

Open Access

IJCER ONLINE

ISSN Online: 2250-3005

Impact Factor: 1.145



IJCER - International Journal of Computational Engineering Research

Volume 05 - Issue 06 , (June 2015)



Editorial Board

Editor-In-Chief

Prof. Chetan Sharma

Specialization: Electronics Engineering, India
Qualification: Ph.d, Nanotechnology, IIT Delhi, India

Editorial Committees

DR.Qais Faryadi

Qualification: PhD Computer Science
Affiliation: USIM(Islamic Science University of Malaysia)

Dr. Lingyan Cao

Qualification: Ph.D. Applied Mathematics in Finance
Affiliation: University of Maryland College Park,MD, US

Dr. A.V.L.N.S.H. HARIHARAN

Qualification: Phd Chemistry
Affiliation: GITAM UNIVERSITY, VISAKHAPATNAM, India

DR. MD. MUSTAFIZUR RAHMAN

Qualification: Phd Mechanical and Materials Engineering
Affiliation: University Kebangsaan Malaysia (UKM)

Dr. S. Morteza Bayareh

Qualificatio: Phd Mechanical Engineering, IUT
Affiliation: Islamic Azad University, Lamerd Branch
Daneshjoo Square, Lamerd, Fars, Iran

Dr. Zahéra Mekkioui

Qualification: Phd Electronics
Affiliation: University of Tlemcen, Algeria

Dr. Yilun Shang

Qualification: Postdoctoral Fellow Computer Science
Affiliation: University of Texas at San Antonio, TX 78249

Lugen M.Zake Sheet

Qualification: Phd, Department of Mathematics
Affiliation: University of Mosul, Iraq

Mohamed Abdellatif

Qualification: PhD Intelligence Technology
Affiliation: Graduate School of Natural Science and Technology

Meisam Mahdavi

Qualification: Phd Electrical and Computer Engineering

Affiliation: University of Tehran, North Kargar st. (across the ninth lane), Tehran, Iran

Dr. Ahmed Nabih Zaki Rashed

Qualification: Ph. D Electronic Engineering

Affiliation: Menoufia University, Egypt

Dr. José M. Merigó Lindahl

Qualification: Phd Business Administration

Affiliation: Department of Business Administration, University of Barcelona, Spain

Dr. Mohamed Shokry Nayle

Qualification: Phd, Engineering

Affiliation: faculty of engineering Tanta University Egypt

Contents:

S.No.	Title Name	Page No.
Version I		
1.	A New Approach of Right State Machine in Discrete Alphabets System. Sarat K. Parhi	01-03
2.	PSO-based Training, Pruning, and Ensembling of Extreme Learning Machine RBF Networks Praveen Malali Miltiadis Kotinis	04-12
3.	Offline and Online Bank Data Synchronization System Anil Jaiswal Rahul Sonawane Mrs. Sangeeta Oswal Mrs. Geocy Shejy	13-16
4.	Big Data and Information Security Gang Zeng	17-21
5.	Emerging Trend of Security Testing to Make Application Robust Mr. Shiv kumar Goel Prasad Kuvalekar	22-27
6.	Design of Full Order Optimal Controller for Interconnected Deregulated Power System for AGC Mrs. Upma Gupta Mrs. S.N.Chaphekar	28-40
7.	Synthesis and characterization of resin copolymer derived from cardanol-furfural/ formaldehyde –p-hydroxy benzoic acid. A. Panda J.Ch. Pal Dr.P.K. Mishra Dr. S.K. Swain Dr.B.Pr. Sahu	41-49
8.	A Hybrid Virtual Reality Simulation System for Wave Energy Conversion Trongnghia Huynh Gene Hou Jin Wang May Hou Miltiadis Kotinis	50-60
9.	Using Computational Fluid Dynamics as a tool for improved prediction of pressure characteristics of a pilot chamber of PRSOV Binod Kumar Saha Dipankar Sanyal	61-70
10.	Hydraulic Transient: Lift Irrigation Scheme Mohite Sudhir Ganpat Morankar D.V.	71-78

A New Approach of Right State Machine in Discrete Alphabets System.

Sarat K. Parhi

Venus Group of Educational and Research Institute, Bahanaga, Balasore-756042, Odisha

ABSTRACT

In this paper, Right State Machine is a new approach of finite automata. The properties of recursive sets related to the Right State Machine is discussed in this paper. The easily understandable theorems are stated in this paper. The idea is applied to specified computer automata and formal language over a new machine.

KEY TERMS: Finite automata, Right State Machine (RSM), Formal language, Discrete alphabets system (DAS).

I. INTRODUCTION

The discrete alphabets system (DAS) is also known as message. The aim is to supervise it in specific order restricting its meaning and its behaviour without violating the specification. The properties of recursive set has a vital rule of this paper.

In communication system, the language reject due to noise information. The language is acceptable for correct information. The error arises during its channel and transmission time, and also the error arises in the defective machine. The processing of information have important in twenty first century of the world information system. We introduced discrete alphabet system (DAS) is one of the information processing model of the communication system.

II. NOTATION & TERMINOLOGY

The discrete alphabets system (DAS) called message is modeled as state machine denoted by a five tuple $M = (Q, \Sigma, \delta, q_0, R)$. Where Q denotes set of states, Σ denotes the finite set of alphabets. $\delta : Q \times \Sigma \rightarrow Q$ denotes the partial deterministic state transition function, $q_0 \in Q$ denotes the initial state, R denotes the right states. A triple $(q_1, \sigma, q_2) \in Q \times \Sigma \times Q$

such that $\delta(q_1, \sigma) = (q_2, r_2)$ is the transition in M . Where $r_1 \in R$ denote for right move. The machine M is denote by $R(M)$ is called language accepted by the right step machine.

$R(M) = \{ \omega \in \Sigma^* / \delta(q_0, \omega) \text{ is the right moves and same state to itself} \}$.

Where Σ^* denotes sequence of starting over Σ . ω is a path from vertex i to j in M is a path from i to j such that the concatenation of the labels along this path from the word ω . R be the right state. Where Σ^* denotes the string of events belong to Σ including the zero length of the sequence ϵ the transition function $\delta : Q \times \Sigma^* \rightarrow Q$

In general, the alphabets can be partitioned into the set of reject symbols Σ_r , and the set of acceptance symbol $\Sigma_a = \Sigma - \Sigma_r$. A set S is a map $S: R(M) \rightarrow Q^{\Sigma - \Sigma_r}$ that determines the set of alphabets $S(s) \subseteq (\Sigma - \Sigma_r)$ to occurrence of trace $S \in R(M)$.

For example if we consider a communication node as DAS with the alphabet set of acceptable and rejectable language. The alphabet is an example of reject able alphabet since the arrival of a language is not under the control of the microwave tower or satellite communication. The alphabet can be partitioned into the set of acceptable and reject able alphabet. In this paper we consider the alphabet to acceptable by the machine. $M^a = (Q^a, \Sigma^a, \delta^a, q_0^a, R^a)$ and its acceptable language by $R(M^a) \in R(M^a)$

$s \in R(M^a), \sigma \in S(s), s_\sigma \in R(M) \Rightarrow s_\sigma \in R(M^a)$

2.1. ILLUSTRATIVE EXAMPLES:-

Consider the right state machine $M = (Q, \Sigma, \delta, q_0, R)$ where $Q = \{q_0, q_1, q_2, q_3, q_4\}$

$\Sigma = \{a, b\}$ and $R \subseteq Q, \delta : Q \times \Sigma \rightarrow (Q, R), R \subseteq Q$

states	inputs	
Q	a	b
q ₀	q ₁	-
q ₁	q ₁	q ₂
q ₂	q ₃	-
q ₃	q ₃	q ₄

(Figure- 2.1)

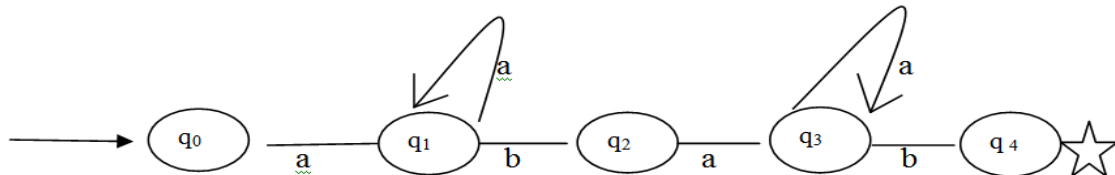
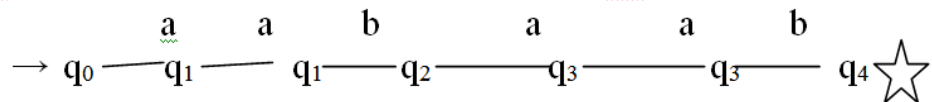


(Figure-2.02(Transition diagram))

Suppose aabaab even number of a and even number of b's in Σ^*



The arrow \rightarrow denotes the initial state and \star denotes the final state.

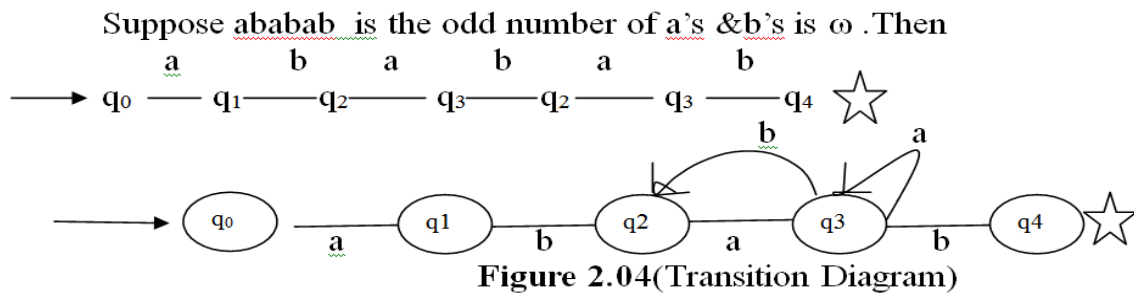
Here, q₄ is the right end state.

Example.2.2

Consider the right state machine $M=(Q,\Sigma,\delta,q_0,R)$ Where $Q=\{q_0,q_1,q_2,q_3,q_4\}$, $\Sigma =\{a,b\}$ and $R \subseteq Q$

States	Inputs	
Q	a	b
q ₀	q ₁	-
q ₁	-	q ₂
q ₂	q ₃	q ₂
q ₃	q ₃	{q ₂ ,q ₄ }

Figure-3.03



Here, it is not a Right state machine because at q_3 state it return back to q_2 . So, ababab is not in $R(M^a)$.

III. PROPERTIES OF RECURSIVE SETS:-223

If a set S of words over Σ to be recursive are satisfied the following.

- i) The Touring machine (T^M) accepts every words in S and reject every words in Σ^*-S .
- (ii) The Right State Machine (RSM) which accepts every words in S and reject every words in Σ^*-S .
- (iii) The Finite State Machine (FSM) with two push down stores which accepts every words in S and reject every words in Σ^*-S .

IV. PROPOSED THEOREM:-

Theorem-4.1:

A set is regular over Σ iff it is accepted by some Right state machine M over Σ .

Proof: Let us prove this theorem, we apply to the method of induction on the word.

Basis: The empty word ϵ is accepted by M iff the initial vertex is final.

Inductive steps: For a word of length n is $\omega \in \Sigma^*$, a ω path from vertex i to vertex j in M is a path from i to j such that the concatenation of the labels along this path from the word. A word $\omega \in \Sigma^*$ is accepted by the Right state machine M if the ω path from the initial vertex leads to the final one.

This is the complete proof of this theorem.

THEOREM-4.2.:-

If a set over Σ is recursive then its compliment Σ^-S is also recursive.*

Proof: In order to prove this theorem, we follow the following steps.

Basis: If S is a recursive null or empty word set over Σ , then there is a Right State Machine M which always move towards right and same state to itself and accepts in S , and also rejects all words in Σ^*-S .

Recursive steps: Construct a Right State Machine M' from M by inter changing the ACCEPT and REJECT words. Clearly M accepts all words in Σ^*-S and reject all words in S .

V. CONCLUSION:-

This paper investigated as behaviour of communication on discrete alphabet system. It would be interesting that the words are not acceptable and examine the conditions. The Right State Machine is the viral rule for preparation of this paper. The error arises during the transmission are the issues of the paper.

REFERENCES:-

- [1]. S.R. Mohanty and R. Kumar, on the synthesis of an optimal controller for a class of Discrete Event Process, proceedings of first international conference Trends in Information Technology, CIT-98, P-82-86, 1998.
- [2]. John E.Hofcroft and J.D.Ullman, Introduction to Automata theory, languages and computation, Narosa Publishing House, 1993.

PSO-based Training, Pruning, and Ensembling of Extreme Learning Machine RBF Networks

Praveen Malali¹ and Miltiadis Kotinis²

¹Department of Mechanical and Aerospace Engineering
Old Dominion University, Norfolk, VA 23509

ABSTRACT:

The research presented in this article focuses on the development of a methodology for ensembling radial basis function (RBF) networks that have been trained using particle swarm optimization (PSO) and the extreme learning machine (ELM). PSO is used to find optimal values for the basis width and the coordinates of the kernel centers, while ELM provides the values of the network connection weights. The ensemble consists of RBF networks that correspond to the personal best positions found by the swarm particles during the search process. The swarm intelligence search mechanism is supplemented with a mutation operator, which incorporates substitution of the worst performing particles by the best performing particle, after the latter has been mutated. Pruning of the input layer of the RBF networks is also implemented in the algorithm. The generalization performance of the PSO-ELM algorithm is evaluated by applying it to a number of widely-utilized regression and time series prediction benchmark problems. The results reveal that the proposed methodology is very effective even when small RBF networks are utilized.

KEYWORDS: Radial basis function, network extreme learning machine, particle swarm optimization, ensembling pruning.

I. INTRODUCTION

The extreme learning machine (ELM) is a fast machine learning algorithm utilized for the training of single-hidden-layer feed forward neural networks (SLFNs) [1–3]. It was developed as an alternative to gradient-based learning algorithms, e.g., back-propagation, in order to accelerate the training of the network, provide good generalization performance by obtaining the smallest norm of the connection weights, and also obviate the need for time-consuming algorithmic parameter tuning [1]. Various ELM-based algorithms have been proposed over the last few years [4,5] in an attempt to reduce the typically high number of hidden nodes required by the ELM due to the random determination of the connection weights between input and hidden layer. Furthermore, the ELM has been combined with evolutionary algorithms [6] in order to evolve the network parameters in tandem with the connection weights.

Radial basis function (RBF) networks [7, 8] are a particular type of SLFNs, which has been used extensively for function approximation and time series prediction. RBF networks are universal approximators [8], i.e., given a sufficiently large number of hidden layer nodes they can be trained to approximate any real multivariate continuous function on a finite data set. An RBF network utilizes a radial basis kernel in each hidden node in order to obtain accurate local, relative to the kernel center, approximations of the unknown function. The Gaussian and the inverse multiquadric kernels, which are radially symmetric and bounded, are frequently used as basis functions in RBF networks. The output of the network is obtained through a linear combination of the hidden nodes' output.

A comparison between the performance of an ELM-based RBF network and a support vector regression (SVR) algorithm in a very small number of regression problems is presented in [9]. The two methods have comparable performance in terms of approximation accuracy, but the ELM-based RBF network requires a significantly shorter time for training. Given that the kernel centers and basis widths are selected randomly in the aforementioned ELM-based methodology, the algorithmic performance would most likely improve via a less random selection scheme; however, such a scheme should not mitigate the major advantage of ELMs, i.e., the fast training of the network. Furthermore, as shown in [10], the performance of an RBF network in a number of time series prediction problems strongly depends on the choice of kernel function, number of hidden nodes, and basis width values.

The training of artificial neural networks (ANNs), including RBF networks, using evolutionary algorithms has been an active area of research during the last fifteen years. Evolutionary algorithms have been employed in order to evolve the network connection weights [11,12], the location of the kernel centers of an RBF network [13], and also to evolve basis width values, location of kernel centers, and connection weights simultaneously [14]. The determination of the values of the network connection weights in tandem with the network architecture has also been investigated in [15-17]. Finally, evolutionary multi-objective optimization algorithms have been employed in order to generate ensembles of neural networks and/or learning machines [18-21].

The main advantage of using stochastic evolutionary algorithms for the network training over traditional, gradient-based algorithms is the inherent capability of the former to minimize the risk of getting trapped in locally optimal values during the search/training process. Furthermore, most evolutionary algorithms are population-based, i.e., perform multiple parallel searches during a single run; this enables them to explore different regions of the decision variable space simultaneously and through the utilization of appropriate mechanisms to transmit search-related information across the population. In this work, PSO and the ELM are combined in order to develop an algorithm that generates ensembles of RBF networks. The generalization error of an ensemble of networks/learners is equal to the weighted average of the generalization error of the individual networks minus the ensemble ambiguity [22]; the latter quantifies the diversity within the ensemble. Therefore, the objective when generating such an ensemble is that it comprises a diverse set of accurate learners. The global best (gbest) PSO search mechanism [23] attempts to direct each population member towards the global optimal solution vector that has been found up to the current iteration, but also towards the personal best position (solution vector) that has been found by the corresponding population member thus far. In this article, it is shown that these two features of the (gbest) search and network training mechanism provide the desirable diverse ensemble of accurate learners. Diversity is preserved via the attraction of each population member towards its current personal best solution and improved prediction accuracy is achieved via its attraction towards the solution with the current minimum validation error. When the stopping criterion of the training process has been met, the current set of personal best solution vectors comprises the ensemble of RBF networks that is utilized to compute the network output.

The rest of the article is organized as follows: The proposed methodology for training, pruning, and ensembling of RBF networks is presented in Sect. 2. The results of its application to regression and time series prediction benchmark problems and comparisons with other SLFN learners are presented in Sect. 3. Conclusions are provided in Sect. 4.

II. TRAINING, PRUNING, AND ENSEMBLING OF RBF NETWORKS USING PSO AND THE ELM

2.1 ELM-based RBF network

An RBF network is an SLFN with a radial basis function assigned to each hidden node. Therefore, the function to be approximated is represented as an expansion in basis functions, which are modeled using kernel functions. Even though, there are no connection weights between input and hidden layer, the coordinates of the kernel centers need to be determined and, thus, are considered parameters of the network. In this work, the inverse multiquadric kernel is utilized in the following form,

$$\phi(\mathbf{x}) = (\|\mathbf{x} - \bar{\mathbf{x}}\|^2 + \sigma^2)^{-1/2} \tag{1}$$

where $\bar{\mathbf{x}}$ is the kernel center coordinate vector, \mathbf{x} is the input vector, and σ is the basis width, or smoothing parameter, which also needs to be determined for each kernel. The RBF network output is computed as the weighted average of the output of the hidden nodes, including the contribution of a bias node. Assuming a network with N hidden layer nodes and a single output node, the value of the approximated function at \mathbf{x} is computed as follows,

$$f(\mathbf{x}) = \sum_{n=1}^N w_n \phi_n(\mathbf{x}) + w_0 \tag{2}$$

where w_n is the weight of the n^{th} radial basis function in the corresponding hidden node and w_0 is the bias node weight. These $N + 1$ weights are obtained through a supervised learning approach, i.e., the network is trained by adjusting its parameters so that the overall output error is minimized when it is evaluated on a training dataset.

The training objective is typically formulated as a minimization of the sum-of-squares problem.

$$\min_{(\sigma_n, \bar{\mathbf{x}}_n, w_n)_1^N} \sum_{p=1}^P (f(\mathbf{x}_p) - y(\mathbf{x}_p))^2 \tag{3}$$

where P is the number of instances in the training dataset. The optimization problem defined in eq. (3) is nonconvex with multiple local minima [25]. Gradient descent can be utilized to obtain a solution for the network weights, the kernel centers, and the basis widths [8]. Given the local-approximator nature of bounded radial basis functions, a clustering algorithm, e.g., K -means, can also be employed at the initial phase of the training process to determine the positions of the kernel centers [26]. The ELM algorithm adapted for RBF networks [10] provides a much faster approach: The kernel centers and basis widths are initialized with random values from within a specific range and the problem of determining the weights is then formulated as follows,

$$\sum_{n=1}^N w_n \phi_n(\mathbf{x}_p) + w_0 = y(\mathbf{x}_p), \quad p \in \{1, \dots, P\} \quad (4)$$

This corresponds to a linear system of P equations, which can be written in a compact matrix form as follows.

$$\mathbf{H}\mathbf{w} = \mathbf{Y} \quad (5)$$

The training of the network can then be accomplished by finding a least-squares solution $\hat{\mathbf{w}}$ of eq. (5): $\min_{\mathbf{w}} \|\mathbf{H}\mathbf{w} - \mathbf{Y}\|$. In most practical applications, the number of hidden nodes is much smaller than the size of the training dataset. In this case, eq. (5) corresponds to an over determined system of equations and the unique smallest-norm least squares solution is as follows.

$$\hat{\mathbf{w}} = \mathbf{H}^\dagger \mathbf{Y} \quad (6)$$

where \mathbf{H}^\dagger is the Moore-Penrose generalized inverse matrix [27]. This can be computed using a number of methods; in this work this is done using the singular value decomposition (SVD) approach. As is pointed out in [10, 28], in general, the smaller the network weights, the better the generalization performance; using the \mathbf{H}^\dagger matrix, the smallest hidden-to-output layer weights are obtained.

2.2 Particle swarm optimization

The utilization of the ELM for the training of SLFNs results in a significant reduction in the training time compared to gradient-based tuning algorithms. However, as is reported in [6], when the ELM is employed for the training of ANNs, the random selection of the values of the input weights tends to favor networks with a larger number of hidden nodes compared to gradient-based network tuning. In order to address this issue, an evolutionary algorithm can be utilized to evolve the network parameters, as is done in [6] where a differential evolution algorithm is combined with the ELM to train ANNs. In addition to a shorter training time, a more compact network architecture could also result in better generalization performance. These observations are expected to be applicable to other types of SLFNs like RBF networks. In this work, PSO is utilized to evolve both the position of each kernel and the corresponding basis width.

The *gbest* PSO model [29] uses a population of swarm particles (solution vectors) that search for the optimal solution simultaneously and in a cooperative manner. The position vector of each particle $\mathbf{x} \in \mathbb{R}^J$ is updated at each iteration $t + 1$ using the following scheme for every $j \in \{1, \dots, J\}$:

$$x_j(t + 1) = x_j(t) + v_j(t + 1) \quad (7)$$

$$v_j(t + 1) = \chi(v_j(t) + \phi_1 \cdot U_j(0,1) \cdot (\hat{y}_j(t) - x_j(t)) + \phi_2 \cdot U_j(0,1) \cdot (y_j(t) - x_j(t))) \quad (8)$$

where $x_j(t), v_j(t), x_j(t + 1)$, and $v_j(t + 1)$ are the particle's j^{th} position coordinate and velocity over a single time increment at iteration t and $t + 1$, respectively. ϕ_1 and ϕ_2 are coefficients that adjust the attraction of the particle towards the global best solution that has been found by the swarm thus far, $\hat{\mathbf{y}}(t)$, and towards the best solution that has been found by the particle up to iteration t , $\mathbf{y}(t)$, respectively. $U_j(0,1)$ is a uniformly distributed random number in $(0, 1)$ sampled anew for each j and particle.

In order to prevent the velocity of each particle from increasing uncontrollably when using eq. (7), various methods have been proposed over the years; here the concept of the constriction coefficient [30] is adopted. The constriction coefficient, χ , is computed using the following scheme as shown.

$$\chi = \frac{2k}{|2 - \phi - \sqrt{\phi^2 - 4\phi}|} \quad (9)$$

where $\phi = \phi_1 + \phi_2, \phi > 4, k \in [0, 1]$.

In this work, k is set equal to one in order to promote a high degree of exploration of the search space, ϕ is set equal to 4.1, as is suggested in [31], and ϕ_1 is set equal to ϕ_2 . The condition $\phi > 4$ is a necessary condition for the convergence of the particle's trajectory to a position inside the search space. This is proven in [30], where the equations of motion are modeled as a discrete-time dynamic system and a stability analysis is performed in order to derive conditions for its convergence to an equilibrium point. Using the *gbest* model, the particle attractor (equilibrium point) corresponds to a weighted average between its personal best and global best positions. In the current application, when the network training has been completed, it is anticipated that the set of personal best positions contains solution vectors close to the global best solution, depending on the size of the attraction basin, which are also distinct enough to satisfy the diversity requirement for the ensemble members.

The positions of the particles are initialized randomly within the range of each coordinate (input variable): $x_j \in [x_j^{(L)}, x_j^{(U)}], j \in \{1, \dots, J\}$. The velocities are initialized with zero values. During the iterative search process, when a particle moves to a position outside of the allowable range in coordinate j , its position coordinate j is set equal to the closest boundary value and the corresponding velocity component is set equal to zero. At the end of each iteration, the performance of the swarm particles is assessed by computing the root mean squared error (RMSE) on a validation set, which contains data that are not included in the training dataset. This is done in order to update, if applicable, the global best and personal best solution vectors. The RBF network parameters that are optimized are the kernel center coordinates and basis widths.

In this research, the PSO algorithm is modified as follows: The particle with the worst (highest) RMSE value at the end of each iteration is replaced by a mutated (perturbed) copy of the global best solution vector. The mutation is performed using the following scheme $j \in \{1, \dots, J\}$,

$$x_j = \begin{cases} \hat{y}_j + msf \cdot (x_j^{(U)} - x_j^{(L)}), & \text{if } U_j(0,1) < mrt \\ \hat{y}_j, & \text{otherwise} \end{cases} \quad (10)$$

where msf is the mutation scaling factor and mrt is the mutation rate. In this way, the optimizer is able to perform a local search in the vicinity of the global best solution found thus far through small perturbations of the corresponding solution vector. During the initialization of the PSO parameters' values for each swarm particle, the input layer of each corresponding RBF network, i , is pruned by randomly selecting the input variables that will be included in the network as shown below,

$$x_{ij} = \begin{cases} deactivated, & \text{if } U_{ij}(0,1) < prr \\ activated, & \text{otherwise} \end{cases} \quad (11)$$

where prr is the pruning rate and $j \in \{1, \dots, J\}, i \in \{1, \dots, I\}$.

The main reason for pruning the input layer is to remove variables that do not contribute towards a better understanding of the underlying process that produced the dataset and, thus, their inclusion does not cause a substantial increase in the accuracy of the approximation/prediction model. In the proposed approach, the importance of the input variables is not estimated explicitly; the determination of the optimal input layer architecture is done gradually through the aforementioned particle replacement operation as, at each iteration, the network with the worst performance is discarded and replaced by a network with the optimal input layer architecture that has been found thus far.

2.3 Implementation of the proposed algorithm for training and ensembling of RBF networks

The PSO algorithm described in the previous section is utilized for the training of the ELM-based RBF networks. The training of the ELM-based RBF networks is stopped if either the global optimal solution has not changed after I_{ch} iterations or the algorithm has reached the maximum allowable number of iterations I_{max} . Two distinct sets of data points are used during the training process; the first corresponds to the training data set, which is used to compute the network weights via Singular Value Decomposition (SVD). The particles (solution vectors) are then evaluated on a validation set in order to find global and personal best positions. In this way, the risk of overtraining the network is reduced. The global best position corresponds to the network with the smallest prediction error on the validation set. The prediction error is quantified by computing the root mean squared error (RMSE). The training and validation data sets, both input and output values, are normalized in the range [-1.0, 1.0]. The ensembling process commences immediately after the training of the RBF networks has been finalized. The output of the ensemble is obtained by averaging the output of its members, i.e., the personal best solutions of the swarm particles. Prior to the evaluation of the generalization performance of the ensemble on a testing dataset, the existence of outliers among the ensemble members is investigated by applying Chauvenet's criterion [32]. This criterion specifies that all points that fall within a band around the mean that corresponds to a probability of $[1 - 1/(2E)]$ should be retained.

E is the original size of the ensemble and, thus, is equal to the swarm population size. The criterion is applied only once for each point of the testing dataset. Using Gaussian probabilities, the ratio of maximum acceptable deviation to sample standard deviation is computed and utilized for the detection of outliers [33]. The algorithm has been developed in FORTRAN 95. The training and testing processes of the PSO-trained ELM-based RBF network ensemble are outlined in Fig. 1.

```

Specify the RBF network architecture
Initialize the swarm population particles (each particle corresponds to an RBF network)
iter = 0
do
    Compute the connection weights of each RBF network using the training data set and SVD
    Evaluate each RBF network on the validation data set by computing the RMSE
    Find the global best RBF network up to the current iteration
    Update, if applicable, the personal best position of each particle
    Move each particle to a new position inside the search space using the gbest PSO algorithm
    iter = iter + 1
until stopping criterion is satisfied
Form RBF network ensemble by combining the personal best positions of the swarm particles
Apply Chauvenet's criterion while computing the ensemble prediction on the testing data set
    
```

Figure 1. Pseudo-code of the PSO-trained ELM-based RBF network ensemble.

2.4 Experimental investigation

The generalization performance of the RBF networks trained using the proposed methodology is investigated and the results are presented in this section. In all the experiments, the swarm population size I is set equal to 20 and I_{ch} and I_{max} are set equal to 8 and 50, respectively. In the first part of this investigation, the number of hidden nodes is set equal to 10 in order to observe the algorithmic effectiveness and efficiency using a small-sized network. The coordinates of the kernel centers are allowed to vary within the range [-1.0, 1.0], while the basis width values within the range [1.0, 60.0]. The mutation parameters, msf and mrt , are set equal to 0.2 and 0.5, respectively, and the pruning rate prr is set equal to 0.2. The training and validation datasets are normalized in the range [-1.0, 1.0].

Ten widely-utilized benchmark problems are considered: Eight regression and two time series prediction problems. The datasets of the majority of these problems have been obtained from the UCI machine learning repository [34]. The problem features and additional references are provided in Table 1.

Table 1. Features of regression and time series prediction benchmark problems.

ID	Problem description	Number of data points	Number of inputs	Input types
BNK	Bank queues simulation	8192	8	integer, real
FF	Forest fires [36]	517	4	real
BH	Housing values in Boston	506	13	categorical, integer, real
CCS	Concrete compressive strength [37]	1030	8	real
SRV	Servomechanism	167	4	categorical, integer
CS	Concrete slump test [38]	103	7	real
CH	Computer hardware performance	209	7	integer
WBP	Breast Cancer Wisconsin (Prognostic)	198	32	real
BJ	Box-Jenkins time series [39]	290	10	real
MG	Mackey-Glass time series [40]	4898	11	real

The dataset of each problem is first randomized and then split into three groups: 40% of the data are used for training, 10% for validation, and 50% for testing. Fifty independent runs are performed for each problem. The RMSE and the mean absolute error (MAE) of the predictions on the testing set are computed using the network output, after it has been transformed back to its original scale, and recorded for the ensemble and for the RBF network with the lowest RMSE value on the validation set. The same 10 problems are used in all phases of this investigation. The computational cost of obtaining the ensemble predictions is negligible compared to the corresponding cost of the training process; on average, the time used to compute the ensemble predictions is equal to 0.7% of the time required for the training process on a machine with 16 GB of RAM and a quad-core 2.80 GHz processor running on a 64-bit Linux operating system.

III. EFFECTIVENESS OF THE PROPOSED ENSEMBLING METHODOLOGY

In the first part, the effectiveness of the proposed methodology is tested, and in particular the utilization of the mutation operator combined with the pruning of the input layer. The RMSE and the mean absolute error (MAE) of the predictions are computed on the testing dataset using the network output, after the latter has been transformed back to its original scale, and recorded for the ensemble (ENS) and for the global best RBF network (GB), i.e., the network with the lowest RMSE value on the validation set at the end of each run. The corresponding versions without mutation and pruning are denoted by ENS_NMP and GB_NMP, respectively. The lower the RMSE and the MAE values, the better the algorithmic performance. The results are shown in Table 2.

In all cases, a single hidden layer with 10 nodes is utilized and the maximum number of training iterations per run is set equal to 1000. A pairwise comparison between ENS and ENS_NMP to determine the statistical significance of the results is also performed using the two-tailed *p*-values, which have been computed using the *t*-test for unequal variances. In the problems where an algorithm has statistically better performance than the other at the 0.05 significance level, the mean value of its RMSE is highlighted in bold font.

The results reported in Table 2 demonstrate the effectiveness of mutation and input-layer pruning on the algorithmic performance: ENS outperforms ENS_NMP in all 10 problems and in both metrics; the difference in the mean values is statistically significant at the 0.05 level in seven problems using either metric. Furthermore, the generalization performance of the ensemble (ENS) is clearly better than the performance of the global best network (GB) in both metrics when mutation and input-layer pruning are incorporated into the algorithm; the same conclusion cannot be drawn from a generalization performance comparison between GB_NMP and ENS_NMP, which further corroborates the claim that mutation and pruning enhance the PSO-training and ensembling effectiveness.

Table 2. RMSE and MAE results for ENS, GB, ENS_NMP and GB_NMP.

ID	RMSE & MAE	ENS	GB	ENS_NMP	GB_NMP
BNK	RMSE	7.209 ·10 ⁻²	7.254·10 ⁻²	8.721·10 ⁻²	8.725·10 ⁻²
	MAE	5.457 ·10 ⁻²	5.497·10 ⁻²	6.797·10 ⁻²	6.793·10 ⁻²
FF	RMSE	1.338	1.340	13.341	1.340
	MAE	1.067	1.069	1.096	1.092
BH	RMSE	4.436	4.601	4.986	4.893
	MAE	3.411	3.545	3.897	3.820
CCS	RMSE	1.281 ·10 ¹	1.368·10 ¹	1.531·10 ¹	1.536·10 ¹
	MAE	1.006 ·10 ¹	1.055·10 ¹	1.258·10 ¹	1.247·10 ¹
SRV	RMSE	9.675 ·10 ⁻¹	1.038	9.973·10 ⁻¹	1.002
	MAE	5.442 ·10 ⁻¹	5.941·10 ⁻¹	6.200·10 ⁻¹	6.156·10 ⁻¹
CS	RMSE	8.133	9.139	8.295	9.764
	MAE	6.612	7.253	6.728	7.781
CH	RMSE	1.265·10 ¹	1.474·10 ¹	1.311·10 ¹	1.617·10 ¹
	MAE	5.581	6.338	5.801	6.967
WBP	RMSE	3.546 ·10 ¹	3.832·10 ¹	4.160·10 ¹	4.237·10 ¹
	MAE	2.953 ·10 ¹	3.198·10 ¹	3.497·10 ¹	3.546·10 ¹
BJ	RMSE	4.324 ·10 ⁻¹	4.437·10 ⁻¹	4.414·10 ⁻¹	4.559·10 ⁻¹
	MAE	3.095·10 ⁻¹	3.171·10 ⁻¹	3.128·10 ⁻¹	3.225·10 ⁻¹
MG	RMSE	1.187 ·10 ⁻²	1.276·10 ⁻²	2.165·10 ⁻²	2.144·10 ⁻²
	MAE	1.027 ·10 ⁻²	1.034·10 ⁻²	1.783·10 ⁻²	1.759·10 ⁻²

The performance of the ensemble (ENS) and of the global best (GB) of the PSO-ELM-trained RBF networks is compared with the performance of two other SLFN learners: An artificial neural network (ANN) that uses the back propagation algorithm for training and an RBF network that uses *K*-means clustering (RBF_K) to obtain the kernel parameters and linear regression to compute the network weights. Both algorithms are available in the open source data mining software WEKA [42]. The ANN uses a momentum term with value set equal to 0.2 and a learning rate with value set equal to 0.3. Both SLFN learners use a single hidden layer with 10 nodes; the number of training iterations is set equal to 1000.

Table 3. Mean and standard deviation values of RMSE for RBF_K, ANN, GB and ENS.

ID	Mean & Deviation	RBF_K	ANN	GB	ENS
BNK	Mean	1.420·10 ^{-1*}	8.130·10 ^{-2*}	7.254·10 ⁻²	7.209·10⁻²
	Deviation	1.484·10 ⁻⁴	1.276·10 ⁻²	2.640·10 ⁻⁴	3.545·10 ⁻⁴
FF	Mean	1.359*	1.461*	1.340	1.338
	Deviation	1.391·10 ⁻²	1.326·10 ⁻¹	2.500·10 ⁻²	2.562·10 ⁻²
BH	Mean	7.505*	5.455*	4.601	4.436
	Deviation	2.919·10 ⁻¹	1.089	4.694·10 ⁻¹	2.954·10 ⁻¹
CCS	Mean	1.844·10 ^{1*}	1.727·10 ^{1*}	1.368·10 ¹	1.281·10¹
	Deviation	1.870	3.071	2.052	1.969
SRV	Mean	1.524*	1.014	1.038	9.675·10⁻¹
	Deviation	7.097·10 ⁻²	2.278·10 ⁻¹	6.677·10 ⁻²	4.355·10 ⁻²
CS	Mean	1.169·10 ^{1*}	8.715*	9.139	8.133
	Deviation	9.547	1.381	1.085	9.001·10 ⁻¹
CH	Mean	1.261·10 ^{2*}	1.380·10 ¹	1.474·10 ¹	1.265·10¹
	Deviation	3.996·10 ¹	1.271·10 ¹	6.197	3.342
WBP	Mean	3.835·10 ^{1*}	4.172·10 ^{1*}	3.832·10 ¹	3.546·10¹
	Deviation	1.222	9.467	2.114	5.716·10 ⁻¹
BJ	Mean	1.364*	5.893·10 ^{-1*}	4.437·10 ⁻¹	4.324·10⁻¹
	Deviation	1.102·10 ⁻¹	1.913·10 ⁻¹	2.878·10 ⁻²	2.236·10 ⁻²
MG	Mean	8.180·10 ^{-2*}	1.068·10 ⁻²	1.276·10 ⁻²	1.187·10 ⁻²
	Deviation	5.506·10 ⁻³	3.257·10 ⁻³	3.624·10 ⁻³	2.809·10 ⁻³

The computed mean (Mean) and standard deviation (Deviation) values of RMSE are listed in Table 3. Pairwise comparisons between ENS, RBF_K, and ANN are performed in order to determine the statistical significance of the results. If the performance of ENS in a problem is statistically better than the performance of another algorithm, then there is an asterisk (*) next to the other algorithm's corresponding mean RMSE value. If the difference in performance between ENS and GB is statistically significant at the 0.05 level, the mean value of the more accurate algorithm is highlighted in bold font.

The RMSE results displayed in Table 3 reveal that the PSO-ELM-trained RBF network ensemble has better generalization performance than the RBF_K learner in ten problems, a result that is statistically significant in all ten problems, and in nine problems compared to the ANN, a result that is statistically significant in seven problems. Furthermore, the variance in the ENS results is very small compared to the other two SLFN learners. In none among the ten problems the performance of either ANN or RBF_K is statistically better than the performance of ENS. A comparison between the results of GB and ENS shows that the latter performs better in all ten problems, a result that is statistically significant in eight problems. Overall, these results demonstrate that the PSO-trained ELM-based RBF network ensembling methodology has very good generalization performance even when applied to a small-sized network. The proposed PSO-ELM-based training methodology without the ensembling is also successful as GB has a lower mean RMSE value than the RBF_K and the ANN in ten and six problems, respectively.

3.1 RBF Networks with Optimal Number of Hidden Layer Nodes

In the final part, the number of hidden layer nodes is varied in an attempt to optimize the network size. Starting with two hidden nodes, the number is increased manually in steps of one node to a maximum number of twenty nodes. The network size of the ensemble (ENS_OPT) that produces the lowest mean RMSE value in each problem is (following the sequence used in Table 1): {20, 11, 5, 12, 20, 12, 20, 18, 20, 20}. The corresponding mean RMSE values are shown in Table 4.

The results obtained using the IB5 *k*-nearest neighbor algorithm [43], a Gaussian process (GP) learner, and M5P [44], a tree-based method with pruning, are also listed in Table 4. GP uses the Gaussian kernel function with a basis width that is varied manually from within the following set of discrete values: {0.25, 0.5, 1.0, 1.5, 2.0, 3.0, 5.0, 10.0}. The results that correspond to the basis width value that produces the lowest mean RMSE in each problem are shown in Table 4. The corresponding basis width values are: {1.0, 1.0, 1.5, 1.0, 0.5, 5.0, 1.5, 3.0, 2.0, 10.0}. The data mining software WEKA is utilized to generate the results for IB5, GP, and M5P. The lowest mean RMSE and MAE values in each problem are highlighted in bold font.

The generalization performance of the proposed methodology is significantly improved by using an optimal-sized hidden layer as is observed through a comparison between the results of ENS listed in Tables 2 and the results of ENS_OPT listed in Table 4 (next page). A comparison between the results of the GP and the IB5 learners and the results of ENS_OPT reveals that the latter outperforms both learners in all ten problems using either metric. It also outperforms M5P in nine problems using the RMSE metric and in eight problems using the MAE metric.

Table 4. RMSE and MAE results for GP, IB5, M5P and ENS_OPT.

ID	RMSE & MAE	GP	IB5	M5P	ENS_OPT
BNK	RMSE	$7.251 \cdot 10^{-2}$	$1.155 \cdot 10^{-1}$	$7.090 \cdot 10^{-2}$	$7.085 \cdot 10^{-2}$
	MAE	$5.491 \cdot 10^{-2}$	$8.940 \cdot 10^{-2}$	$5.322 \cdot 10^{-2}$	$5.331 \cdot 10^{-2}$
FF	RMSE	1.345	1.443	1.352	1.336
	MAE	1.060	1.095	1.124	1.058
BH	RMSE	4.715	6.615	3.776	4.139
	MAE	3.180	4.602	2.797	3.152
CCS	RMSE	$1.317 \cdot 10^1$	$1.743 \cdot 10^1$	$1.308 \cdot 10^1$	$1.264 \cdot 10^1$
	MAE	$1.094 \cdot 10^1$	$1.410 \cdot 10^1$	$1.036 \cdot 10^1$	9.972
SRV	RMSE	1.061	1.098	$9.261 \cdot 10^{-1}$	$9.030 \cdot 10^{-1}$
	MAE	$5.514 \cdot 10^{-1}$	$5.644 \cdot 10^{-1}$	$4.611 \cdot 10^{-1}$	$4.350 \cdot 10^{-1}$
CS	RMSE	8.218	8.519	8.194	8.073
	MAE	6.401	6.625	6.409	6.395
CH	RMSE	$4.328 \cdot 10^1$	$5.904 \cdot 10^1$	$3.189 \cdot 10^1$	9.121
	MAE	$1.678 \cdot 10^1$	$1.953 \cdot 10^1$	$1.476 \cdot 10^1$	4.385
WBP	RMSE	$3.664 \cdot 10^1$	$3.965 \cdot 10^1$	$3.549 \cdot 10^1$	$3.404 \cdot 10^1$
	MAE	$3.116 \cdot 10^1$	$3.291 \cdot 10^1$	$2.877 \cdot 10^1$	$2.770 \cdot 10^1$
BJ	RMSE	1.003	1.074	$4.521 \cdot 10^{-1}$	$3.915 \cdot 10^{-1}$
	MAE	$7.001 \cdot 10^{-1}$	$7.899 \cdot 10^{-1}$	$3.213 \cdot 10^{-1}$	$2.867 \cdot 10^{-1}$
MG	RMSE	$1.540 \cdot 10^{-2}$	$1.071 \cdot 10^{-2}$	$3.612 \cdot 10^{-2}$	$7.238 \cdot 10^{-3}$
	MAE	$1.180 \cdot 10^{-2}$	$8.700 \cdot 10^{-3}$	$2.860 \cdot 10^{-2}$	$5.758 \cdot 10^{-3}$

IV. CONCLUSIONS AND FUTURE RESEARCH

The development of a new methodology that combines PSO and ELM to train and generate ensembles of RBF networks is described in this article. PSO, supplemented with the proposed mutation operator and pruning of the input layer, is utilized in order to optimize the kernel parameters; this results in RBF networks with a compact architecture and very good generalization performance. Combining the networks that correspond to the personal best positions of the swarm particles to form an ensemble increases the robustness of the algorithm and further enhances its generalization performance. Optimizing the size of the hidden layer results in further improvement in the ensemble's generalization performance. These conclusions are drawn from comparisons between the ensemble's performance and the performance of other SLFNs on eight regression and two time series prediction benchmark problems.

The optimization of the RBF network's architecture without a substantial increase in the required training time is currently being investigated. Furthermore, the development of a PSO model tailored for ensembling purposes, e.g., having more control over the particles' trajectories, is also being considered.

REFERENCES

- [1] G.B. Huang, Q.Y. Zhu, C.K. Siew. Extreme learning machine: theory and applications. *Neurocomputing*, 70(1-3):489-501, 2006.
- [2] Y. Wang, F. Cao, Y. Yuan. A study on effectiveness of extreme learning machine. *Neurocomputing*, 74(16):2483-2490, 2011.
- [3] M. van Heeswijk, Y. Miche, E. Oja, A. Lendasse. GPU-accelerated and parallelized ELM ensembles for large-scale regression. *Neurocomputing*, 74(16):2430-2437, 2011.
- [4] G.B. Huang, L. Chen. Convex incremental extreme learning machine. *Neurocomputing*, 70(16-18):3056-3062, 2007.
- [5] G. Feng, G.B. Huang, Q. Lin and R. Gay. Error minimized extreme learning machine with growth of hidden nodes and incremental learning. *IEEE Transactions Neural Networks*, 20(8), pp. 1352-1357, 2009.
- [6] Q.Y. Zhu, A.K. Qin, P.N. Suganthan and G.B. Huang. Evolutionary extreme learning machine. *Pattern Recognition*, 38(10), pp. 1759-1763, 2005.
- [7] D.S. Broomhead and D. Lowe. Multivariate functional interpolation and adaptive networks. *Complex Systems*, 2, pp. 321-355, 1988.
- [8] T. Poggio and F. Girosi. Networks for approximation and learning. *Proc. IEEE*, 78(9), pp. 1481-1497, 1990.
- [9] C. Harpham and C.W. Dawson. The effect of different basis functions on a radial basis function network for time series prediction: A comparative study. *Neurocomputing*, 69(16-18), pp. 2161-2170, 2006.
- [10] G.B. Huang and C.K. Siew. Extreme learning machine with randomly assigned RBF kernels. *International Journal of Information Technology*, 11(1), pp. 16-24, 2005.
- [11] R. Mendes, P. Cortez, M. Rocha and J. Neves. Particle swarms for feedforward neural network training. In: *Proceedings of the 2002 International Joint Conference on Neural Networks*, Honolulu, Hawaii, pp. 1895-1899, 2002.
- [12] F. Han, H.F. Yao and Q.H. Ling. An improved evolutionary extreme learning machine based on particle swarm optimization. *Neurocomputing*, 116, pp. 87-93, 2013.
- [13] M.W. Mak and K.W. Cho. Genetic evolution of radial basis function centers for pattern classification. In: *Proceedings of the 1998 IEEE International Joint Conference on Neural Networks*, Anchorage, Alaska, pp. 669-673, 1998.
- [14] H.M. Feng. Self-generation RBFNs using evolutionary PSO learning. *Neurocomputing*, 70(1-3), pp. 241-251, 2006.
- [15] J. Gonzalez, I. Rojas, J. Ortega, H. Pomares, F.J. Fernandez and A.F. Diaz. Multi-objective evolutionary optimization of the size, shape, and position parameters of radial basis function networks for function approximation. *IEEE Transactions Neural Networks*, 14(6), pp. 1478-1495, 2003.

- [16] M. Rocha, P. Cortez and J. Neves. Evolution of neural networks for classification and regression, *Neurocomputing*, 70(16-18), pp. 2809-2816, 2007.
- [17] H. Du and N. Zhang. Time series prediction using evolving radial basis function networks with new encoding scheme, *Neurocomputing*, 71(7-9), pp. 1388-1400, 2008.
- [18] I. Kokshenev and P.A. Braga. A multi-objective approach to RBF network learning, *Neurocomputing*, 71(7-9), pp. 1203-1209, 2008.
- [19] N. Kondo, T. Hatanaka and K. Uosaki. Pattern classification by evolutionary RBF networks ensemble based on multi-objective optimization, In: *Proceedings of the 2006 International Joint Conference on Neural Networks*, Vancouver, British Columbia, pp. 2919-2925, 2006.
- [20] Y. Jin, T. Okabe and B. Sendhoff. Neural network regularization and ensembling using multi-objective evolutionary algorithms, In: *Proceedings of the 2004 IEEE Congress on Evolutionary Computation*, Portland, Oregon, pp. 1-8, 2006.
- [21] A. Chandra and X. Yao. Evolving hybrid ensembles of learning machines for better generalization, *Neurocomputing*, 69(7-9), pp. 686-700, 2006.
- [22] A. Krogh and J. Vedelsby. Neural network ensembles, cross validation, and active learning, *Advances in Neural Information Processing Systems*, 7, pp. 231-238, 1995.
- [23] R.C. Eberhart, P.K. Simpson and R.W. Dobbins. *Computational Intelligence PC Tools*. Boston: Academic Press, 1995.
- [24] R.L. Hardy. Multiquadric equation of topography and other irregular surfaces, *Journal of Geophysical Research*, 76(8), pp. 1905-1915, 1971.
- [25] T. Hastie, R. Tibshirani and J. Friedman. *The elements of statistical learning*. New York: Springer Science plus Business Media, 2nd edition, pp. 212-214, 2009.
- [26] J.E. Moody and C. Darken. Learning with localized receptive fields, In: Touretzky D, Hinton G, Sejnowski T (Eds) *Proceedings of the Connectionist Models Summer School*, San Mateo, California, Morgan Kaufmann, pp. 133-143, 1989.
- [27] C.R. Rao and S.K. Mitra. *Generalized inverse of matrices and its applications*. New York: Wiley publications, 1971.
- [28] P.L. Bartlett. The sample complexity of pattern classification with neural networks: the size of the weights is more important than the size of the network, *IEEE Transactions on Information Theory*, 44(2), pp. 522-536, 1998.
- [29] J. Kennedy and R.C. Eberhart. Particle swarm optimization, In: *Proceedings of the 1995 IEEE International Conference on Neural Networks*, Perth, Australia, pp. 1942-1948, 1995.
- [30] M. Clerc and J. Kennedy, J. The particle swarm explosion, stability, and convergence in a multi-dimensional complex space, *IEEE Transactions on Evolutionary Computing*, 6(1), pp. 58-73, 2002.
- [31] R. Eberhart and Y. Shi. Comparing inertia weights and constriction factors in particle swarm optimization, In: *Proceedings of the 2000 IEEE Congress on Evolutionary Computation*, San Diego, California, pp. 84-88, 2000.
- [32] W. Chauvenet. *A manual of spherical and practical astronomy*. Philadelphia: Lippincott, Vol. 2, 1st edition, 1863.
- [33] H.W. Coleman and W.G. Steele. *Experimentation and uncertainty analysis for engineers*. New York: Wiley publications, 2nd edition, 2002.
- [34] K. Bache and M. Lichman. UCI Machine Learning Repository, University of California, School of Information and Computer Science, Irvine, CA, <http://archive.ics.uci.edu/ml>, 2014.
- [35] P. Cortez, A. Cerdeira, F. Almeida, T. Matos and J. Reis. Modeling wine preferences by data mining from physiochemical properties, *Decision Support Systems*, 47(4), pp. 547-553, 2009.
- [36] P. Cortez and A. Morais. Data mining approach to predict forest fires using meteorological data, In: Neves J, Santos MF, Machado J (Eds) *New trends in artificial intelligence*, Proceedings of the 13th EPIA, Portuguese Conference on Artificial Intelligence, Guimaraes, Portugal, pp. 512-523, 2007.
- [37] I.C. Yeh. Modeling of strength of high performance concrete using artificial neural networks, *Cement Concrete Research*, 28(12), pp. 1797-1808, 1998.
- [38] I.C. Yeh, I.C. Modeling slump flow of concrete using second-order regressions and artificial neural networks, *Cement Concrete Composites*, 29(6), pp. 474-480, 2007.
- [39] G.E.P. Box and G.M. Jenkins. *Time series analysis: forecasting and control*. San Francisco: Holden-Day, Revised edition, 1976.
- [40] M.C. Mackey and L. Glass. Oscillation and chaos in physiological control systems, *Science*, 197(4300), pp. 287-289, 1977.
- [41] B.L. Welch. The generalization of 'Student's' problem when several different population variances are involved, *Biometrika*, 34(1-2), pp. 28-35, 1947.
- [42] M. Hall, E. Frank, G. Holmes, B. Pfahringer, P. Reutemann and I.H. Witten. The WEKA data mining software: an update. *ACM SIGKDD Exploration Newsletter*, 11(1), pp. 10-18, 2009.
- [43] D. Aha and D. Kibler. Instance-based learning algorithms, *Machine Learning*, 6, pp. 37-66, 1991.
- [44] R.J. Quinlan. Learning with Continuous Classes, In: *Proceedings of the 5th Australian Joint Conference on Artificial Intelligence*, Singapore, pp. 343-348, 1992.

Offline and Online Bank Data Synchronization System

Anil Jaiswal¹, Rahul Sonawane¹, Mrs. Sangita Oswal², Mrs. Geocy Shejy².

¹Post-Graduate Student in the Department of MCA, VESIT Mumbai, India.

²Professor in the Department of MCA, VESIT Mumbai, India.

Abstract:

Mobile applications mostly being developed are either for a local or client-server. Though the applications in the future will be developed with cloud in mind, i.e. it will be a native application, the heavy processing and storage is done on the native and later uploaded to cloud, it will deliver only required parts and requested data at runtime and able to run offline. In order to better understand how to facilitate the building of mobile cloud-based applications, we have implemented existing work in mobile computing through the prism of cloud computing principles. We provide an overview of the system, in particular, models of mobile cloud applications. Also, synchronization of offline data with online database will be done.

Keywords: cloud computing, mobile device, remote execution, database synchronization, offloading.

I. INTRODUCTION

Offline and Online Bank Data Synchronization System is used by credit societies to save the money of people with small businesses, or e.g. shopkeepers, vegetable vendors. These people deposit money at the credit society. The cash collector is the person who is working under the credit society. The cash collector collects the money from these people. Cash collector enters the transaction data on his tablet. We are storing our whole data on local storage at first and it will upload the data to Microsoft's cloud, Azure, as soon as the system gets online. Azure services through a global network of Microsoft-managed datacenters [2].

II. LITERATURE SURVEY

2.1. OData Service:

Open Data Service (OData) is a RESTful data access protocol initially defined by Microsoft. Versions 1.0, 2.0, and 3.0 are released under the Promise. It is the data API for Microsoft Azure. SAP NetWeaver Gateway provides OData access to SAP Business Suite and SAP Business Warehouse. IBM WebSphere extreme Scale REST data service can be accessed by any HTTP client using OData. OData client implementations include Microsoft SharePoint 2010, WCF Data Services and Windward Reports. OData is built on the AtomPub protocol and XML where the Atom structure is the envelope that contains the data returned from each OData request. An OData request uses the REST model for all requests. Each REST command is a POST, GET, PUT, PATCH, or DELETE HTTP request (mapping to CRUD) where the specifics of the command are in the URL.

- GET: Get a collection of entities (as a feed document) or a single entity (as an entry document).
- POST: Create a new entity from an entry document.
- PUT: Update an existing entity with an entry document.
- PATCH: Update an existing entity with a partial entry document.
- DELETE: Remove an entity.

Any platform that provides support for HTTP and XML is enough to form HTTP requests to interact with AtomPub. The OData specification defines how AtomPub is used to standardize a typed, resource-oriented CRUD interface for manipulating data sources.

2.2. Cloud Technology:

Cloud computing is a general term for anything that involves delivering hosted services over the Internet. These services are broadly divided into three categories: Infrastructure-as-a-Service (IaaS), Platform-as-a-Service (PaaS) and Software-as-a-Service (SaaS). The name cloud was inspired by the symbol that's often used to represent the Internet in flowcharts and diagrams. Cloud computing relies on sharing of resources to achieve coherence and economies of scale, similar to a utility (like the electricity grid) over a network. At the foundation of cloud computing is the broader concept of converged infrastructure and shared services. Cloud computing, or "the cloud", focuses on maximizing the effectiveness of the shared resources. Cloud resources are usually not only shared by multiple users but are also dynamically reallocated per demand.

2.3. Traditional approach v/s current approach:

In traditional approach, the paper receipt of the transaction was given by the agent and at the end of the day he used to submit the details of the number of transactions carried out that day as well as the money collected from the customers manually to the bank manager. Now days, each agent is allocated with the TRIMAX machine. Agent collects the money from the customers and enters the transactions into the machine. At the end of the day, machine database is synchronized with the bank database. In this way the data gets submitted in the bank. With our system in place, the transaction data locally stored in tablet will be getting uploaded on cloud to report to the bank manager. Hence, the data in the system will be directly compared with the data collected by the Cash collector. So if there is any difference in the data or the cash collected then the Cash collector is answerable for it. For traditional system, the procedure of daily collection is totally dependent upon the cash collector's shoulders. Cash collectors helps in collecting money from the customers and also maintaining the respective account balance sheet, so in most cases it is seen that, there is a mismatch between the bank ledgers and the cash collector's ledgers. This system is vulnerable to vandalism and fraud's. Co-operative society as well as vendor has to believe in cash collector in any condition. So, it is very much easy for cash collector to do fraudulent work and misuse of money. Also cash collectors give customers thermally printed receipt, whose ink gets easily\ rubs off if you rub it quickly, or it will get faded in 2 to 3 days, thus the customers won't have any proof of his investment. So, it is one of the main reasons why co-operative society's or co-operative bank goes down in.

III. BANK APPLICATION ARCHITECTURE:

3.1. Bank application architecture overview:

Bank Application is combination of offline mobile application and online web Application. Mobile Application is used by the Agent to enter the transaction data. That data will be at first locally stored and whenever the system gets online it transfers the data over to cloud storage. Online web application is used by the bank manager, he will be able access to data on cloud storage to check the details of the agent transactions and other information.

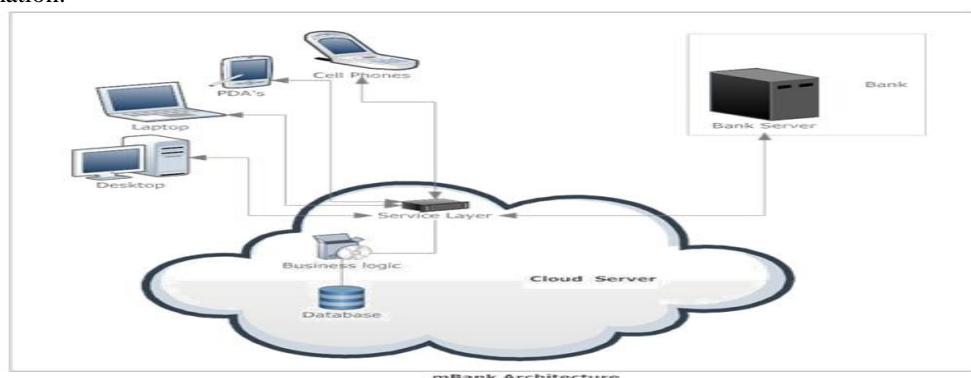


Fig 1 Bank Application Architecture

So it consist of 3 layer architecture

1. Client Side
2. Cloud Server
3. Bank Server

1. Client Side: It can be accessed on any device may that be Computer, Laptop or Mobile with internet connectivity i.e. it is platform independent. There are two types of client one is agent and other one is bank manager.

2. Cloud Server: It is basically the intermediate communication medium between Client and Bank Server. Whatever data entered by the agents through their tablets is synchronised with the cloud server.as well as it will also contain the business logic for this sake.

3. Bank Server: Bank server is taking all the data from cloud storage and updating its data on cloud.

To get the full advantage of potential of cloud computing we need to consider the capabilities and constraints of existing architectures. Most of the applications available for modern mobile devices fall into the following two categories.

3.2. Offline Application.

They act as fat client that processes the presentation and business logic layer locally on mobile devices with data downloaded from backend systems. Only at a certain period, the client and backend system are synchronized. A fat client is a networked application with most resources available locally, rather than distributed over a network as is the case with a thin client. Offline applications, also often called native applications, offer:

- good integration with device functionality and access to its features
- performance optimized for specific hardware and multitasking
- always available capabilities, even without network connectivity

On the other hand, the native applications have many disadvantages:

- no portability to other platforms complex code
- increased time to market

3.3. Online Application.

An online application assumes that the connection between mobile devices and backend systems is available most of the time. Smartphones are popular due to the power and utility of their applications, but there are problems such as cross-platform issues. Here web technologies can overcome them, i.e. applications based on web technology are powerful alternative to native applications. Online mobile applications have the potential to overcome some of the disadvantages of offline applications because they are:

- multi-platform
- directly accessible from anywhere
- knowledge of Web technologies is widespread among developers, greatly minimizing the learning curve required

3.4. Issues with Offline and Online Mobile Applications

Current applications are statically partitioned, i.e. most of the execution and application logic happens either on the device or on backend systems. However, mobile clients could face wide variations and rapid changes in network conditions and local resource availability when accessing remote data and services. As a result, one partitioning model does not satisfy all application types and devices. In order to enable applications and systems to continue to operate in such dynamic environments, mobile cloud applications must react with dynamic adjustment of the computing functionality between the mobile device and cloud depending on circumstances. In other words, the computation of clients and cloud has to be adaptive in response to the changes in mobile environments [1].

So combining the both the systems and taking their pros and neglecting cons this bank architecture is being built.

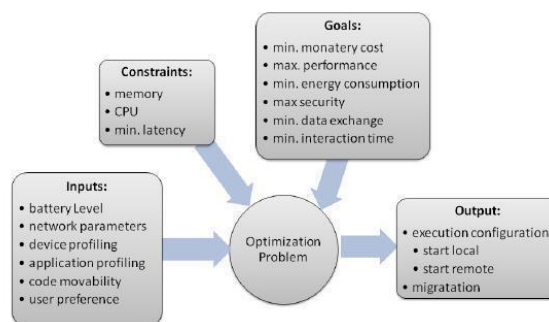


Fig 2 Optimization issues

IV. BENEFITS OF THE SYSTEM

1. This entire system will have web based background for maintaining depositional transactional history.
2. Human efforts will reduce in maintaining the details and entering the daily collections into the system.
3. The system provides security to the customer by providing login id and password.
4. Thus system is fraudulent and trustworthy. Also make the system paperless.

V. RESULT

The wire frame of the system is given below:

The wireframe consists of two main sections. The left section is titled 'ONLINE LOGIN SCREEN' and features the 'Pathpedi Logo' (a picture of yellow flowers). Below the logo are input fields for 'Login ID' and 'Password', both highlighted in blue. There are 'Login' and 'Clear' buttons below these fields. The right section is titled 'OFFLINE Customer Information and Deposit amount form' and contains input fields for 'Agent ID' (value: 1), 'Name' (value: Anil), 'Address' (value: Juinagar), 'Phone No.' (value: 7208550512), and 'Email ID' (value: prasad@gmail.com). Below these fields are 'Genrate Report' and 'Back' buttons. At the bottom of the wireframe is an 'ONLINE Customer Search' section with a search input field containing the letter 'a' and a dropdown list showing 'Yadnesh', 'Anil', and 'Harish'.

Fig 3 Wire Frame of the system.

VI. CONCLUSION

In this paper, we have covered several representative mobile cloud approaches. Other related work exists, but the purpose of this paper is to give an overview of the wide spectrum of mobile cloud computing possibilities. None of the existing approaches meets completely the requirements of mobile clouds. Native (offline) and web-based (online) applications are the two extremes of mobile applications. We believe that the full potential of mobile cloud applications lies in between these two extremes, while dynamically shifting the responsibilities between mobile device and cloud. Several approaches have shown how to achieve it, e.g., by replicating whole device software image or offloading parts of the application. The offloading can happen to some remote data centre, nearby computer or cluster of computers, or even to nearby mobile devices. Moreover, due to the unstable mobile environments, many factors need to be incorporated in a cost model, and fast predictive optimizing algorithms decide upon the best application execution. To simplify the development a convenient, but effective, programming abstraction is required.

REFERENCES

- [1] D. Kristol, HTTP State Management Mechanism, February 1997.
- [2] 2012 Sixth International Conference on Innovative Mobile and Internet Ser-vices in "Ubiquitous Computing".
- [3] Android Wireless Application Development: Volume I Android Essentials, By Lauren Darcey, Shane Conder.
- [4] <http://azure.microsoft.com/en-us/>

Big Data and Information Security

Gang Zeng

(Police Information Department, Liaoning Police College, Dalian, China)

ABSTRACT:

With the development of application of Internet/Mobile Internet, social networks, Internet of Things, big data has become the hot topic of research across the world, at the same time, big data faces security risks and privacy protection during collecting, storing, analyzing and utilizing. This paper introduces the functions of big data, and the security threat faced by big data, then proposes the technology to solve the security threat, finally, discusses the applications of big data in information security.

KEYWORDS: *big data, security risks, information security, information security technology*

I. INTRODUCTION

With the deepening of Internet applications, social networks and internet of things, produced a huge amount of data, which we called big data. It makes the analysis and application of the data more complex, and difficult to manage. These data, including text, images, audio, video, Web pages, e-mail, microblogging and other types, Among them, 20% are structured data, 80% are semi-structured and unstructured data.

big data is large and complex, so it is difficult to deal with the existing database management tools or data processing application. Why do we collect and analyze big data? Because we can get the benefit from it.

(1) to Acquire Knowledge.

Because of big data contains a large number of original, true information, big data analysis can effectively get rid of individual differences, to help people through the phenomenon, more accurately grasp the law behind the things.

(2) to Presume the Trend.

Using the knowledge, we can more accurately predict the natural or social phenomenon. Google predicted the occurrence trend of flu around the world, through the statistics of search for influenza information.

(3) to Analyze Personality Characteristics.

Commercial enterprise collect information on all aspects of customers for a long time, to analyze the user behavior law, more accurately portray the individual characteristics, to provide users with better personalized products and services, and more accurate advertising recommended.

For example, e-commerce sites now use Big Data technology record customer browsing and purchasing history, to guess his interest, and recommend products for him, this may be his interest.

(4) to Discern Truth by Analyzing.

In the network, data sources is diverse, type is rich, so the authenticity can't be guaranteed. At the same time, the spread of information on the Internet is more convenient, so the damage caused by false information on the Internet is greater. Due to the huge amount of data in the big data environment, to a certain extent, it can help discern truth by analyzing the data.

Big data bring the benefits to us, but also bring the questions of data security and privacy protection, since the emergence of big data technology, a large number of security incidents have been occurred, these incidents sounded the alarm for the society: We must study the security question of big data.

II. BIG DATA BRING THREATS TO THE INFORMATION SECURITY

Science and technology is a double-edged sword. Both of the security issues and the value brought by big data become the center of people's attention. Compared with the traditional information security issues, the challenge for big data security is mainly reflected in the following aspects.

2.1. Big Data Increase the Risk of Privacy Leakage

The collection of big data inevitably increases the risk of leakage of user privacy. Because it contains a large number of user information in the data, the development and utilization of big data is very easy to infringe the privacy of citizens, the technical threshold is greatly reduced. The privacy of citizens will be used poisonously.

The cause of information leakage is various, it can be summarized as follows:

(1) The abuse of data leads to the privacy leakage

Big data relates to several areas and departments, and relates to data collecting, storing, processing, analyzing, reporting and other processes, in this process, if the abuse of data will cause privacy leakage. For example, internal staff of data center do not abide by the professional ethics, abuse their functions and powers, release the data of the sensitive department, persons and events to the public, resulted in privacy leakage. When big data is shared among multiple relational departments, this should be also a cause of privacy leakage. Data has a life cycle, at the end of its life cycle, if it does not be effectively destroyed, sniffer can get the data by social engineering, results in privacy leakage.

(2) Analysis and use of data causes privacy leakage

One of the distinctive features of big data is a huge amount of data, the diversity of data source. When analyzing the data, data from different sources are integrated, we may get an unexpected result which can't be got from a single data source. A classic case of privacy leakage in big data environment, the owner of retail store know that his neighbor girl is pregnant early than her parents, and mailed advertising to her, All these are obtained from the analysis of the sales records.

2.2. Big Data Becomes the Carrier of Advanced Persistent Threat

APT is a kind of advanced persistent threat, It's a long time of the attack, the attack process is complex and difficult to find. The main features of APT is that the space to attack is very wide, long duration, single point concealment ability is very strong.

Traditional protection policies is difficult to detect hacker attacks behind big data. Traditional threat detection is based on a real-time feature matching detection on a single point, but APT is an ongoing process, without obvious feature to be detected in real-time, so it can't be detected in real time. Meanwhile, APT code hidden in big data is also difficult to find. In addition, an attacker can also use social network and system vulnerabilities to attack.

Hackers can use big data to expand the attack effect, this is mainly reflected in three aspects:

(1) Hackers can launch a botnet attack using big data server, they may control millions of puppet machine and attack, a single point attack has not such aggressivity.

(2) Hackers can enlarge attack effect by controlling the key nodes;

(3) Hackers can hide data for attacking in large data, which makes difficulty to analysis of security vendors. Any misguiding hacker set, will lead to deviation from the proper direction of safety monitoring.

2.3. Big Data Is Not Necessarily Credible

Because big data is original, the general view is that the big data is true and reliable, the data itself is a fact. In fact, this is not necessarily true, as people can't always believe their eyes.

An important factor affecting the credibility of big data is the correct level of data, If the data comes from the real and reliable production processes, then these data is credible, but if these data is fabricated for a special purpose, so these data is untrusted, because incorrect data will lead to erroneous conclusions .

For example, in some review sites, the real reviews information and bogus reviews mixed together, the user is difficult to distinguish between true and false, and sometimes make wrong judgments based on false reviews, to choose inferior products and services.

Another factor is the gradual distortion in the data dissemination. Data collection process under manual intervention may introduce errors, data distortion due to errors and deviations, and it ultimately affects the accuracy of the results of data analysis. Changes of versions of the data is another factor of data distortion, because of the different versions of the data, users have different understand to the same data, finally, errors will occur.

2.4. How to Achieve Access Control for Big Data

Access control is an effective method to realize data controlled sharing, it is divided into discretionary access control, mandatory access control and role-based access control. While in big data environment, it is difficult to preset the role, to realize the role and to predict the actual authority of each role. Discretionary access control is unable to meet the diversity of the permissions due to the diversity of users, mandatory access control is unable to meet the dynamics of authority, role-based access control is not able to effectively match the role and the corresponding permissions. Therefore, a new security access control mechanisms must be adopted to protect data in big data environment.

III. SECURITY TECHNOLOGY IN BIG DATA ENVIRONMENT

For the security risks of big data, we need to address the security issues of big data from the following points: data privacy protection technology; data integrity and trusted technology; access control technology.

3.1. Data Privacy Protection Technology

To protect the privacy of big data, even if the data with privacy leak, the attacker can't obtain the effective value of data. We can use data encryption and Data anonymity technology

(1) Data Encryption Technology

Data encryption technology is an important means to protect data confidentiality, it safeguards the confidentiality of the data, but it cut down the performance of the system at the same time. The data processing ability of big data system is fast and efficient, which can satisfy the requirements of the hardware and software required for encryption. So the homomorphic encryption has become a research hotspot in data privacy protection.

The homomorphic encryption is a model for the calculation of the cipher text, avoiding the encryption and decryption in the unreliable environment, and directly operation on the cipher text. Which is equivalent to the procedure of processing the data after decryption, then encrypting it. Homomorphic encryption is still in the exploratory stage, the algorithm is immature, low efficiency, and there is a certain distance away from practical application.

(2) Data Anonymity Technology

Data anonymity is another important technology for privacy protection, Even if the attacker gets the data that contains the privacy, he can't get the original exact data, because the value of the key field is hidden. However, in the background of big data, the attacker can obtain data from multiple sources, then associate the data from one source with another source, then will find the original meaning of the hidden data.

(3) Generalization Technology

The third technology of privacy protection is generalization technology, which is to generalize the original data, so that the data is fuzzy, so as to achieve the purpose of privacy protection. For example: I live in 3-13-2 No. 187 Guangyuanli Lane Xuanwu District Beijing. This address is very detailed, now we change the address to the city of Beijing, so that the value of address has become vague, so as to achieve the purpose of privacy protection.

3.2. Access Control Technology

Big data contains a wealth of information resources, all professions and trades have great demand of the data, so we must manage access rights of big data carefully. Access control is an effective means to achieve controlled sharing of data, but in big data environment, the number of users is huge, the authority is complex, and a new technology must be adopted to realize the controlled sharing of data.

(1) Role Mining

Role-based access control (RBAC) is an access control model used widely. By assigning roles to users, roles related to permissions set, to achieve user authorization, to simplify rights management, in order to achieve privacy protection. In the early, RBAC rights management applied "top-down" mode: According to the enterprise's position to establish roles,

When applied to big data scene, the researchers began to focus on "bottom-up" mode, that is based on the existing "Users - Object" authorization, design algorithms automatically extract and optimization of roles, called role mining.

In the big data scene, using role mining techniques, roles can be automatically generated based on the user's access records, efficiently provide personalized data services for mass users. It can also be used to detect potentially dangerous that user's behavior deviates from the daily behavior.

But role mining technology are based on the exact, closed data set, when applied to big data scene, we need to solve the special problems: the dynamic changes and the quality of the data set is not higher.

(2) Risk Adaptive Access Control

In big data scene, the security administrator may lack sufficient expertise, Unable to accurately specify the data which users can access, risk adaptive access control is an access control method for this scenario. By using statistical methods and information theory, define Quantization algorithm, to achieve a risk-based access control. At the same time, in big data environment, to define and quantify the risk are more difficult.

3.3. Data Provenance technology

Due to the diversification of data sources, it is necessary to record the origin and the process of dissemination and calculation, provide additional support for the latter mining and decision.

Before the emergence of the concept of big data, Data Provenance technology has been widely studied in database fields. Its purpose is to help people determine the source of the data in the data warehouse.

The method of data provenance is labeled method, through the label, we can know which data in the table is the source, and can easily checking the correctness of the result, or update the data with a minimum price.

In the future, data provenance technology will play an important role in the field of information security. But data provenance technology for big data security and privacy protection also need to solve the following two questions: 1, The balance between privacy protection and data provenance;2, to protect the security of data provenance technology itself.

IV. APPLICATION OF BIG DATA TECHNOLOGY IN INFORMATION SECURITY

4.1 Threat Discovery Technology Based on Big Data

Compared with the traditional security system, the big data technology used in the security system, can find the security threat earlier. For example: big data technology can detect abnormal behavior in the network, predict the attack behavior, and analyze the source of the attack. By analyzing the email, social network information, you can analyze the disgruntled employees in your enterprise, and make timely plans to prevent security incidents.

Security analysis techniques using big data, has the following characteristics:

(1) Big Data Is More Suitable For Security Analysis

The core technology of safety analysis is the analysis of safety behavior and security incidents, this often come from the analysis of the log, and big data technology is more suitable for the data collection, storage, analysis of the log and other unstructured data. The result of the analysis is very valuable for the security protection, and can also be visualized.

(2) The Range of Content Analysis Is Broader

The security monitoring system using big data technology can collect social network data, personally identifiable information, track information of travel and driving, financial information, call ticket, e-mail information, shopping information, medical information, enterprises business information. According to these information, some abnormal incidents related to security can be analyzed, and steps are taken to prevent security incidents happening.

(3) The time span of the analysis is longer

Analysis of security incidents tend to have a very long time span, it requires a lot of computing power and a large amount of data. The traditional threat analysis system can not meet the requirements of computing power, but the threat analysis system using big data has a variable resource pool, and can analyze vast amounts of data, so as to predict the security incidents as soon as possible, such as APT attack.

(4) The prediction of threats

We always want to predict the security incidents as early as possible, and prevent them happening. The traditional threat analysis system has small amount of data, small range, short time span, and can't predict the security incidents within a long time span and a wide range. The threat analysis system using big data technology can predict the impending threat, according to the characteristics of the security incident.

(5) Detection of unknown incidents

Based on historical experience, we can detect security incidents happened before, but the world is constantly changing, and new security incidents may occur. The analytical work in traditional threat analysis system are carried out by experienced analysts, they mostly make judgments based on historical incidents, so that they can't detect the unknown incident. The security incidents are often interrelated, the threat analysis system using big data technology can detect the unknown security incidents, according to the relation between security incidents, and not a causal relationship, for example: a web site, it has been running very well, recently the ability to provide services constantly reduced, there were no security incident that have been occurred in history, then we can predict that the web site may be attacked by unknown way.

4.2 The Identity Authentication Technology by Behavior Characteristic Based on Big Data

Traditional authentication technologies rely on three ways for certification: Who I am (biometric authentication), what do I know (password authentication), what I have (ID card). In the big data environment, users can be authenticated by behavioral characteristics. This is different from the previous authentication technology, it is difficult for user to pass authentication by feature forgery, at the same time the burden on the user will be reduced, the user needn't remember the complex password, or with id card.

But, this authentication method requires a training data set of user's behavioral characteristics, in the initial stage, it is necessary to collect data and form the training data set which authentication needs, this may impact on the operation of the system.

4.3 Authenticity Analysis Based on Big Data

Above, we discussed that big data is not necessarily true, the real data on the security will have a certain impact, untrue data will impact on security. We can analyze the authenticity of the data by big data technology, and remove false data. For example: using big data, we can distinguish which mail is spam, which comment in comment network is false comment, which data collected in a production system is wrong.

V. CONCLUSION

This paper first introduces the function of big data, and then introduces the security threat faced by big data, and proposes the technology to solve the security threat, finally, discusses the applications of big data in information security. Of course, with the development of big data technology, new security threat may appear, we need to find new solutions and technologies to solve it.

ACKNOWLEDGEMENT

This work was partly supported by general scientific research project of education department of Liaoning Province of China (No. L2013490).

REFERENCES

- [1] FENG Deng-Guo, ZHANG Min, LI Hao. Big Data Security and Privacy Protection[J]. Chinese Journal of Computers, 2014,37(1):246-258.
- [2] MA Li-chuan, PEI Qing-qi, LENG Hao, LI Hong-ning. Survey of Security Issues in Big Data[J]. Radio Communications Technology, 2015,41(1):1-7.
- [3] Hu Kun, Liu Di, Liu Minghui. Research on Security Connotation and Response Strategies for Big Data[J]. Telecommunications Science, 2014(2):112-117,122.
- [4] WANG Yu-long, ZENG Meng-qi. Big Data Security based on Hadoop Architecture[J]. Information Security and Communications Privacy, 2014(7):83-86.
- [5] Big Data Working Group. Big Data Analytics for Security Intelligence[EB/OL]. <https://www.cloudsecurityalliance.org/research/big-data>.
- [6] Guillermo Lafuente. The big data security challenge[J]. Network Security,2015.(1):12-14.
- [7] Hrestak D, Picek S. Homomorphic Encryption in the Cloud [C] // 2014 37th International Convention on Information and Communication Technology, Electronics and Micro electronics (MIPRO), 2014: 1400-1404.
- [8] L.D. Cohen. NOTE On Active Contour Models and Balloons. Computer Vision and Image Processing: Image Understanding, 53:211-218, March 1991.

Emerging Trend of Security Testing to Make Application Robust

Mr. Shiv kumar Goel¹, Prasad Kuvalekar²

¹Professor in the Department of MCA, VESIT Mumbai, India.

²Post-Graduate Student in the Department of MCA, VESIT Mumbai, India.

ABSTRACT:

Typical security requirements may include specific elements of confidentiality, integrity, authentication, availability, authorization and non-repudiation. Actual security requirements tested depend on the security requirements implemented by the system. Security testing as a term has a number of different meanings and can be completed in a number of different ways. As such a Security Taxonomy helps us to understand these different approaches and meanings by providing a base level to work from.

Keywords: Attacks, Security testing, software assurance, SQL injection, Vulnerabilities, Web application

I. INTRODUCTION

Security testing is necessary because it has a distinct relationship with software quality. Just because software meets quality requirements related to functionality and performance, it does not necessary mean that the software is secure. The inverse however is true: i.e. software that is secure is software with added resiliency, thus software of higher quality. Poor architecture and implementation of the web application cannot assure the CIA aspect of software assurance, which would otherwise indicate the resiliency quality of the software.



Fig. 1 Disclosure Strategies.

Vulnerabilities in web applications are now the largest source of enterprise security attacks. Web application vulnerabilities accounted for over 55% of all vulnerabilities disclosed in 2010, according to an IBM X-Force study. That may be the tip of the iceberg as the study includes only commercial web applications.¹

Stories about compromised sensitive data frequently mention culprits such as “cross-site scripting,” “SQL injection,” and “buffer overflow.” Vulnerabilities like these often fall outside the traditional expertise of network security managers. The relative obscurity of web application vulnerabilities thus makes them useful for attacks. As many organizations have discovered, these attacks will evade traditional enterprise network defenses unless you take new precautions.



Fig.2 Top hacking Countries

II. LITERATURE SURVEY

2.1 Overview of Web Application Security

Attacks on vulnerabilities in web applications began appearing almost from the beginning of the World Wide Web, in the mid-1990s. Attacks are usually based on fault injection, which exploits vulnerabilities in a web application's syntax and semantics. Using a standard browser and basic knowledge of HTTP and HTML, an attacker attempts a particular exploit by automatically varying a Uniform Resource Indicator (URI) link, which in turn could trigger an exploit such as SQL injection or cross-site scripting.

`http://example/foo.cgi?a=1`
`http://example/foo.cgi?a=1'` Example of SQL Injection
`http://example/foo.cgi?a=<script>...` Example of Cross-site Scripting (XSS)

Some attacks attempt to alter logical workflow. Attackers also execute these by automatically varying a URI.

`http://example/foo.cgi?admin=false`
`http://example/foo.cgi?admin=true` Example of increasing privileges

Fig.3 SQL injection

A significant number of attacks exploit vulnerabilities in syntax and semantics. You can discover many of these vulnerabilities with an automated scanning tool. Logical vulnerabilities are very difficult to test with a scanning tool; these require manual inspection of web application source code analysis and security testing. Web application security vulnerabilities can stem from misconfigurations, bad architecture, or poor programming practices within commercial or custom application code. Vulnerabilities may be in code libraries and design patterns of popular programming languages such as Java, .NET, PHP, Python, Perl, and Ruby. These vulnerabilities can be complex and may occur under many different circumstances. Using a web application firewall might control effects of some exploits but will not resolve the underlying vulnerabilities.

2.2.4 Command Execution – hijacks control of web application

- >> Buffer Overflow attacks alter the flow of an application by overwriting parts of memory.
- >> Format String Attack alters the flow of an application by using string formatting library features to access other memory space.

Security Testing

- >> LDAP Injection attacks exploit web sites by constructing LDAP statements from user-supplied input.
- >> OS Commanding executes operating system commands on a web site by manipulating application input.

2.2.5 Information Disclosure – shows sensitive data to attackers

- >> Directory Indexing is an automatic directory listing / indexing web server function that shows all files in a requested directory if the normal base file is not present.
- >> Information Leakage occurs when a web site reveals sensitive data such as developer comments or error messages, which may aid an attacker in exploiting the system.
- >> Path Traversal forces access to files, directories and commands that potentially reside outside the web document root directory.
- >> Predictable Resource Location uncovers hidden web site content and functionality.

2.2.6 Logical Attacks – interfere with application usage

- >> Abuse of Functionality uses a web site’s own features and functionality to consume, defraud, or circumvent access control mechanisms.
- >> Denial of Service (DoS) attacks prevents a web site from serving normal user activity.
- >> Insufficient Anti-automation is when a web site permits an attacker to automate a process that should only be performed manually.
- >> Insufficient Process Validation permits an attacker to bypass or circumvent the intended flow of an application.

III. TESTING APPROACH

Criteria	Security Testing Approach	
	Black Box	White Box
Determination of root cause	Most likely to address the symptoms than the root cause.	Exact line of code or design issue causing the vulnerability can be identified.
Extent of code coverage	Limited as the analysis is behavioral; not all code paths may be covered.	Greater as the source code and configuration is available for review.
Detection of logic flaws	Not knowing the normal behavior of the software; anomalous behavior may not necessarily indicate flaws in logic.	The availability of design and architectural documents besides code can be used to detect logic flaws.
Issues with deployment	Assessment can be performed in pre- as well as post-deployment production or production-like simulated environment, giving insight into any potential issues after deployment.	Assessment is performed in pre-deployment environments usually providing limited issues pertaining to configuration and change management.

Fig.5 Security Testing Approach

IV. SECURITY TESTER

Security testers are a breed all their own. In addition to an anti-developer attitude, a good security tester's profile includes a creative mind to think out of the box. A good security tester thrives and excels when posed with challenges.

Security Testing

"Good security tester's profile includes a creative mind to think out of the box."

They have a constant thirst for learning newer attack techniques and coming up with all possible combinations of attack as they seek to exploit weaknesses in the software or system. They usually have selfdriven personalities and their motivations are often related to ego than materialistic pursuits. With appropriate training and skills on software security throughout the SDLC, these testers become very valuable to the organization.

V. TYPES OF SECURITY TESTING

Following are the types of security testing as per Open Source Security Testing methodology manual. They are explained as follows:

Vulnerability Scanning:

This is done through automated software to scan a system against known vulnerability signatures.

Security Scanning:

It involves identifying network and system weaknesses, and later provides solutions for reducing these risks. This scanning can be performed for both Manual and Automated scanning.

Penetration testing:

This kind of testing simulates an attack from malicious hacker. This testing involves analysis of a particular system to check for potential vulnerabilities to an external hacking attempt.

Risk Assessment:

This testing involves analysis of security risks observed in the organization. Risks are classified as Low, Medium and High. This testing recommends controls and measures to reduce the risk.

Security Auditing: This is internal inspection of Applications and Operating systems for security flaws. Audit can also be done via line by line inspection of code

Ethical hacking:

It's hacking Organization Software systems. Unlike malicious hackers who steal for their own gains, the intent is to expose security flaws in the system.

Posture Assessment: This combines Security scanning, Ethical Hacking and Risk Assessments to show an overall security posture of an organization.

Vulnerability Assessment:

This is a security audit and privilege access and administrator assistance is required for configuration audit. This is done directly on the system with physical and logical access. System configuration checking and vulnerability scanning is performed to find out weaknesses, vulnerabilities and mis-configuration in the target hosts.

Penetration Testing:

Penetration Testing (PT) is normally done remotely from public domain (Internet) and also can be done from internal network to find out exploitable vulnerabilities from internal network. No privilege access is required. Series of testing conducted like information gathering from public domain, port scanning, system fingerprinting, service probing, vulnerability scanning, manual testing, password cracking etc. using state-of-the-art tools (commercial and open source) and techniques used by hackers with objective to unearth vulnerabilities and weaknesses of the IT infrastructure.

Application Security Assessment:

Different software testing techniques are employed to unearth application security vulnerabilities, weaknesses and concerns related to Authentication, Authorization, Session Management, Input/output Validation, Processing Errors, Information Leakage, Denial of Service etc. Typical issues which may be discovered in an application security audit include Cross-site scripting, Broken ACLs/Weak passwords, Weak session management, Buffer overflows, Forceful browsing, CGI- BIN manipulation, Form/hidden field manipulation, Command injection, Insecure use of cryptography, Cookie poisoning, SQL injection, Server mis-configurations, Well-known platform vulnerabilities, Errors triggering sensitive information leak etc. For web applications OWASP (Open Web Application Security Project) guidelines is used for the assessment. All the assessment are carried out using both state-of-the-art tools and manual testing methods.

Security Testing

VI. STRATEGIES

Since security testing is not an optional activity, it is imperative to incorporate this vital activity into the SDLC. Security testing should be made an integral part of the overall testing process. It must be included into the scope of the software development project, even before the code for that software is written. A proven strategy is to incorporate a library of security tests into the enterprise project template (assuming you already have one) and maintain these tests in the centralized test and bug tracking database/software. This will ensure that all projects will, at a bare minimum, automatically inherit any tests that need to be run as part of the project. Another strategy is to start generating the test cases during the requirement phase of the SDLC itself. When the requirements are known, there is no need to wait until code is complete to generate all the test cases. This proactive approach to testing gives time for both functional and security test cases to be generated in advance and the testing phase can be used efficiently to conduct these test cases.

VII. USING TOOLS TO IMPLEMENT WEB APPLICATION SECURITY

There are many kinds of scanners and other tools for IT security, audit, and operations. Our focus here is the web application security (WAS) scanner. Its fundamental purpose is to automatically examine custom web applications that respond to dynamic web page requests with protocols like hypertext transfer protocol (HTTP).

Some scanners use the „point-and-shoot“ method of operation without imposing particular parameters. Others need to be „trained“ or configured for a particular environment. However it works, the scanner should be able to find all vulnerabilities in all web applications with a high degree of accuracy. To miss these, or present false positive or false negative identifications is to leave a web application exposed to exploitation.

VIII. CONCLUSION

Software assurance is comprised of reliability, recoverability, and resiliency aspects of the software. Software testing must address all of these. Without testing the software for its security capabilities, it is only a matter of time before software will be exploited (hacked). Software testing for functionality should always be augmented with security testing for resiliency. Security is an attribute of quality, and software that is less prone to getting hacked can be said to be of higher quality than software that doesn't take security into account. Security testing can be used to achieve software assurance – akin to setting up the chess board so that you are able to defend your organization and avoid checkmate.

REFERENCES

- [1] "Improving Web Application Security: Threats and Countermeasures". Microsoft Corporation. June 2003.
- [2] "Testing and Comparing Web Vulnerability Scanning Tools for SQL Injection and XSS Attacks" (PDF). Fonseca, J.; Vieira, M.; Madeira, H., Dependable Computing, IEEE. Dec 2007.
- [3] "The Web Hacking Incidents Database". WASC. January 2010.
- [4] "Web Application Vulnerability Scanners". NIST.
- [5] "Source Code Security Analyzers". NIST.
- [6] "Web application firewalls for security and regulatory compliance". Secure Computing Magazine. February 2008.

Design of Full Order Optimal Controller for Interconnected Deregulated Power System for AGC

Mrs. Upma Gupta¹, Mrs. S.N.Chaphekar²

¹ M.E. Scholar, PES's Modern College of Engineering, Pune India

² Assistant Professor, PES's Modern College of Engineering, Pune India

Abstract

This paper presents the design and simulation of full order optimal controller for deregulated power system for Automatic Generation Control (AGC). Traditional AGC of two-area system is modified to take in to the effect of bilateral contracts on the system dynamics. The DISCO participation matrix defines the bilateral contract in a deregulated environment. This paper reviews the main structures, configurations, modeling and characteristics of AGC in a deregulated environment and addresses the control area concept in restructured power Systems. To validate the effectiveness of full order optimal controller, a simulation has been performed using MATLAB and results are presented here. The results for LFC and AGC for a deregulated interconnected power systems shows that the optimal full order controllers perform better than classical integral order controllers .

Keywords: Automatic Generation Control, Area Control Error, ACE Participation Factor, Bilateral Contracts, Contract Participation Factor, Deregulation, DISCO Participation Matrix, Full Order Optimal Controller, Load Frequency Control.

I. Introduction

In the electric power system load demand of the consumer always keeps on changing, hence the system frequency varies to its nominal value and the tie line power of the interconnected power system changes to its scheduled value. AGC is responsible to control the frequency to its nominal value and maintain the tie line power to its scheduled value, at the time of load perturbation in the system. In the conventional power system the generation, transmission and distribution are owned by a single entity called a Vertically Integrated Utility (VIU). In the deregulated environment Vertically Integrated Utilities no longer exist. However, the common operational objective of restoring the frequency at its nominal value and tie line power to its schedule value remain the same. In the deregulated power system the utilities no longer own generation, transmission and distribution. In this scenario there are three different entities generation companies (GENCOs), transmission companies (TRASCOS), distribution companies (DISCOs). As there are several GENCOs and DISCOs in the deregulated environment, a DISCO has the freedom to have a contract with any GENCO for transaction of power. A DISCO has freedom to contract with any of the GENCOs in their own area or another area. Such transactions are called "bilateral transactions" and these contracts are made under the supervision of an impartial entity called Independent System Operator (ISO). ISO is also responsible for managing the ancillary services like AGC etc. The objective of this paper is to modify the traditional two area AGC system to take into account the effect of Bilateral Contracts. The concept of DISCO participation matrix is used that helps in the visualization and implementation of Bilateral Contracts. Simulation of the bilateral contracts is done and reflected in the two-area block diagram. The full order optimal controller is used for accomplish the job of AGC i.e to achieve zero frequency deviation at steady state, and to distribute generation among areas so the interconnected tie line power flow match the prescribed schedule and to balance the total generation against the total load.

II. Formulation of Model of AGC for deregulated power system

Consider a two-area system in which each area has two GENCOs (non reheat thermal turbine) and two DISCOs in it. Let GENCO1 GENCO2, DISCO1 and DISCO2 be in area 1 and DISCO3, and DISCO4 be in area 2 as shown in Fig. 1.



Fig. 1: Schematic of a two-area thermal system in deregulated environment

For LFC or AGC conventional model is used which is just the extension of the traditional Elgerd model [3]. In this AGC model, the concept of disco participation matrix (DPM) is included to incorporate the bilateral load contracts. DPM is a matrix with the number of rows equal to the number of GENCOs and number of columns equal to the number of DISCOs in the system. The DPM shows the participation of a DISCO in a contract with GENCO. For the system described in Fig 1, the DPM is given as

$$DPM = \begin{bmatrix} cpf_{11} & cpf_{12} & cpf_{13} & cpf_{14} \\ cpf_{21} & cpf_{22} & cpf_{23} & cpf_{24} \\ cpf_{31} & cpf_{32} & cpf_{33} & cpf_{34} \\ cpf_{41} & cpf_{42} & cpf_{43} & cpf_{44} \end{bmatrix}$$

Where Cpf refers to "contract participation factor." $cpf_{ij} = \frac{\text{Demand of DISCOj from GENCOi}}{\text{Total Demand of DISCOj}}$,

Thus ijth entry corresponds to the fraction of the total load power contracted by DISCO j from GENCO i. The sum of all the entries of particular column of DPM is unity.

Whenever the load demanded by a DISCO changes, it is reflected as a local load in the area to which this DISCO belongs. As there are many GENCOs in each area, ACE signal has to be distributed among them in proportion to their participation in the AGC. "ACE (Area Control Error) participation factor (apf)" are the coefficient factors which distributes the ACE among GENCOs. If there are m no of GENCOs then $\sum_{i=1}^m apf_i = 1$.

In deregulated scenario a DISCO demands a particular GENCO or GENCOs for load power. These demands must be reflected in the dynamics of the system. Turbine and governor units must respond to this power demand. Thus, as a particular set of GENCOs are supposed to follow the load demanded by a DISCO, information signals must flow from a DISCO to a particular GENCO specifying corresponding demands. Here, we introduce the information signals which were absent in the conventional scenario. The demands are specified by (elements of DPM) and the pu MW load of a DISCO. These signals carry information as to which GENCO has to follow a load demanded by which DISCO.

The block diagram for two area AGC in a deregulated power system is shown in Fig 2. In this model the schedule value of steady state tie line power is given as

$$\Delta P_{\text{tie1-2,scheduled}} = (\text{demand of DISCOs in area 2 from GENCOs in area1}) - (\text{demand of DISCOs in area 1 from GENCOs in area2})$$

At any given time, the tie line power error, $\Delta P_{\text{tie1-2,error}}$ is defined as-

$$\Delta P_{\text{tie1-2,error}} = \Delta P_{\text{tie1-2,actual}} - \Delta P_{\text{tie1-2,scheduled}}$$

This error signal is used to generate the respective ACE signals as in the traditional scenario

$$ACE_1 = B_1 \Delta f_1 + \Delta P_{\text{tie 1-2,error}}$$

$$ACE_2 = B_2 \Delta f_2 + \Delta P_{\text{tie 2-1,error}}$$

Where

$$\Delta P_{\text{tie 2-1,error}} = - \frac{P_{r1}}{P_{r2}} \Delta P_{\text{tie 1-2,error}}$$

P_{r1} and P_{r2} are the rated powers of area 1 and area 2, respectively. Therefore

$$ACE_2 = B_2 \Delta f_2 + \alpha_{12} \Delta P_{\text{tie 1-2,error}}$$

$$\text{Where } \alpha_{12} = - \frac{Pr1}{Pr2}$$

In the block diagram shown in figure 2, $\Delta P_{L1,LOC}$ and $\Delta P_{L2,LOC}$ represents the local loads in area 1 and area 2 respectively.

ΔP_{L1} , ΔP_{L2} , ΔP_{L3} and ΔP_{L4} represents the contracted load of DISCO1, DISCO2, DISCO3 and DISCO4 respectively.

III. Design of full order optimal Controller

The theory of optimal control is concerned with operating a dynamic system at minimum cost. The case where the system dynamics are described by a set of linear differential equations and the cost is described by a quadratic functional is called the LQ problem. The optimal control problem for a linear multivariable system with the quadratic criterion function is one of the most common problems in linear system theory. it is defined below:

$$\dot{x} = Ax + Bu \quad \dots\dots\dots(1)$$

Given the completely controllable plant, where x is the $n \times 1$ state vector, u is the $p \times 1$ input vector. A is the $n \times n$ order of real constant matrix and B is the $n \times p$ real constant matrix. Desired steady -state is the null state $x=0$

The control law

$$u = -Kx \quad \dots\dots\dots(2)$$

Where K is $p \times n$ real constant unconstrained gain matrix, that minimizes the quadratic performance index . The design of a state feedback optimal controller is to determine the feedback matrix 'K' in such a way that a certain Performance Index (PI) is minimized while transferring the system from an initial arbitrary state $x(0) \neq 0$ to origin in infinite time i.e., $x(\infty) = 0$. Generally the PI is chosen in quadratic form as:

$$PI = \frac{1}{2} \int_0^{\infty} (x^T Q x + u^T R u) dt \quad \dots\dots\dots(3)$$

where, 'Q' is a real, symmetric and positive semi-definite matrix called as 'state weighting matrix' and 'R' is a real, symmetric and positive definite matrix called as 'control weighting matrix'.

The matrices A, B, Q & R are known. The optimal control is given by $u = -Kx$, 'K' is the feedback gain matrix given by;

$$K = R^{-1} B^T S \quad \dots\dots\dots(4)$$

where, 'S' is a real, symmetric and positive definite matrix which is the unique solution of matrix Riccati Equation:

$$A^T S + S A - S B R^{-1} B^T S + Q = 0 \quad \dots\dots\dots(5)$$

The closed loop system equation is;

$$\dot{x} = Ax + B(-Kx) = (A - BK)x = A_C x \quad \dots\dots\dots(6)$$

The matrix $A - BK = A_C$ is the closed loop system matrix. The stability of closed loop system can be tested by finding eigen values of A_C .

IV. State Space Modeling AGC System in Deregulated Environment

The two area AGC system considered has two individual area connected with a tie line. The deviation in each area frequency is determined by considering the dynamics of governor, turbines, generators and load represented in that area. The state space model of representation of AGC model is given by

$$\dot{x} = Ax + Bu + \Gamma p + \beta q \quad \dots\dots\dots(7)$$

This model of AGC is shown in Fig.2 .Where x is state vector, u is control vector p is disturbance vector and q is the bilateral contract vector. A, B, Γ and β are the constant matrix associated with state control, disturbance and bilateral contract vector respectively.

In our system we can identify total 13 states. All these vectors and matrix are given by -

The State Vector 'x' (13×1), $x = [x_1 \ x_2 \ x_3 \ x_4 \ x_5 \ x_6 \ x_7 \ x_8 \ x_9 \ x_{10} \ x_{11} \ x_{12} \ x_{13}]^T$ where

$$x = [f_1 \ f_2 \ \Delta P_{GV1} \ \Delta P_{GV2} \ \Delta P_{GV3} \ \Delta P_{GV4} \ \Delta P_{M1} \ \Delta P_{M2} \ \Delta P_{M3} \ \Delta P_{M4} \ \int ACE_1 dt \ \int ACE_2 dt \ \Delta P_{ne1-2}]^T ; \quad \dots\dots\dots(8)$$

$$\text{Control Vector 'u' } (2 \times 1) \quad u = [u_1 \ u_2]^T ; \quad \dots\dots\dots(9)$$

$$\text{Disturbance vector 'p' } (2 \times 1) \quad p = [P_{d1} \ P_{d2}]^T ; \quad \dots\dots\dots(10)$$

$$\text{Bilateral Contract Vector 'q' } (4 \times 1) \quad q = [\Delta P_{L1} \ \Delta P_{L2} \ \Delta P_{L3} \ \Delta P_{L4}]^T \quad \dots\dots\dots(11)$$

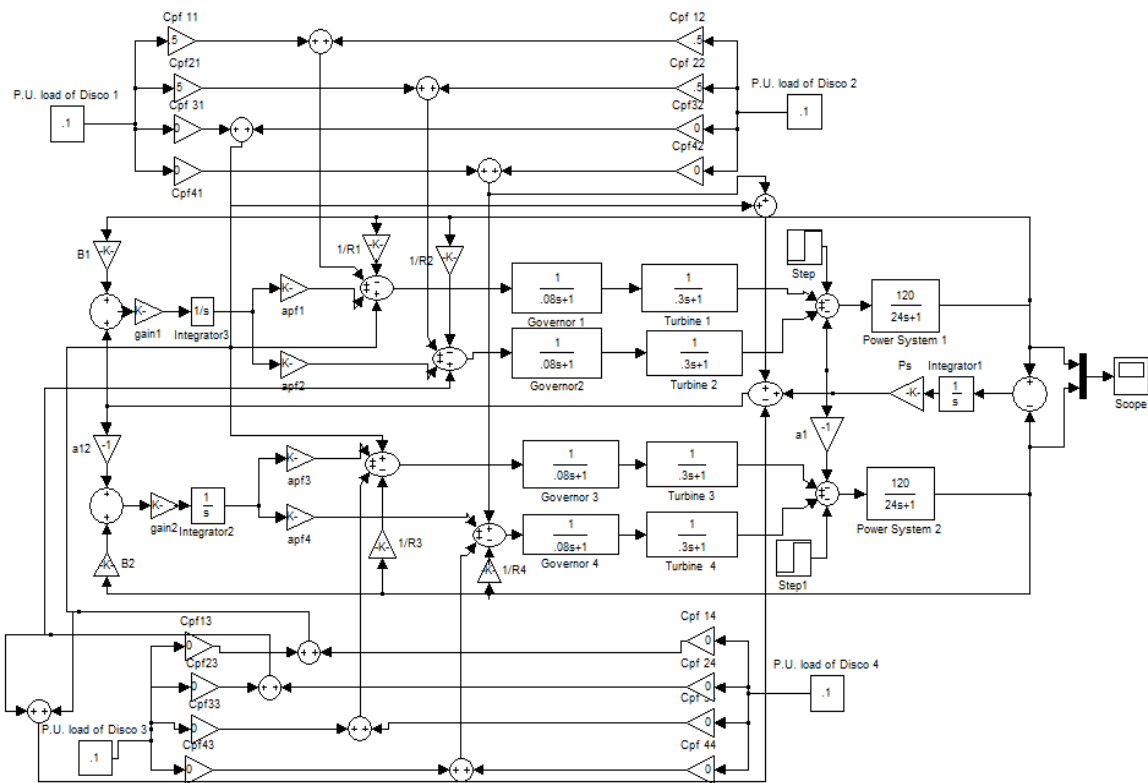


Fig.2: Two area AGC model in deregulated power system

$$A = \begin{bmatrix}
 \frac{-1}{T_{P1}} & 0 & 0 & \frac{k_{P1}}{T_{P1}} & \frac{k_{P1}}{T_{P1}} & 0 & 0 & 0 & 0 & 0 & 0 & 0 & -\frac{k_{P1}}{T_{P1}} \\
 0 & \frac{-1}{T_{P2}} & 0 & 0 & \frac{k_{P2}}{T_{P2}} & \frac{k_{P2}}{T_{P2}} & 0 & 0 & 0 & 0 & 0 & 0 & -\frac{a_{12}k_{P2}}{T_{P2}} \\
 0 & 0 & \frac{-1}{T_{T1}} & 0 & 0 & 0 & \frac{1}{T_{T1}} & 0 & 0 & 0 & 0 & 0 & 0 \\
 0 & 0 & 0 & \frac{-1}{T_{T2}} & 0 & 0 & 0 & \frac{1}{T_{T2}} & 0 & 0 & 0 & 0 & 0 \\
 0 & 0 & 0 & 0 & \frac{-1}{T_{T3}} & 0 & 0 & 0 & \frac{1}{T_{T3}} & 0 & 0 & 0 & 0 \\
 0 & 0 & 0 & 0 & 0 & \frac{-1}{T_{T4}} & 0 & 0 & 0 & \frac{1}{T_{T1}} & 0 & 0 & 0 \\
 \frac{-1}{R_1 T_{g1}} & 0 & 0 & 0 & 0 & 0 & \frac{-1}{T_{g1}} & 0 & 0 & 0 & 0 & 0 & 0 \\
 \frac{-1}{R_2 T_{g2}} & 0 & 0 & 0 & 0 & 0 & 0 & \frac{-1}{T_{g2}} & 0 & 0 & 0 & 0 & 0 \\
 0 & \frac{-1}{R_3 T_{g3}} & 0 & 0 & 0 & 0 & 0 & 0 & \frac{-1}{T_{g3}} & 0 & 0 & 0 & 0 \\
 0 & \frac{-1}{R_4 T_{g4}} & 0 & 0 & 0 & 0 & 0 & 0 & 0 & \frac{-1}{T_{g4}} & 0 & 0 & 0 \\
 -B_1 & 0 & 0 & 0 & 0 & 0 & 0 & 0 & 0 & 0 & 0 & 0 & -1 \\
 0 & -B_2 & 0 & 0 & 0 & 0 & 0 & 0 & 0 & 0 & 0 & 0 & -a_{12} \\
 2\pi T_{12} & -2\pi T_{12} & 0 & 0 & 0 & 0 & 0 & 0 & 0 & 0 & 0 & 0 & 0
 \end{bmatrix}$$

.....(12)

$$B = \begin{bmatrix} 0 & 0 \\ 0 & 0 \\ 0 & 0 \\ 0 & 0 \\ 0 & 0 \\ 0 & 0 \\ \frac{apf_1}{Tg_1} & 0 \\ \frac{apf_2}{Tg_2} & 0 \\ 0 & \frac{apf_3}{Tg_3} \\ 0 & \frac{apf_4}{Tg_4} \\ 0 & 0 \\ 0 & 0 \\ 0 & 0 \\ 0 & 0 \end{bmatrix}, \dots\dots\dots(13)$$

$$\Gamma = \begin{bmatrix} \frac{k_{p1}}{T_{p1}} & 0 \\ 0 & \frac{k_{p2}}{T_{p2}} \\ 0 & 0 \\ 0 & 0 \\ 0 & 0 \\ 0 & 0 \\ 0 & 0 \\ 0 & 0 \\ 0 & 0 \\ 0 & 0 \\ 0 & 0 \\ 0 & 0 \\ 0 & 0 \end{bmatrix} \dots\dots\dots(14)$$

$$\beta = \begin{bmatrix}
 \frac{-k_{p1}}{T_{p1}} & \frac{-k_{p1}}{T_{p1}} & 0 & 0 \\
 0 & 0 & \frac{-k_{p2}}{T_{p2}} & \frac{-k_{p2}}{T_{p2}} \\
 0 & 0 & 0 & 0 \\
 0 & 0 & 0 & 0 \\
 0 & 0 & 0 & 0 \\
 0 & 0 & 0 & 0 \\
 \frac{cpf_{11}}{T_{g1}} & \frac{cpf_{12}}{T_{g1}} & \frac{cpf_{13}}{T_{g1}} & \frac{cpf_{14}}{T_{g1}} \\
 \frac{cpf_{21}}{T_{g2}} & \frac{cpf_{22}}{T_{g2}} & \frac{cpf_{23}}{T_{g2}} & \frac{cpf_{24}}{T_{g2}} \\
 \frac{cpf_{31}}{T_{g3}} & \frac{cpf_{32}}{T_{g3}} & \frac{cpf_{33}}{T_{g3}} & \frac{cpf_{34}}{T_{g3}} \\
 \frac{cpf_{41}}{T_{g4}} & \frac{cpf_{42}}{T_{g4}} & \frac{cpf_{43}}{T_{g4}} & \frac{cpf_{44}}{T_{g4}} \\
 - (cpf_{31} + cpf_{41}) & - (cpf_{32} + cpf_{42}) & + (cpf_{13} + cpf_{23}) & + (cpf_{14} + cpf_{24}) \\
 - a_{12} (cpf_{31} + cpf_{41}) & - a_{12} (cpf_{32} + cpf_{42}) & a_{12} (cpf_{13} + cpf_{23}) & a_{12} (cpf_{14} + cpf_{24}) \\
 0 & 0 & 0 & 0
 \end{bmatrix},$$

.....(15)

V. Design of full Optimal controller for AGC in Deregulated Environment

The design of a state feedback optimal controller is to determine the feedback matrix ‘K’ in such a way that a certain Performance Index (PI) is minimized while transferring the system from an initial arbitrary state $x(0) \neq 0$ to origin in infinite time i.e., $x(\infty) = 0$.

Generally the PI is chosen in quadratic form as given by equation (3)

$$PI = \frac{1}{2} \int_0^\infty (x^T Q x + u^T R u) dt$$

where, ‘Q’ is a real, symmetric and positive semi-definite matrix called as ‘state weighting matrix’ and ‘R’ is a real, symmetric and positive definite matrix called as ‘control weighting matrix’. The matrices Q and R are determined on the basis of following system requirements.

- 1) The excursions (deviations) of ACEs about steady values are minimized. In this model, these excursions are;

$$ACE_1 = B_1 \Delta f_1 + \Delta P_{tie\ 1-2} = B_1 x_1 + x_{13} \quad \text{and} \quad \dots\dots\dots(16)$$

$$ACE_2 = B_2 \Delta f_2 + \Delta P_{tie\ 2-1} = B_2 x_2 + a_{12} x_{13} \quad \dots\dots\dots(17)$$
- 2) The excursions of $\int ACE \ dt$ about steady values are minimized. In this model, these excursions are x_{11} & x_{12} .
- 3) The excursions of control inputs u_1 and u_2 about steady values are minimized.

Under these considerations, the PI takes a form;

$$PI = \frac{1}{2} \int_0^\infty [(B_1 x_1 + x_{13})^2 + (B_2 x_2 + a_{12} x_{13})^2 + (x_{11})^2 + (x_{12})^2 + (u_1)^2 + (u_2)^2] dt \quad \dots\dots(18)$$

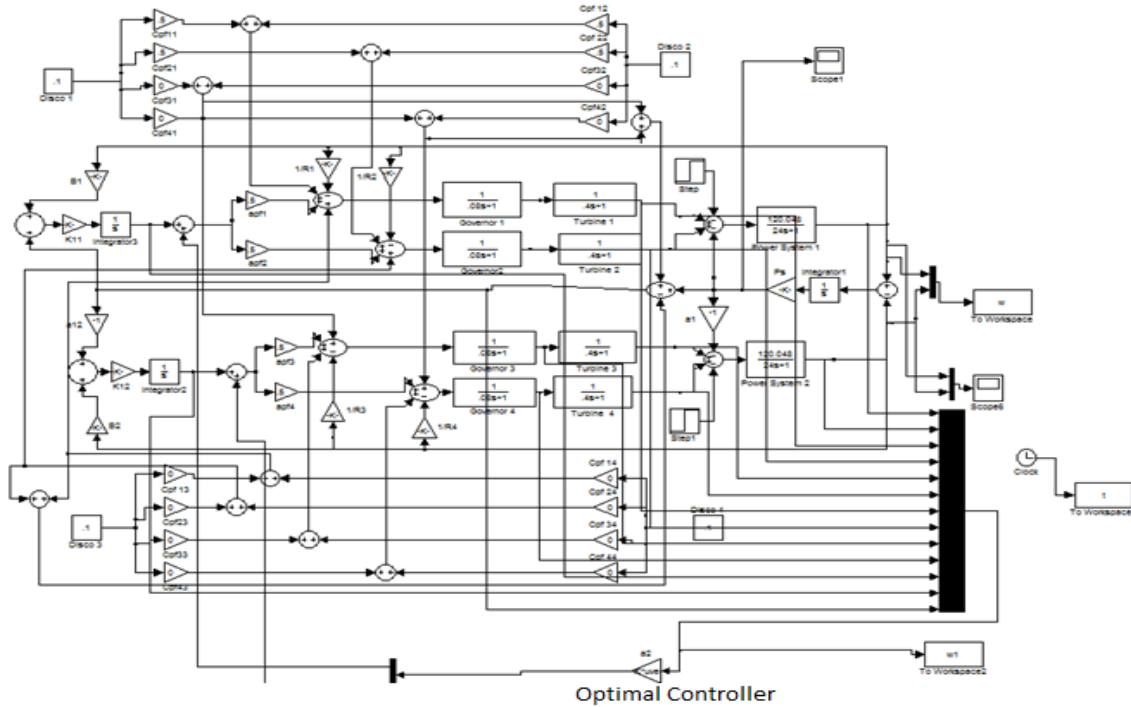


Fig. 3 Simulation model of two area AGC in deregulated system with Optimal Controller
 This gives the matrices Q (13×13) and R (2×2) as:

$$Q = \begin{bmatrix} B_1^2 & 0 & 0 & 0 & 0 & 0 & 0 & 0 & 0 & 0 & 0 & 0 & 0 & B_1 \\ 0 & B_2^2 & 0 & 0 & 0 & 0 & 0 & 0 & 0 & 0 & 0 & 0 & 0 & a_{12} B_2 \\ 0 & 0 & 0 & 0 & 0 & 0 & 0 & 0 & 0 & 0 & 0 & 0 & 0 & 0 \\ 0 & 0 & 0 & 0 & 0 & 0 & 0 & 0 & 0 & 0 & 0 & 0 & 0 & 0 \\ 0 & 0 & 0 & 0 & 0 & 0 & 0 & 0 & 0 & 0 & 0 & 0 & 0 & 0 \\ 0 & 0 & 0 & 0 & 0 & 0 & 0 & 0 & 0 & 0 & 0 & 0 & 0 & 0 \\ 0 & 0 & 0 & 0 & 0 & 0 & 0 & 0 & 0 & 0 & 0 & 0 & 0 & 0 \\ 0 & 0 & 0 & 0 & 0 & 0 & 0 & 0 & 0 & 0 & 0 & 0 & 0 & 0 \\ 0 & 0 & 0 & 0 & 0 & 0 & 0 & 0 & 0 & 0 & 0 & 0 & 0 & 0 \\ 0 & 0 & 0 & 0 & 0 & 0 & 0 & 0 & 0 & 0 & 0 & 0 & 0 & 0 \\ 0 & 0 & 0 & 0 & 0 & 0 & 0 & 0 & 0 & 0 & 1 & 0 & 0 & 0 \\ 0 & 0 & 0 & 0 & 0 & 0 & 0 & 0 & 0 & 0 & 0 & 0 & 1 & 0 \\ B_1 & a_{12} B_2 & 0 & 0 & 0 & 0 & 0 & 0 & 0 & 0 & 0 & 0 & 0 & 1 + a_{12}^2 \end{bmatrix} \dots\dots\dots(19)$$

$$R = \begin{bmatrix} 1 & 0 \\ 0 & 1 \end{bmatrix} \dots\dots\dots(20)$$

The matrices A, B, Q & R are known. The optimal controller gain matrix can be obtained by using equations (4) to (6).

VI. Simulation Result

A. Case 1:

Consider a case where all the DISCOs contract with the GENCOs for power as per the following DPM:

$$DPM = \begin{bmatrix} .3 & .5 & .1 & .35 \\ .2 & .5 & .25 & .3 \\ .1 & 0 & .4 & .1 \\ .4 & 0 & .25 & .25 \end{bmatrix}$$

It is assumed that each DISCO demands 0.1 pu MW power from GENCO as defined by *cpfs* in DPM matrix and each GENCO participates in AGC as defined by following *apfs*: $apf_1 = 0.75$, $apf_2 = 0.25$, $apf_3 = 0.5$ and $apf_4 = 0.5$.

The system in figure 3 simulated using the above data and the system parameters given in Appendix -I . The result of the simulation has shown in Figure 4.

The off diagonal elements of DPM corresponds to the contract of a DISCO in one area with a GENCO in another area.

The schedule power on the tie line in the direction from area1 to area2 is -

$$\begin{aligned} \Delta P_{tie1-2,scheduled} &= [\Delta P_{L3}(cpf_{13} + cpf_{23}) + \Delta P_{L4}(cpf_{14} + cpf_{24})] \\ &\quad - [\Delta P_{L1}(cpf_{31} + cpf_{41}) + \Delta P_{L2}(cpf_{32} + cpf_{42})] \\ &= [0.1(0.1+0.25)+0.1(0.3+0.35)] - [0.1(0.1+0.4)+0.1(0+0)] \\ &= 0.05 \text{ pu MW} \end{aligned}$$

The desired generation of a GENCO in pu MW can be expressed in terms of Contract Participation Factor (*cpfs*) and the total demand of DISCOs as

$$\Delta P_{Mi} = \sum_{j=1}^j cpf_{ij} \Delta P_{Lj}$$

Where ΔP_{Lj} is the total demand of DISCO *j* and *cpfs* are given by DPM.

At steady state power generated by GENCOs -

$$\Delta P_{M1} = 0.3(0.1) + 0.5(0.1) + 0.1(0.1) + 0.35(0.1) = 0.125 \text{ pu MW}$$

$$\Delta P_{M2} = 0.125 \text{ pu MW}; \quad \Delta P_{M3} = 0.06 \text{ pu MW}; \quad \Delta P_{M4} = 0.09 \text{ pu MW}$$

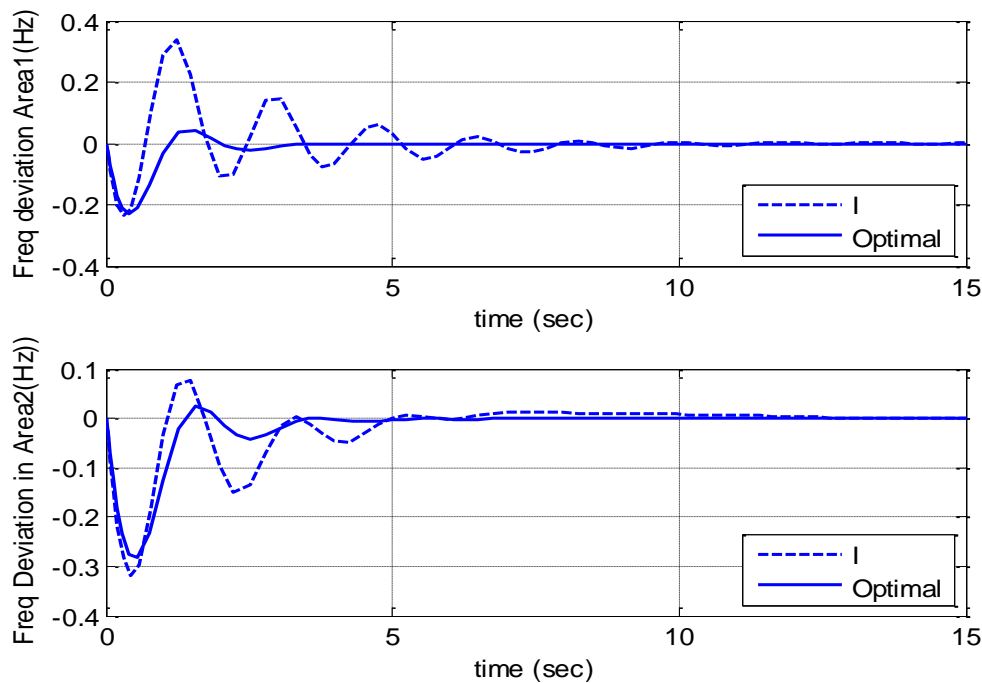


Fig. 4a: Frequency Deviations (Hz) for area 1 & area 2, case1

Fig. 4a shows the dynamic responses of frequency deviations in two areas (i.e., Δf_1 and Δf_2). The frequency deviation in each area goes to zero in the steady state.

The schedule power on the tie line in the direction from area1 to area2 is .05 pu MW. Fig. 4b shows the actual Tie line power flow between two area at steady state is also .05 pu MW. So the deviation in tie line power at steady state become zero .

Fig. 4c & 4d show the power generated by GENCO1, GENCO2, GENCO3 & GENCO4 in steady state. The results are matching from our calculations.

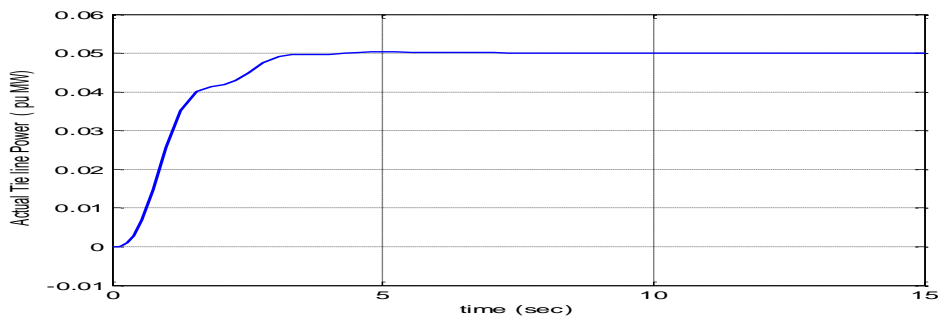


Fig.4b: Actual Tie line power (pu MW), case 1

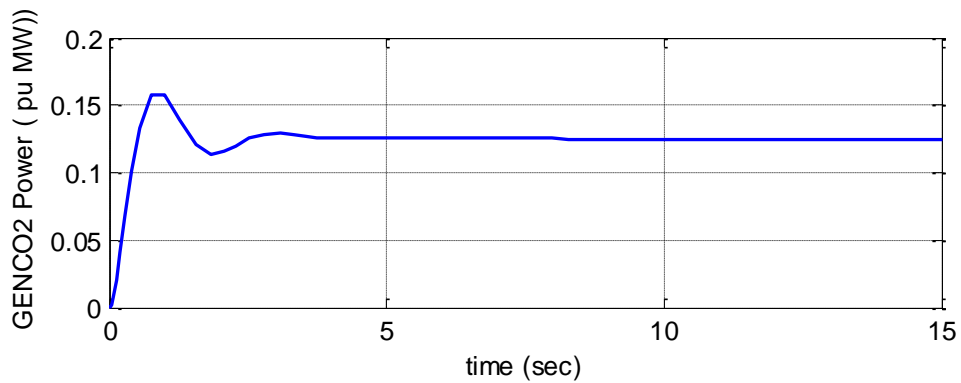
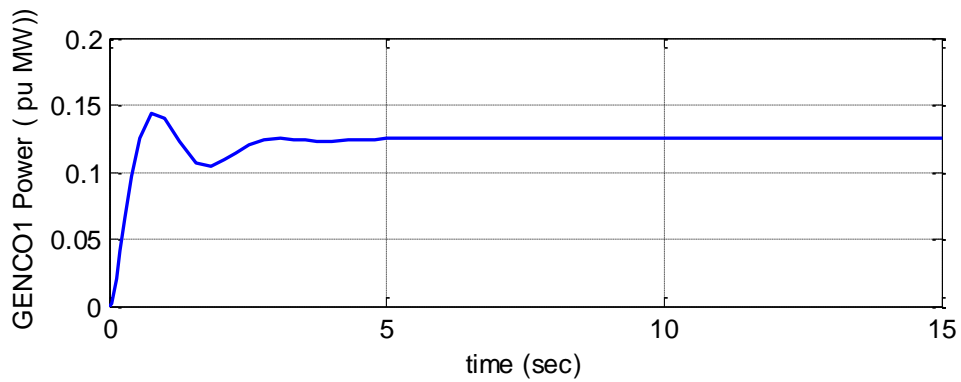


Fig.4c: Generated Power by GENCO1 & GENCO2 (pu MW) case 1

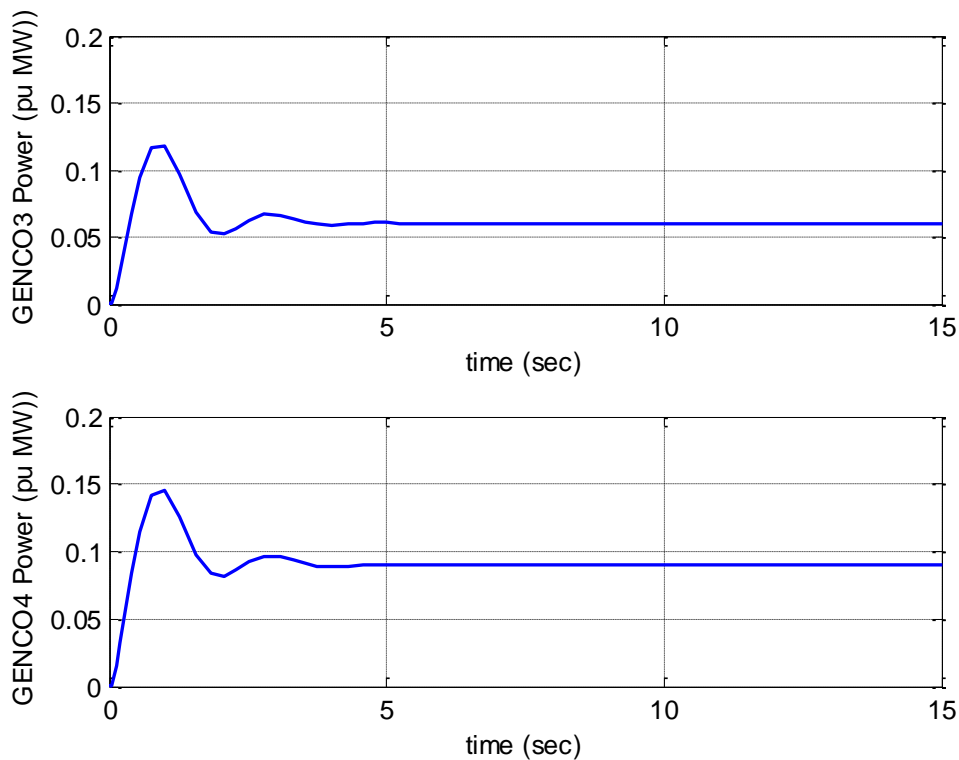


Fig.4d: Generated Power by GENCO3 & GENCO4 (pu MW), case 1

B. Case 2: Contract Violation

It may be happen that a DISCO violate a contract by demanding more power than that specified in the contract. This excess power is not contracted out to any GENCO. This uncontracted power must be supplied by the Gencos in the same area as the DISCO. It must be reflected as a local load of the area but not as the contracted demand. Now consider DPM as below

Now in this case all the Discos contract with the Gencos for power as per the following DPM-

$$DPM = \begin{bmatrix} .5 & .25 & 0 & .3 \\ .2 & .25 & 0 & 0 \\ 0 & .25 & 1 & .7 \\ .3 & .25 & 0 & 0 \end{bmatrix}$$

It is assumed that each DISCO demand s 0.1 pu MW power from GENCO as defined by *cpfs* in DPM matrix and DISCO1 demand 0.1 pu MW of excess power. ACE participation factors are *apf1*=0.75, *apf2*=1-*apf1*=0.25, *apf3*= 0.5, *apf4*=1-*apf3*=0.5.

The total local load in area I = Load of DISCO1 + Load of DISCO2
 = (0.1 + 0.1) + 0.1= 0.3 pu MW

Similarly, the total local load in area II = Load of DISCO3 + Load of DISCO4
 = (0.1 + 0.1) = 0.3 pu MW (no un contracted load)

Schedule tie line power flow is 0.05 from area 2 to area 1.

The system in figure 3 simulated again ,using the above data and the system parameters given in Appendix -I . The result of the simulation has shown in figure 5.

Fig. 5a: shows the dynamic responses of frequency deviations in two areas (i.e., Δf1 and Δf2).The frequency deviation in each area goes to zero in the steady state.

Fig. 5b: shows the tie line power deviation between two area. The actual tie line power .05 pu MW which flows from area 2 to area 1.Scheded tie tie line power is also .05, in the steady state deviation goes to zero.

Fig 5c & 5d show the power generated by GENCO1, GENCO2,GENCO3 & GENCO4 in the steady state. The generation of GENCO3 & GENCO4 are not affected by the excess load of DISCO1. The un contracted load of

DISCO1 is reflected in generation of GENCO1 & GENCO2. The ACE participation factor decide the distribution of un contracted load in the steady state. Thus this excess load is taken up by the GENCOs in the same area as that of the DISCO making the un contracted demand.

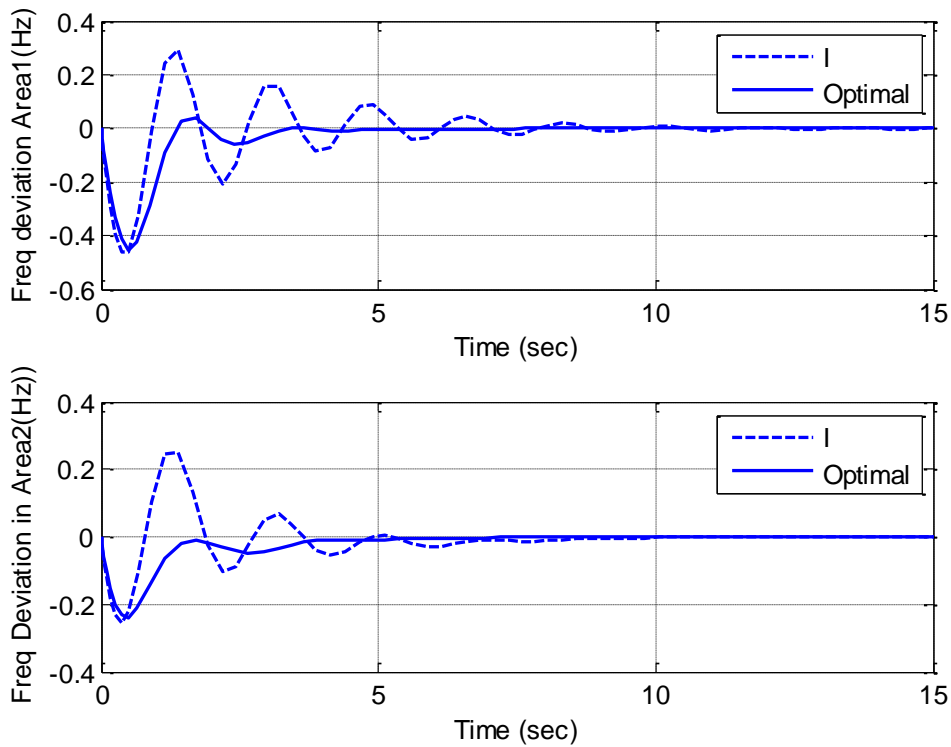


Fig. 5a: Frequency Deviations (Hz) for area 1 & area 2, case2

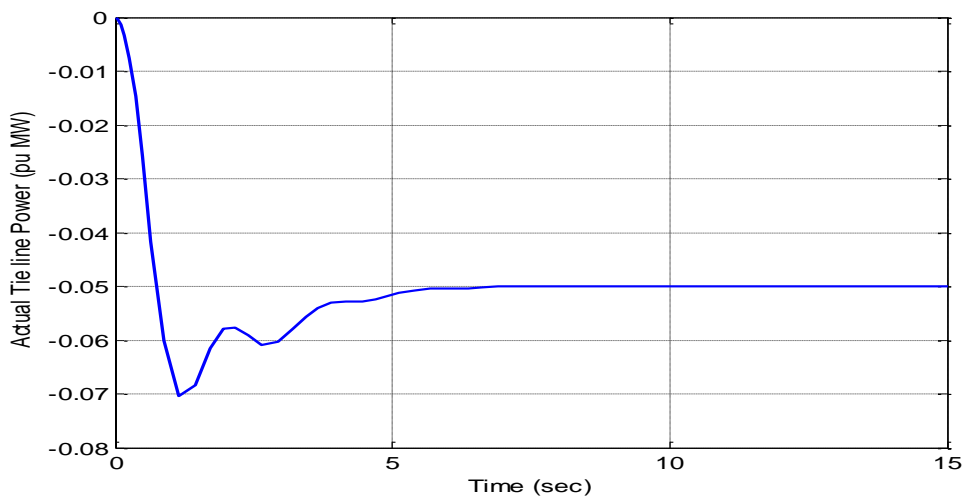


Fig.5b: Actual Tie line power (pu MW), case 2

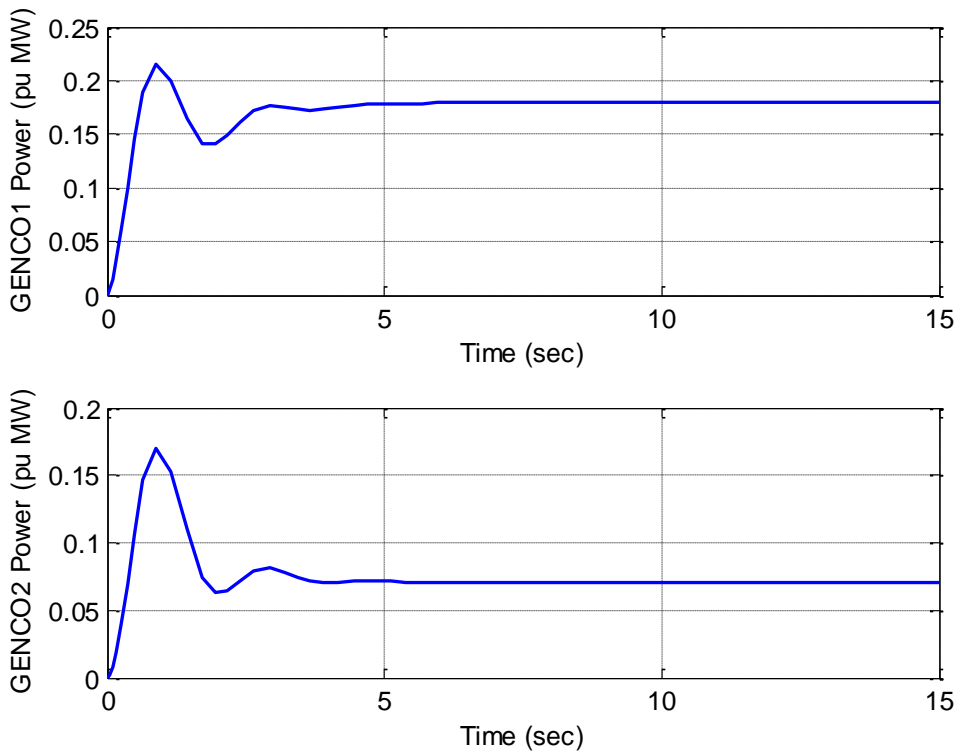


Fig.5c: Generated Power by GENCO1 & GENCO2 (pu MW), case 2

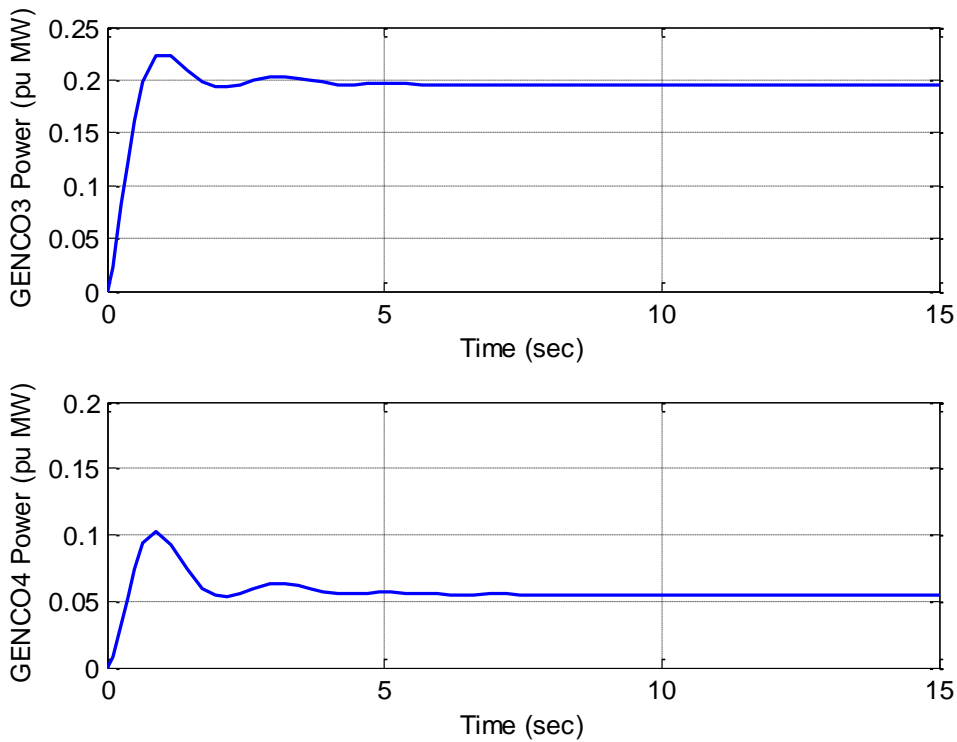


Fig.5d: Generated Power by GENCO3 & GENCO4 (pu MW), case 2

The value of 'k' optimal controller gain matrix, find out with the help of MATLAB program is given below.

$$k = \begin{bmatrix} .312 & -.080 & .571 & .571 & -.128 & -.128 & .108 & .108 & -.023 & -.023 & -1 & 0 & .147 \\ -.080 & .312 & -.128 & -.128 & .571 & .571 & .023 & -.023 & .108 & .108 & 0 & -1 & -.147 \end{bmatrix}$$

Hence the control inputs:

$$u_1 = -.312 x_1 + .08 x_2 - .571 x_3 - .571 x_4 + .128 x_5 + .128 x_6 - .108 x_7 - .108 x_8 + .023 x_9 + .023 x_{10} + x_{11} - .147 x_{13}$$

$$u_1 = .080 x_1 - .312 x_2 + .128 x_3 + .128 x_4 - .571 x_5 - .571 x_6 - .023 x_7 + .023 x_8 - .108 x_9 - .108 x_{10} + x_{11} + .147 x_{13}$$

The eigen values of 'A' open loop system are

$$[0, 0, -0.444 + 3.63i, -0.444 - 3.63i, -0.823 + 3.02i, -0.823 - 3.02i, -0.778, -13.4, -13.4, -2.50, -2.50, -12.5, -12.5]$$

Two eigen values are zero and remaining have negative real parts indicating that, the system is marginally stable before applying the optimal control strategy.

The eigen values of 'Ac' closed loop system are

$$[-13.3996 \quad -13.3804 \quad -0.8468 + 3.7432i \quad -0.8468 - 3.7432i \quad -1.1232 + 3.1450 \quad -1.1232 - 3.1450i \quad -0.8032 + 0.2435i \quad -0.8032 - 0.2435i \quad -0.4590 \quad -12.5000 \quad -12.5000 \quad -2.5000 \quad -2.5000]$$

All eigen values of 'Ac' have negative real parts indicating that the system is asymptotically stable after applying optimal control strategy.

APPENDIX I

$P_{r1} = P_{r2}$	2000 MW
$R_1 = R_2 = R_3 = R_4$	2.4 Hz /pu MW
$K_1 = K_2$.6558
$K_{p1} = K_{p2}$	120
$T_{p1} = T_{p2}$	24
$B_1 = B_2$.429
T_{12}	.0707 MW / radian
$T_{T1} = T_{T2} = T_{T3} = T_{T4}$.4
$T_{g1} = T_{g2} = T_{g3} = T_{g4}$.08
$P_{tie \max}$	200 MW

VII. CONCLUSION

This work gives an overview of AGC in deregulated environment which acquires a fundamental role to enable power exchanges and to provide better conditions for the electricity trading. The important role of AGC will continue in restructured electricity markets, but with modifications. Bilateral contracts can exist between DISCOs in one control area and GENCOs in other control areas. The use of a "DISCO Participation Matrix" facilitates the simulation of bilateral contracts. Models of interconnected power systems in deregulated environment have been developed for integral as well as optimal control strategies. The state equations and control equations have been successfully obtained and full State feedback optimal controller has designed. The models have also been tested for system stability before and after applying closed loop feedback control and it has been observed performance is much better in case of full state feedback optimal controller as compare to integral controller.

References

- [1] J. Kumar, K. Ng, and G. Sheble, "AGC simulator for price-based operation: Part I," IEEE Trans. Power Systems, vol.12,no. 2, May 1997.
- [2] J. Kumar, K. Ng, and G. Sheble, "AGC simulator for price-based operation: Part II," IEEE Trans. Power Systems, vol.12,no. 2, May 1997.
- [3] O. I. Elgerd and C. Fosha, "Optimum megawatt-frequency control of multiarea electric energy systems," IEEE Trans. Power Apparatus & Systems, vol. PAS-89, no. 4, pp. 556-563, Apr. 1970.
- [4] C. Fosha and O. I. Elgerd, "The megawatt-frequency control problem: A new approach via optimal control theory," IEEE Trans. Power Apparatus & Systems, vol. PAS-89, no. 4, pp. 563-577, Apr. 1970.
- [5] R. Christie and A. Bose, "Load-frequency control issues in power systems operations after deregulation," IEEE Trans. Power Systems, vol. 11, pp. 1191-1200, Aug. 1996.
- [6] E. Nobile, A. Bose, and K. Tomsovic, "Bilateral market for load following ancillary services," in Proc. PES Summer Power Meeting, Seattle, WA, July 15-21, 2000.
- [7] V. Donde, M. A. Pai, I. A. Hiskens, "Simulation of Bilateral Contracts in an AGC System After Restructuring" IEEE Trans. Power Systems, vol. 16, no. 3, August 2001.
- [8] M. Ilic, F. Galiana, and L. Fink, Eds., Power Systems Restructuring: Engineering & Economics. Boston: Kluwer Academic Publishers, 1998.
- [9] G. B. Sheble, Computational Auction Mechanisms for Restructured Power Industry Operation. Boston: Kluwer Academic Publishers, 1999.
- [10] P. Kundur, "Power System Stability and Control," McGraw-Hill, 1994
- [11] I. J. Nagrath, D. P. Kothari, "Power System Engineering," TATA McGraw Hill, 1994.
- [12] Hadi Saadat, "Power System Analysis "TATA McGraw Hill 1991

Synthesis and characterization of resin copolymer derived from cardanol-furfural/ formaldehyde –p-hydroxy benzoic acid.

A. Panda, J.Ch. Pal, Dr.P.K. Mishra, Dr. S.K. Swain*, Dr.B.Pr. Sahu*

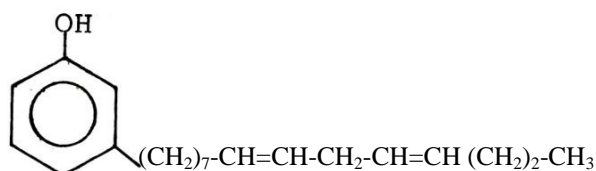
Research Laboratory of Chemistry Department, R.C.M. Sc. College, Khallikote (761030), Ganjam, Odisha, India.

ABSTRACT:

Some of resin copolymers have been synthesized by refluxing cardanol, which is a major constituent of Cashew nut Shell Liquid (CNSL), with furfural/formaldehyde and p-hydroxy benzoic acid in presence of different acid and base catalysts. The resins have been characterized by FTIR spectra. The thermal behaviors of the resins have been studied and the kinetic parameters as well as plausible degradation mechanism have been suggested. In addition to this XRD and SEM of the copolymers have been studied.

I. INTRODUCTION

Cashew nut shell liquid (1-5) (CNSL) and its polymeric product find a wide variety of applications in industries (8-10). The main constituents of CNSL are anacardic acid, cardol, cardanol and 6-methyl cardol. On heating, anacardic acid is decarboxylated to cardanol which is a n-penta decadienyl phenol. Its aliphatic side chain usually consists of mixture of one, two and three double bonds in a linear chain. These components of CNSL have been characterized by a number of techniques including proton NMR, ultraviolet (UV), infrared (IR) and chromatography.



Although a tot of work has been carried out on phenol-formaldehyde polymers which have great deal of importance as materials, the area of synthetic resins derived from renewable resources like CNSL has not been widely exploited. Recently Misra and Pandey (11) reported the kinetics of formaldehyde condensation of cardanol. Manjula has studied the oligomerization of cardanol using acid catalyst.(12,13) Recently Varma and coworkers(14), on the basis of the fragmentation pattern of mass spectra and NMR spectra proposed the structure of cardanol. O' Connor and Blum (15) have reported the thermal stability of some resins by condensing cardanol formaldehyde. Pillai et al (16, 17) have reported the GPC studies on the cationic polymerization of cardanol initiated by Boron trifluoride diethyl etherate. Sathiyalekshmi (18) reported the, structure and properties of CNSL-novalac resins prepared using succinic acid as the catalyst. Nayak and Lenka (19-30) have reported the synthesis and characterization of a large number of resins using a multitude of hydroxy aromatic compounds, formaldehyde/furfural in the presence of acid and base as the catalysts. They have reported, thermal, ion-exchange properties, bacteriocidal and fungicidal properties of the resins. This communication presents the synthesis and characterization of resins obtained by condensation of cardanol-formaldehyde-p-hydroxy benzoic acid.

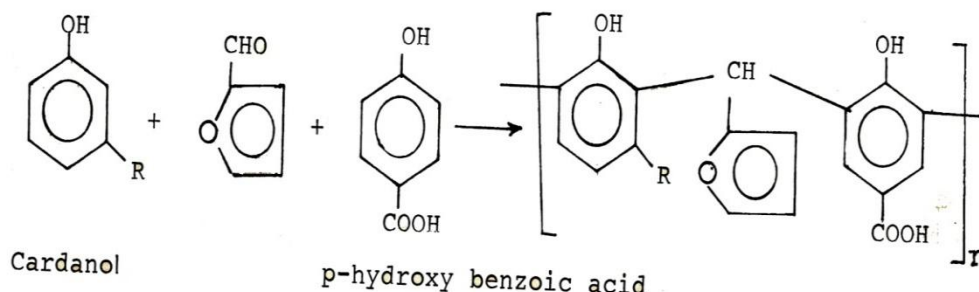
Synthesis of resins:

Method-1

A mixture of cardanol (4 m. mole), furfural (40 m. mole) , and p-hydroxy benzoic acid (4 m. mole) was refluxed at 110°C for about 6-8 hours in presence of 2 ml of NaOH (4N) with periodical shaking. At the end of the reaction, the contents were extracted with ice-cold water, filtered and washed repeatedly with hot water to remove the unreacted materials. The product was dried in vacuum. The physico-chemical properties of the

resins are furnished in Table-2. The dried resin was weighed and mixed with different percentage of hexamethylenetetramine (HMTA) which acts as curing agent and powdered and kept in the oven for first one hr. at 100^o C and post cured further 1 hr. at 120^o C.

The poly condensation reaction of cardanol with furfural (40 m. mole), and p-hydroxy benzoic acid may be represented as follows.



Method-2

Reagents taken

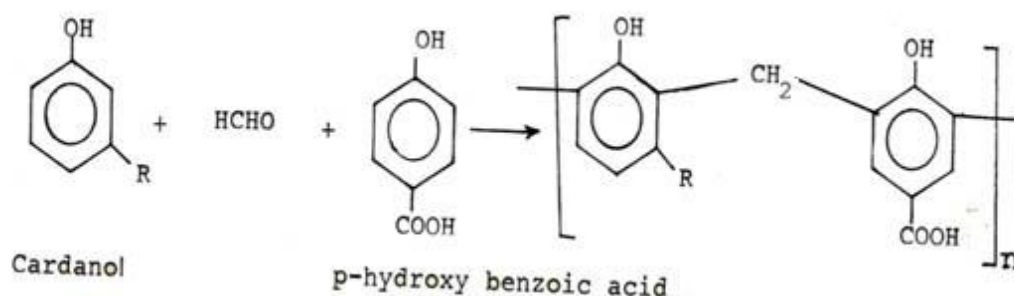
- i) Cardanol - 1.192 gm
- ii) Formaldehyde - 3.84 gm
- iii) p-hydroxy benzoic acid - 0.552 gm.

Catalyst used: - HCl (4N) 2 ml

Condensation of cardanol- formaldehyde and p-hydroxy benzoic acid in presence of acid catalyst.

Procedure : A mixture of 1.192 gm (4 m. mole) of cardanol, 3.84 gm (40 m. mole) of formaldehyde and 0.552 gm (4 m. mole) of p-hydroxy benzoic acid were refluxed for 2-3 hrs at 80-100^oC in presence of 2 ml of (4N) HCl catalyst with periodical shaking. After completion of reaction, the product was washed with 10% NaOH then hot water in order to remove the basic and unreacted impurities, filtered and the residue was dried in vacuum at 60^oC, and then collected.

Polycondensation reaction for above method may be represented as follows:



PHYSICO- CHEMICAL PROPERTIES OF CARDANOL-FURFURAL-P-HYDROXY BENZOIC ACID.

Table-1

Sl. No.	Name of comonomer	Catalyst	Duration of heating	Colour	Structure	Solubility	Yield (%)	Decomposition of temp. ($^{\circ}$ C)
01	Cardanol+formaldehyde+p-hydroxy benzoic acid	HCl	3	Brown	Crystalline	DMF*	70	>360
02	Cardanol+formaldehyde+p-hydroxy benzoic acid	H ₂ SO ₄	3	Reddish	Crystalline	DMF*	60	>360
03	Cardanol+formaldehyde+p-hydroxy benzoic acid	NaOH	6	Brown	Crystalline	DMSO*	65	>360
04	Cardanol+formaldehyde+p-hydroxy benzoic acid	KOH	6	Brown	Crystalline	DMSO*	60	>360
05	Cardanol+formaldehyde+p-hydroxy benzoic acid	H ₃ PO ₄	2	Brown	Crystalline	DMSO*	70	>360
06	Cardanol-furfural-p-hydroxy benzoic acid	HCl	2	Brown	Crystalline	DMSO*	65	>360
07	Cardanol-furfural-p-hydroxy benzoic acid	H ₂ SO ₄	2	Reddish	Crystalline	DMSO*	60	>360
08	Cardanol-furfural-p-hydroxy benzoic acid	KOH	6	Brown	Crystalline	DMSO*	70	>360

* - represents partially solvents.

II. FTIR ANALYSIS

The structure of the cardanol-furfural-p-hydroxy benzoic acid was identified from the spectral data from the fig.1. The band near 3369.9 cm^{-1} is due to O-H stretching in phenolic OH group. The strong peak at 2833.6 cm^{-1} indicates the C-H stretching of methylene linkages. A medium absorption band at 1667.1 cm^{-1} is due to C=O stretching in -COOH. The peak at 1585.2 cm^{-1} is due to carboxylate anionic stretching vibration. The alkene disubstitution is identified by the peak at 1514.9 cm^{-1} . The peak at 1414.2 is due to C-H asymmetric stretching. The band at 1158.9 cm^{-1} is due to C-O stretching of ester or alcohol. The peak at 1098 cm^{-1} is due to C-O stretching. The intense peak at 842.7 cm^{-1} is due to CH=CH trans unsaturation. The peak 760.7 cm^{-1} is due to monosubstituted aromatic ring typically have out of plane bending.

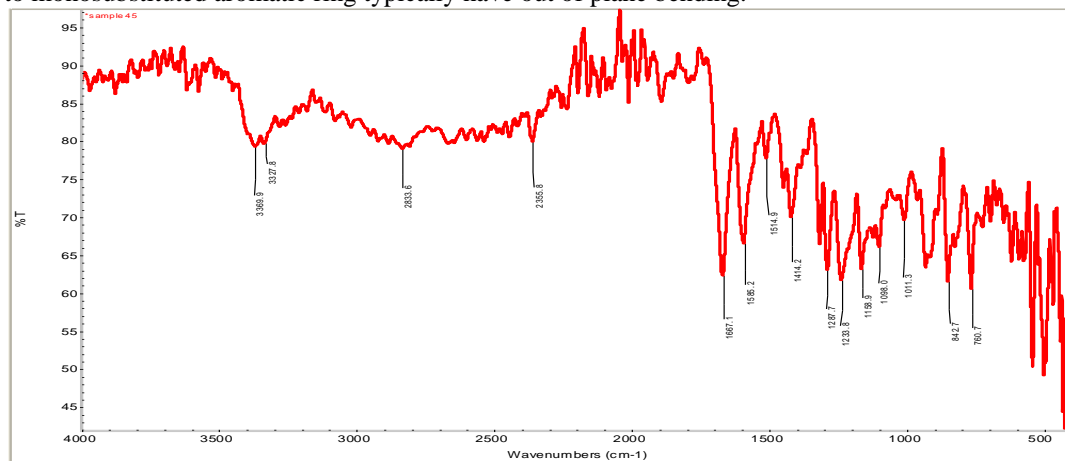


Fig-1. IR Spectra of the resin prepared from cardanol-furfural-p-hydroxy benzoic acid.

Table 2

Sl. No.	Wave No. (Cm ⁻¹)	Functional group
01	3369.9	O-H stretching in cardanol part
02	2833.6	C-H stretching(SP ³ carbon)
03	1667.1	-C-O stretching in -COOH group
04	1585.2	C=C stretching in aromatic ring and N-H bending
05	1514.9	C=C ring stretching
06	1414.2	C-H asymmetric stretching
07	1158.9	C-O stretching of ester or alcohol
08	1098.0	C-O stretching
09	842.7	Out of plane /CH=CH trans unsaturation
10	760.7	Monosubstituted aromatic ring typically have out - of - plane bending

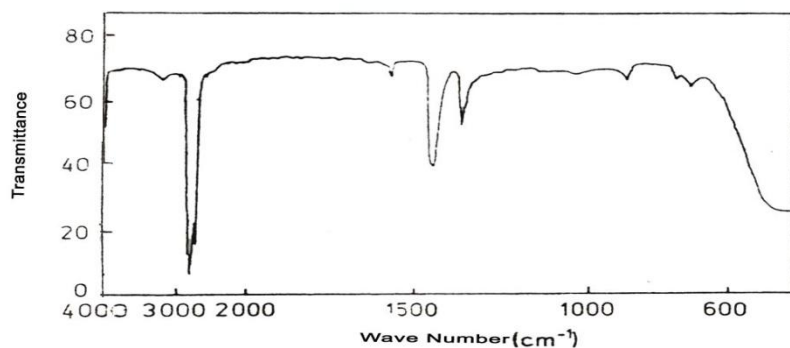


Fig-2 IR spectra of the resin prepared from cardanol- formaldehyde -p-hydroxy benzoic acid.

Table 3

Sl. No.	Wave No. (Cm ⁻¹)	Functional group
01	3400	O-H stretching in phenolic OH group
02	3040-3010	-C=C- stretching in alkene
03	2920-2860	C-H stretching in methylene linkage
04	1598	Carboxylate anionic stretching vibration
05	1460-1440	C-H bending in side chain alkane
06	1385-1380	The phenolic O-H bending and C-O stretching
07	780-680	Bending vibration of C-H group

Thermogravimetric (TG) Analysis of the resins.

On the basis of the above observed trend in weight loss with temperature. a plausible degradation mechanism of the resin copolymers prepared by condensing cardanol-furfural-p-hydroxy benzoic acid may be due to

- (1) chain fragmentation and post curing controlled by the unreacted methylol groups;
- (2) thermal reforming ,controlled by the free radicals formed, and
- (3) ring stripping, depending upon the elemental composition .

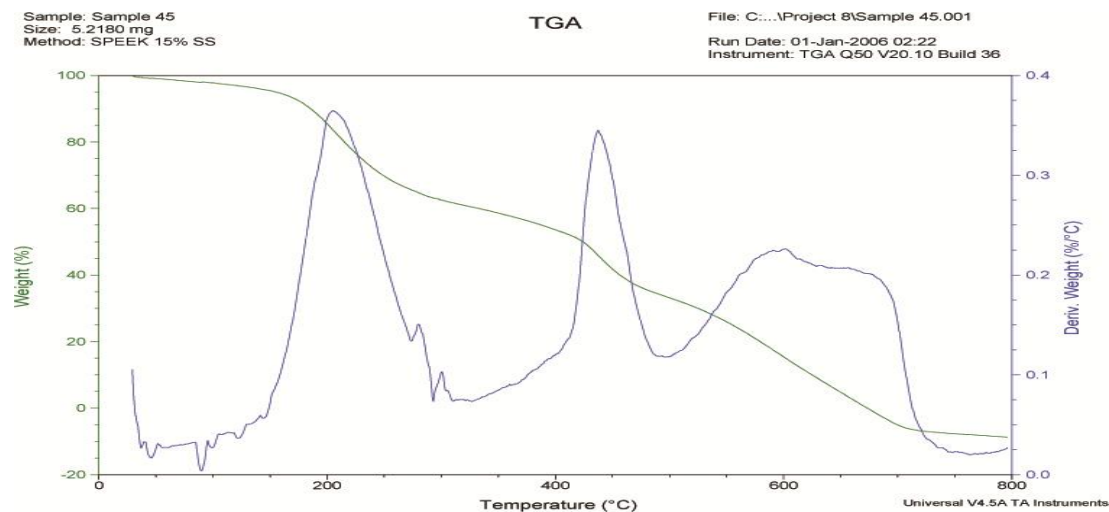


Fig-3 Thermogram of copolymer (cardanol-furfural-p-hydroxy benzoic acid).

Percentage of weight loss of resin for every 50 degree interval

Table-4

Sl. No.	Temperature Celsius in degree	% of weight loss
01	50	1
02	100	3
03	150	5
04	200	15
05	250	30
06	300	38
07	350	41
08	400	45
09	450	55
10	500	65
11	550	71
12	600	82

III. Result & Discussion:

From the TG curve of resin copolymer prepared from cardanol-furfural and p-hydroxy benzoic acid in presence of NaOH catalyst, it was observed that about 50-55% of weight loss occurs up to 400°C. 70-75% Of weight loss occurs up to 600°C. Copolymer prepared in presence of acid catalyst like H₂SO₄ or H₃PO₄ is more thermally stable than Copolymer prepared in presence of base catalyst like NaOH or KOH it may be due to greater degree of crosslinking and greater dehydration reaction.

IV. X-RAY DIFRACTION:

There are three major aspects of investigating the crystal structure of resin copolymers prepared from cardanol-formaldehyde/furfural- substituted aromatic acids/alcohols. These are (i) degree of crystallinity, (ii) lattice size, (iii) ctystallite orientation. Hermans (20) and Karst and Flaschner (21) developed quantitative methods for determination of the degree of crystallinity(Xcr) i.e. relative proportion of crystalline domains in the crystalline - amorphous composite structure. These two methods define crystalline domains as those which contribute maxima in its X-ray diffraction curve and arrived at a crystalline proportion by comparison of the intensity of maxima considered to be contributed by the crystalline part of the substance and the intensity of the background scattering supposed to be due to amorphous regions. Ruland (22) developed a better method for the determination of Xcr by introducing crystal defect concept which was subsequently simplified and computed by Vonk(234) Hindlesh(24)developed a peak resolution technique to find out Xcr values . Crystalline size can be determined by Scherrers' Formula (25).

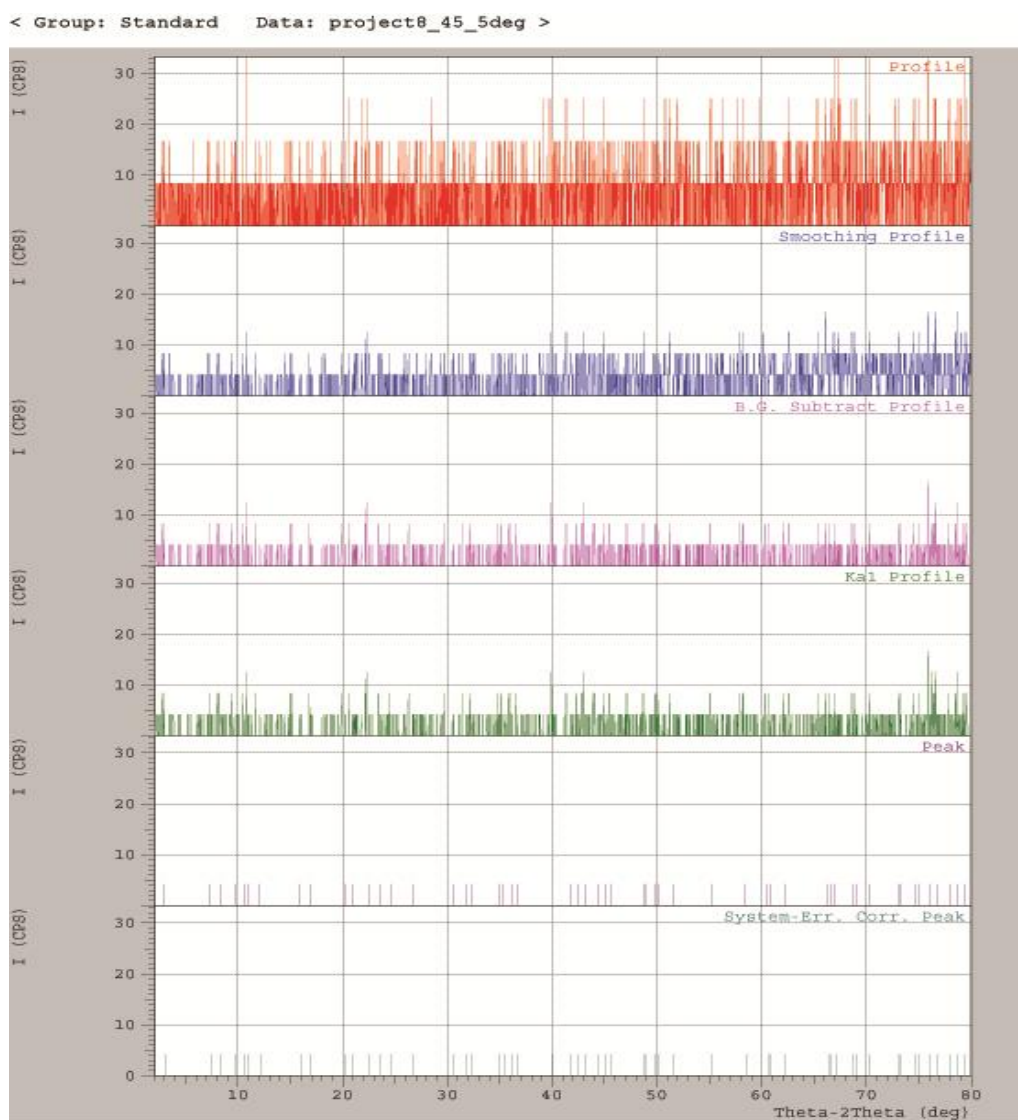


Fig.4

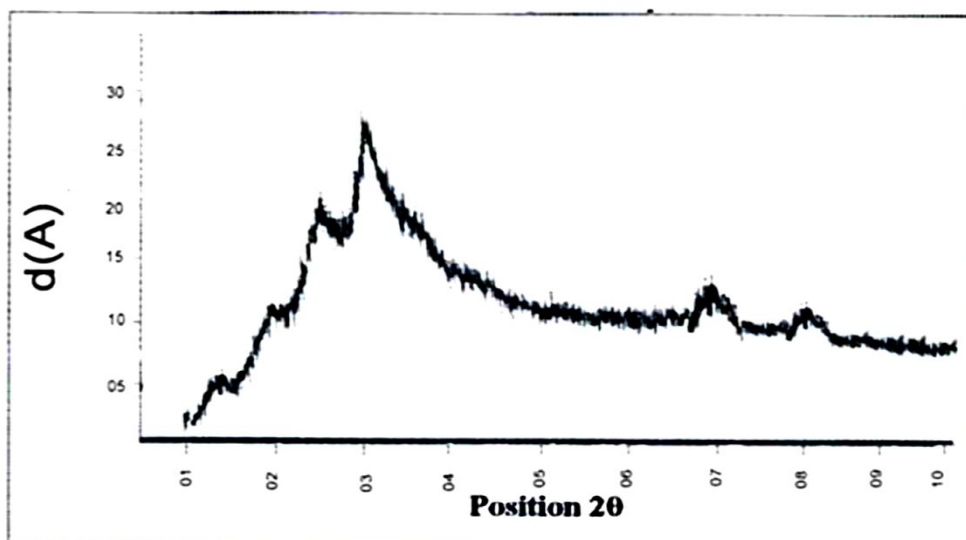


Fig-5: XRD Pattern of Cardanol- Furfural-P-hydroxybenzoic acid

The basic data of cardanol-furfural-p-hydroxy benzoic acid I

Table-5

Sl. no.	Strong-est peak no.	2 theta(deg)	d(A)	I/II	FWHM (deg)	Intensity (Counts)	Integrat-ed Intensity(Counts)
1	1	3.1121	28.36693	100	0.00000	1	0
2	2	7.3851	11.96071	100	0.00000	1	0
3	3	8.3187	10.62034	100	0.00000	1	0

V. Result and discussion.

In the present investigation, Ruland and Vonk method has been employed for calculating the degree of Crystallinity (X_{cr}) values but Bragg's equation and Debye Scherer equation indicated the presence of two sets of reflection planes corresponding to the 2θ values of 2° and 80°. This is more clearly observed from the data given in table-5 and also in fig.4&5.

A polymer can be considered partly crystalline and partly amorphous too much crystallinity of substance causes brittleness. The crystallinity part gives sharp narrow diffraction peak and the amorphous part gives very broad peak. The relation between the intensities can be used to calculate the degree of crystallinity.

VI. SCANNING ELECTRON MICROSCOPE (SEM) :

A Scanning Electron Microscope (SEM) is type of a electron microscope that produces images of a sample by scanning it with a focused beam of electrons. The electrons interact with atoms in the sample, producing various signals that can be detected and that contain information about the sample surface topography and composition. The electron beam is generally scanned in a raster scan pattern, and the beam's position is combined with the detected signal to produce an image. SEM can achieve resolution better than nanometer. Specimens can be observed in high vacuum, in low vacuum, in wet conditions and at a wide range of elevated temperature. In most applications, data are collected over a selected area of the surface of the sample and a 2-dimensional image is generated that displays spatial variations in these properties. Areas ranging from approximately 1 cm to 5 microns in width can be imaged in a scanning mode using conventional SEM techniques (magnification ranging from 20X to approximately 30,000X, spatial resolution of 50 to 100 nm).

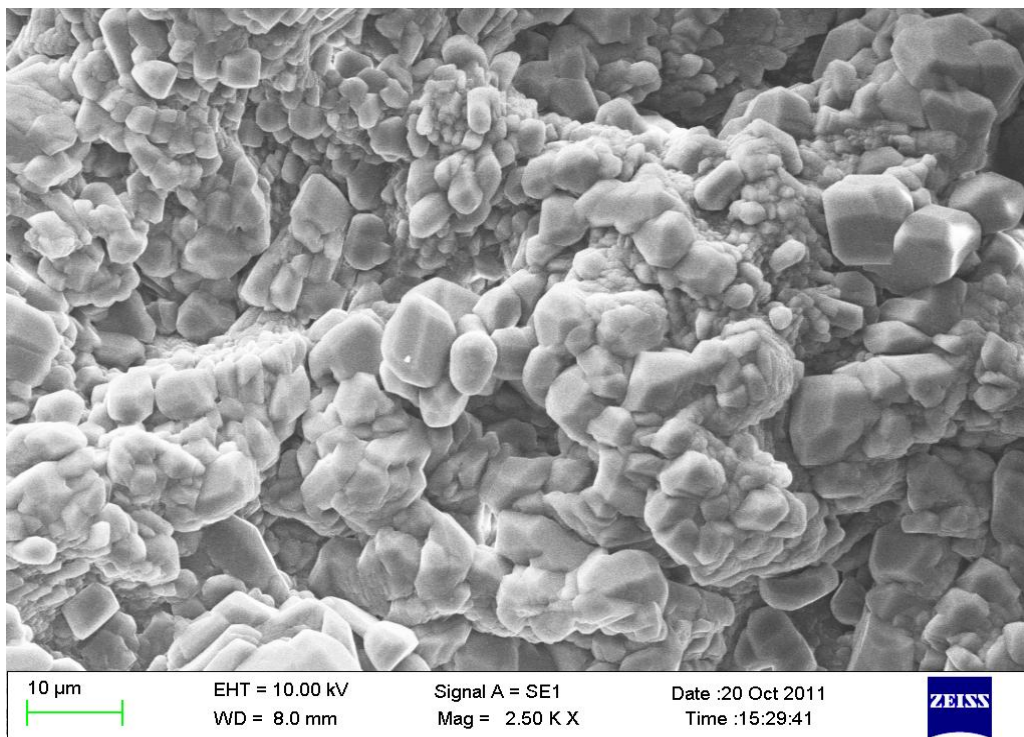


Fig. 6 Cardanol-furfural-p-hydroxy benzoic acid

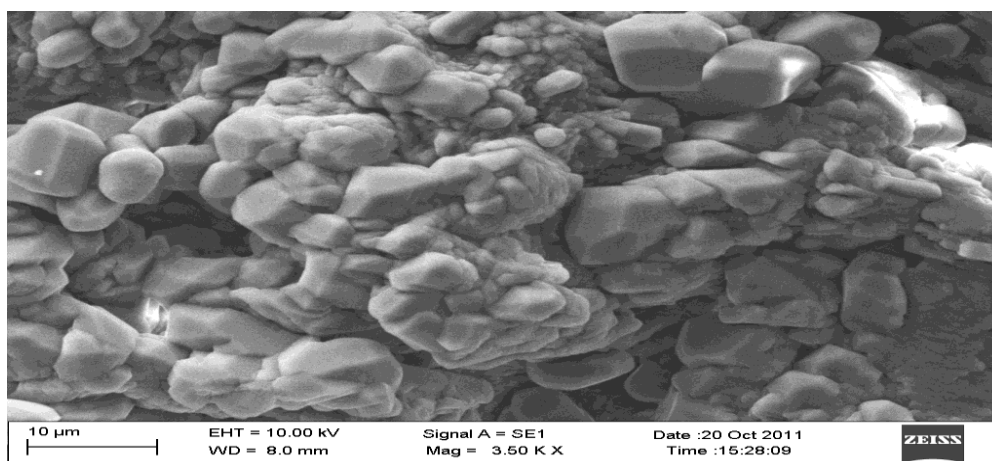


Fig.7 Cardanol-furfural-p-hydroxy benzoic acid.

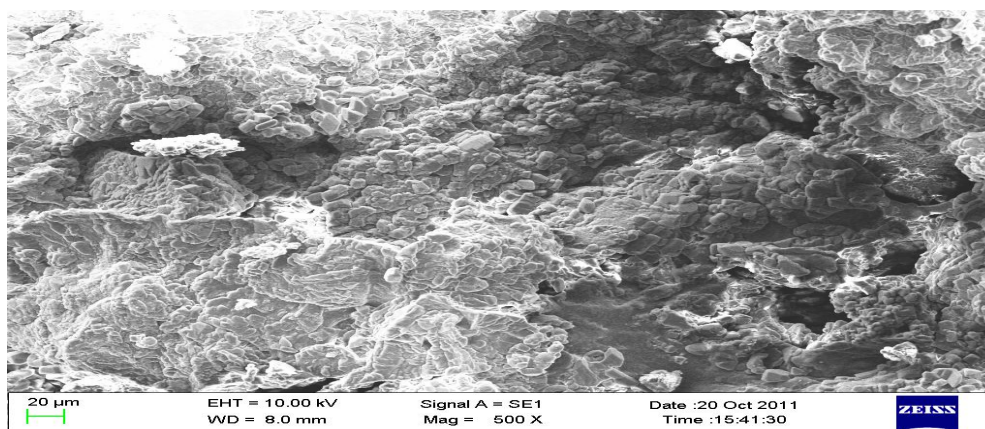


Fig.8 Cardanol-furfural-p-hydroxy benzoic acid.

VII. Result and Discussion:

The SEM is routinely used to generate high-resolution images of shapes of resin copolymer and to show spatial variations in chemical compositions: 1) acquiring elemental maps or spot chemical analysis using EDS, 2) discrimination of phases based on mean atomic number (commonly related to relative density) using BSE and 3) compositional maps based on differences in trace element “activators” (typically transition metal and Rare Earth elements) using CL. The SEM is also widely used to identify phases based on qualitative chemical analysis and/or crystalline structure of resin copolymer caradnol – furfural–p-hydroxy benzoic acid. It has been studied from ZEISS instrument from CIPET (LARPM) in fig. (6-8).

REFERENCES

- [1]. K.Varma,S.K.Dha,M.Varma and T.S. Biddapa, *Angew Makromol.Chem.*154,67(1987).
- [2]. J.H.P. Tyman and J.J. Morris, *J.Chromatog* 27, 287, (1967),.
- [3]. J.H.P. Tyman and N. Jacobs, *J. Chromatog.* 54,3,(1971).
- [4]. J.H.P. Tyman, *Chem.commun.*982 (1967).
- [5]. J.H. Tyman, V. Tychopoulos and B.A. Colenutt, *J.Chromätog*, 231,287 (1981).
- [6]. A.A. Durrani, G.C. Sun and J.H.P. Tyman, *Lipids*, 17,561(1982).
- [7]. A.A. Durrani,L. Davis, S.K. Sood, V. Tychopoulos, and J.H.P. Tyman, *J. Chem Tech. Biotechnol*,32,681(1982).
- [8]. J.Caplin and J.H.P. Tyman, *J. Chem. Res. Synop.* 14, (1982).
- [9]. S.K.Sood,J.H.P. Tyrnan, A.A.Durrani and R.A.Johnson,*Lipids*, 21, 241(1986).
- [10]. B.G.K. Murthy, M.A. Sivasamban and J.S. Aggarwal,*J. Chromatog.* 32, 519 (1968).
- [11]. A.K.Misra and G.N.Pandey, *J. Appl. Polym. Sc.* 30, 969 (1985).
- [12]. S.Manjuia, J.D\$udha, S.C.Bera and C.K.S.Pillai, *J. Appl.Polym. Sc.* 30 (1985) 1767.
- [13]. S.Manjula, and C.K.S.Pillai, *Polymer News*, 12 (1987) 369.
- [14]. I.K.Varma, S.K.Dhara, M.Varma and T.S.Biddapa, *Angew. Makromol. Chèm.* 154 (1987) 67.
- [15]. D.O' Connor, F.D.Blum, *J. Appl. Polym. Sc.* 33 (1987) 1933.
- [16]. C.K.S.Pillai, P.K.Rohatgi and Gopakumar, *J. Sc. Ind. . Res.* 40 (1981) 159.
- [17]. S.Manjula and C.K.S. Pillai, *Polymer News*, 12 (1987) 369
- [18]. K.Sathiyalekshmi, *Bull. Mater Sc.* 16 (1993) 137.
- [19]. S.Lenka, A.P.Das and P.L.Nayak, *J. Polym. Sc. Polym. Chem. Ed.* 30, (1985) 4619
- [20]. Hermans PH (1948) *J. Appl. Phys.* 19:491.
- [21]. Karst W, Flachner L. (1948) *Kolloid Z.* 6:111.
- [22]. Ruland W. (1964) *Polymer* 5:89.
- [23]. Vonk CG (1973) *J. Appl. Cryst.* 148: 6.
- [24]. Hindlesh AM (1980) *Tex. Res. J.* 50(10): 581.

A Hybrid Virtual Reality Simulation System for Wave Energy Conversion

Trongnghia Huynh¹, Gene Hou¹, Jin Wang^{2, 4}, May Hou³, and Miltiadis Kotinis¹

¹ Department of Mechanical and Aerospace Engineering Old Dominion University, Norfolk, VA 23529

² Department of Mathematics Old Dominion University, Norfolk, VA 23529

³ Department of Computer Science Norfolk State University, Norfolk, VA 23504

⁴ Department of Mathematics University of Tennessee, Chattanooga, TN 37403

Abstract:

Recent advances in interfacing computational software with experimental hardware have expanded the area of application of virtual reality (VR) beyond that of visualization to simulation-based training and education. The VR can now be directly interfaced with hardware and physics-based computational models to form a sophisticated hybrid simulation system. The integrated simulation system developed in this research demonstrates the motion of a heaving buoy in irregular waves in order to demonstrate the process of wave energy conversion. The VR system consists of three main function blocks: A physics-based simulator in MATLAB®, a game studio in Unity 3D, and a hardware manipulator in LabVIEW®. These three blocks operate in a decentralized mode and communicate with each other as interconnected nodes of an integrated network. This article details the development of each of these function blocks and addresses issues associated with data transmission and lockstep synchronization. The effectiveness of the developed hybrid VR system is demonstrated to conclude the presentation.

Keywords: Unity 3D, virtual reality, wave energy conversion, wave simulation.

I. INTRODUCTION

This research follows the Mikropoulos and Natsis [1] notion of virtual reality (VR), who define it as “a mosaic of technologies that support the creation of synthetic, highly interactive three-dimensional spatial environments that represent real or non-real situations.” The dominant technology in VR is visual representation, namely virtual environment (VE). VE and VR are quite often interchangeable in the literature. VE along with technologies such as immersion, multisensory interaction and haptic devices has enabled VR to offer a first-order experience in emulating the natural environment and visualizing abstract ideas. As a result, VR has been proven to be effective in increasing knowledge construction and, thus, enhancing the learning outcome.

Many educational institutions have recently incorporated VR in classroom teaching; particularly in the engineering and science disciplines such as factory production process [2-3], chemistry [4], electrical [5] and mechanical engineering laboratories [6]. Recent advances in software-hardware interfacing have increased the level of the VE sophistication and broadened the range of applications of VR to allow the VE to interact with physical models in real time. For instance, Hu and Zeigler [7] developed an interface tread to allow for direct interaction between a robot and the VE. Richardson, et al [8] incorporated the machine code in the virtual environment to simulate the microcontrollers interactively. Morris et al [9] developed a physics-based simulation to model sound and force dynamics in a virtual environment to train physicians for temporal bone surgery. Fu et al [10] introduced risk models in the virtual environment for safe navigation training in the three gorges reservoir area. In addition to those project- or course-oriented VEs, many educators and IT experts have proposed proper frameworks and simulation tools to develop a distributed VE shared by multiple schools [11-13].

In order to investigate the effectiveness of using VR as an educational tool, Mikropoulos and Natsis recently reviewed 53 research articles on educational virtual environments and summarized their findings in [1] in terms of educational context, characteristics and features of each VR, and the associated learning theory. Abulrub et al [14] stressed creative learning in an interactive and immersive virtual environment in which the students can create and investigate design alternatives. Finally, Lindgren [15] used an expert’s view in a virtual factory for safety training to prove that changing a person’s perspective in a virtual environment benefits learning.

The goal of this research is to develop a hardware in-the-loop VR simulation system that can be used to demonstrate the ocean wave energy harnessing process and the associated technologies. Ocean waves offer an attractive green and renewable energy source and have generated considerable interest in research, development and test in recent years. For the purpose of this research, the wave energy harnessing is performed by a heaving buoy, which is connected to a power take-off device and a generator in order to convert the wave energy first into mechanical energy and finally into electricity. The integrated hybrid VR system developed to demonstrate the wave energy conversion (WEC) process comprises three major components: A physics-based ocean wave simulation and wave-buoy interaction software, a hardware mechanism to convert the heaving buoy motion into electricity, and a virtual environment to display the interaction between the buoy and the waves. The WEC simulator sends the buoy motion signal simultaneously to both the hardware stand and the VR so that the buoy moves in synchrony in real and virtual environments. The challenge faced in this task corresponds to achieving a lock-stepped synchronization among the involved three platforms: physics-based simulation, virtual reality, and hardware mechanism.

Drafted in the early 2000s, Unity 3D has been used since as a cross-platform to create many new 3D games and applications for mobile devices, desktop PCs, and the web. It is also suitable for creating menu interfaces using built-in animation and coding scripts. In this project, Unity 3D is utilized to create the VE based on the data provided by the physics-based simulator. In Unity 3D, a game scene is constructed to demonstrate the working principle of the WEC process, i.e., absorb the wave energy through the heaving motion of the buoy and convert it into mechanical energy. C# scripts are used primarily to control every action in this game scene from the sunlight reflection on the surface of the ocean and the propagation of the waves to the motion of the floating buoy. At the beginning of each simulation, all the scripts used in the game scene are compiled and later utilized to regulate the game object according to the data input from the physics-based simulator.

The paper is organized as follows: Section 2 presents the wave spectrum model used in the Unity 3D to generate ocean waves in Unity 3D. The same wave spectrum is utilized to excite the floating buoy in the physics-based simulator. The equation of motion of the heaving buoy that results from the wave-buoy interaction and the equation of the corresponding energy absorption are derived in Section 3. The data flow among the VR system and the WEC hardware mechanism is described in Section 4. A few examples are given in Section 5 to demonstrate the simulation of the wave energy conversion process using the hybrid VR system. Conclusions and directions for improvement of the presented system are presented in Section 6.

II. MODELLING OF OCEAN WAVES

Considering the stochastic nature of ocean waves, the ocean free surface elevation can be described as a random process; for design purposes it is often assumed that it is an ergodic random process, i.e., its statistical properties will not change with time and these properties can be deduced from a single, sufficiently long sample of the process. Therefore, it can be modeled by a wave spectrum (polychromatic waves), which distributes the wave energy over wave frequency and direction. The spectral density can be computed by utilizing existing parametric wave spectra, e.g., the JONSWAP (Joint North Sea Wave Project) spectrum [16], which is capable of modeling both developing and fully-developed open-sea conditions. In this work, the unified directional spectrum, proposed in [17], is utilized in order to model the ocean waves. The spectrum is modeled considering the contribution of both short and long wind-driven waves,

$$S_k(k) = k^{-3}(B_l + B_h) \quad (1)$$

where S_k is the wavenumber spectrum, k is the wavenumber, B_l is the spectrum curvature for low frequencies, and B_h is the spectrum curvature for high frequencies. The wavenumber is defined as a function of the wave length λ : $k = 2\pi / \lambda$. Assuming operation in deep water, the relation between wavenumber and wave frequency (dispersion relation) is defined as:

$$\omega^2 = k \cdot g \quad (2)$$

with g being the acceleration of gravity ($g = 9.81 \text{ m/s}^2$). The spectrum curvature for low frequencies is calculated using the following equation:

$$B_l = \frac{1}{2} a_p \frac{c_p}{c} F_p \quad (3)$$

where c is the wave phase speed ($c = \omega/k$), c_p is the wave phase speed at the spectral peak frequency, a_p is the generalized Phillips-Kitaigorodskii equilibrium range parameter for long waves, and F_p is the long-wave side effect function. The parameter a_p is computed using the following expression [18]:

$$a_p = 0.006 \cdot \Omega^{0.55} \quad (4)$$

where Ω is the inverse wave age defined as $\Omega = U_{10}/c_p$. U_{10} is the wind speed at a height of 10 m from the water surface. The following relationship is proposed in [17] between the fetch x , i.e., the distance over which the wind blows with almost constant velocity, Ω , and U_{10} ,

$$\Omega = 0.84 \cdot \left(\tanh \left(\left(\frac{g \cdot x}{U_{10}^2 \cdot X_0} \right)^{0.4} \right) \right)^{-0.75} \quad (5)$$

with $X_0 = 2.2 \cdot 10^4$. In this research, we assume that the WEC system is operating in fully-developed seas, thus, with a typical fetch value of 150 km and U_{10} that can vary between 2 and 10 m/s, the corresponding values of Ω are in the range [0.84, 1.11]. The long-wave side effect function is calculated as:

$$F_p = L_{PM} \cdot J_p \cdot \exp \left\{ -\frac{\Omega}{\sqrt{10}} \left[\sqrt{\frac{k}{k_p}} - 1 \right] \right\} \quad (6)$$

where k_p is the wavenumber at the spectral peak frequency, L_{PM} is the Pierson-Moskowitz shape spectrum [19], and J_p is the JONSWAP peak enhancement factor [16] given by the following equations:

$$L_{PM} = \exp \left\{ -\frac{5}{4} \cdot \left(\frac{k_p}{k} \right)^2 \right\} \quad (7)$$

$$J_p = \gamma^\Gamma, \quad \gamma = 1.7 \text{ for } 0.84 < \Omega < 1 \text{ and } \gamma = 1.7 + 6 \cdot \log(\Omega) \text{ for } 1 < \Omega < 5$$

$$\Gamma = \exp \left\{ -\frac{\left(\sqrt{\frac{k_p}{k}} - 1 \right)^2}{2\sigma^2} \right\}, \quad \sigma = 0.08 \cdot (1 + 4\Omega^{-3}) \quad (8)$$

The spectrum curvature for high frequencies is calculated as:

$$B_n = \frac{1}{2} a_m \frac{c_m}{c} F_m \quad (9)$$

where a_m is the generalized Phillips-Kitaigorodskii equilibrium range parameter for short waves, c_m is the minimum phase speed at the wavenumber k_m associated with the gravity-capillary peak in the curvature spectrum, and F_m is the short-wave side effect function. Assuming that $k_m = 370$ rad/m [17], then $c_m = 0.23$ m/s. The short-wave side effect function is calculated as:

$$F_m = \exp \left\{ -\frac{1}{4} \cdot \left(\frac{k}{k_m} - 1 \right)^2 \right\} \quad (10)$$

The equilibrium range parameter is calculated assuming a linear relation between a_m and the friction velocity u^* at the water surface:

$$a_m = a_0 \frac{u^*}{c_m} \quad (11)$$

where the constant a_0 is set equal to $1.4 \cdot 10^{-2}$ following the observation in [17] that this value compares favorably with the frequency spectrum parameter values reported in [20]. The calculation of u^* is performed through the log-law equation for boundary layer flows:

$$U_{10} = \frac{u^*}{\kappa} \ln \left(\frac{z}{z_0} \right) \quad (12)$$

with $z = 10$ m, the universal constant $\kappa = 0.4$, and z_0 is the near-surface aerodynamic roughness length, which is estimated from the following semi-empirical equation [21]:

$$z_0 = 3.7 \cdot 10^{-5} \frac{U_{10}^2}{g} \left(\frac{U_{10}}{c_p} \right) \quad (13)$$

In order to demonstrate a more realistic ocean environment, short-crested seas, i.e., seas where the wave propagation is not unidirectional relative to the wind direction, are also included in the wave simulation. This can be accomplished by multiplying eq. (1) by a spreading function to obtain a directional spectrum. The latter is the Fourier transform of the auto-covariance of the free-surface elevation, which is a real and even function and, thus, the Fourier series expansion of the spreading function must contain only even harmonics. In this research, the spreading function proposed in [17] is utilized:

$$\Phi(k, \phi) = \frac{1}{2\pi} \cdot [1 + \Delta(k) \cdot \cos(2\phi)] \quad (14)$$

where ϕ is the wave propagation direction relative to the wind direction and $\Delta(k)$ is the coefficient of the second harmonic of the truncated Fourier series expansion of the spreading function $\Phi(k, \phi)$, which is computed as:

$$\Delta(k) = \tanh \left\{ \frac{\ln(2)}{4} + 4 \cdot \left(\frac{c}{c_p} \right)^{2.5} + 0.13 \cdot \frac{u^*}{c_m} \cdot \left(\frac{c_m}{c} \right)^{2.5} \right\} \quad (15)$$

Therefore, by combining the omnidirectional spectrum from eq. (1) and the spreading function from eq. (14), we obtain the unified directional spectrum [17]:

$$\Psi_{k,\phi}(k, \phi) = \frac{1}{k} \cdot \Phi(k, \phi) \cdot S_k(k) \quad (16)$$

The computation of the wave elevation $\eta(x, y, t)$ at the location of the buoy can be performed through a linear superposition of N discrete wave components, each with wavenumber k_n , and M discrete values of the angle ϕ_m , i.e., the angle between the wave propagation direction and the wind direction ϕ_m .

$$\eta(x, y, t) = \sum_{n=0}^{N/2} \sum_{m=1}^M \sqrt{\Psi_{k_n, \phi_m} k_n \Delta k_n \Delta \phi_m} \sin(\omega_n t - k_n x \cos \phi_m - k_n y \sin \phi_m + \varepsilon_{nm}) \quad (17)$$

where ε_{nm} is a random phase angle uniformly distributed in $[0, 2\pi]$ and the angle ϕ_m can take values in $[-\pi, \pi]$. The computation of the wave elevation can be facilitated by utilizing an inverse Fast Fourier Transform (FFT). In order to apply the inverse FFT, eq. (17) is written in the following form:

$$\eta(x, y, t) = \sum_{n=-N/2}^{N/2} (a_n - ib_n) e^{i\omega_n t} \quad (18)$$

with,

$$a_n = \sum_{m=1}^M \sqrt{\Psi_{k_n, \phi_m} k_n \Delta k_n \Delta \phi_m} \cos(k_n x \cos \phi_m + k_n y \sin \phi_m + \varepsilon_{nm})$$

$$b_n = \sum_{m=1}^M \sqrt{\Psi_{k_n, \phi_m} k_n \Delta k_n \Delta \phi_m} \sin(k_n x \cos \phi_m + k_n y \sin \phi_m + \varepsilon_{nm})$$

In the WEC simulations, we have used 256 components for k_n and ϕ_m , i.e., $N = 256$ and $M = 256$ with k_n in the range $[0.04, 4]$ rad/m.

III. WAVE-BUOY INTERACTION AND WAVE ENERGY ABSORPTION

The time-domain simulation of the wave energy conversion process using a hemispherical (half-submerged) buoy is described in this section. The incident wave exerts a force on the buoy. This force can be computed by utilizing the model for the short-crested, irregular waves, eq. (16), to obtain the spectrum of the wave excitation force,

$$S_{FW} = |H(\omega)|^2 \cdot \Psi_{k,\phi} \quad (19)$$

where $H(\omega)$ is the force transfer function, which facilitates the computation of the magnitude of the force per unit input, i.e., wave force per unit wave amplitude. According to Faltinsen [22], the force transfer function for a heaving spherical buoy can be written as:

$$H(\omega) = \sqrt{\frac{2\rho g^3 B_h(\omega)}{\omega^3}} \quad (20)$$

where $B_h(\omega)$ is the radiation damping coefficient, which for a hemispherical (half-submerged) buoy can be obtained from [23], and ρ is the fluid density. The wave frequency ω is obtained from the corresponding wave number from eq. (2). By combining eqs. (18) – (20) and using an inverse FFT, the time series of the incident wave excitation force F_W is obtained.

In addition to the force due to the incident wave, the power take-off mechanism that converts the wave energy into mechanical energy exerts a force on the buoy, F_{PTO} . In this work, we assume that this force is modeled as a viscous (linear) damper:

$$F_{PTO}(t) = -B_{PTO} \cdot \dot{\zeta}(t) \quad (21)$$

where the damping coefficient B_{PTO} is constant and equal to the radiation damping coefficient at the spectral peak frequency, $B_h(\omega_p)$, and $\dot{\zeta}(t)$ is the vertical velocity of the buoy. The heaving motion of the buoy results in the production of waves radiated away from the buoy, which causes an additional force exerted on the buoy by the fluid, the radiation force, F_R :

$$F_R(t) = -m_R(\infty) \cdot \ddot{\zeta}(t) - \int_{-\infty}^t \kappa(t - \tau) \dot{\zeta}(\tau) d\tau \quad (22)$$

where $m_R(\infty)$ is the added mass of the buoy at infinite frequency, $\ddot{\zeta}(t)$ is the vertical acceleration of the buoy, and $\kappa(t)$ is the radiation force kernel. For a heaving hemisphere, $m_R(\infty)$ is equal to approximately half the mass of the buoy, m_b [23]. The radiation force kernel is computed as:

$$\kappa(t) = m_b \frac{2}{\pi} \int_0^\infty B_h(\omega) \cdot \cos(\omega t) d\omega \quad (23)$$

The convolution integral in eq. (22) is computed numerically using the trapezoidal rule. Finally, the net force between buoyancy and weight of the buoy generated due to the displacement $\zeta(t)$ of the buoy from its equilibrium position corresponds to the hydrostatic force, F_{HS} :

$$F_{HS}(t) = -\rho g A_W \zeta(t) \quad (24)$$

where A_W is the cross-sectional area of the buoy at the free-surface plane. For a floating buoy with a single degree of freedom (heave), the rigid body equation of motion is [24]:

$$m_b \ddot{\zeta}(t) = F_W(t) + F_{PTO}(t) + F_R(t) + F_{HS}(t) \quad (25)$$

Equation (25) combined with eqs. (21), (22), and (24) result in the following integro-differential equation:

$$(m + m_R(\infty)) \ddot{\zeta}(t) + \int_{-\infty}^t \kappa(t - \tau) \dot{\zeta}(\tau) d\tau + B_{PTO} \cdot \dot{\zeta}(t) + \rho g A_W \zeta(t) = F_W \quad (26)$$

This equation is solved using a 4th order Runge-Kutta solver with a fixed time step of 0.05s. The average absorbed power over a time period T can be calculated using the following equation:

$$P_{ave} = \frac{1}{T} \int_0^T F_{PTO}(t) \cdot \dot{\zeta}(t) dt \quad (27)$$

If the instantaneous absorbed power is measured at N discrete time intervals over a time period T , then eq. (27) can be rewritten in the following form to compute its root mean squared value:

$$P_{m,rms} = \sqrt{\frac{1}{N} \sum_{n=0}^{N-1} F_{PTO}(t_n) \dot{\zeta}(t_n)} = \sqrt{\frac{1}{N} \sum_{n=0}^{N-1} B_{PTO} (\dot{\zeta}(t_n))^2} \quad (28)$$

The physics-based simulator used in the VR system is based on the aforementioned equations for the ocean waves and the wave-buoy interaction and it was developed in MATLAB[®]. The wind speed can be configured to create different settings of the ocean.

IV. SOFTWARE INTEGRATION AND INTERFACE WITH WEC HARDWARE MECHANISM

The integrated VR system was developed around the three main blocks shown in Fig. 1.a: The physics-based simulator in MATLAB[®], the game engine in Unity 3D, and the hardware controller in LabVIEW[®]. Whereas Unity 3D helps to visualize the waves and the buoy in real time, LabVIEW is responsible for controlling the hardware (stepper motor). These three blocks work in a decentralized mode and communicate with each other as nodes in a network. The entire WEC system is shown in Fig. 1.b.

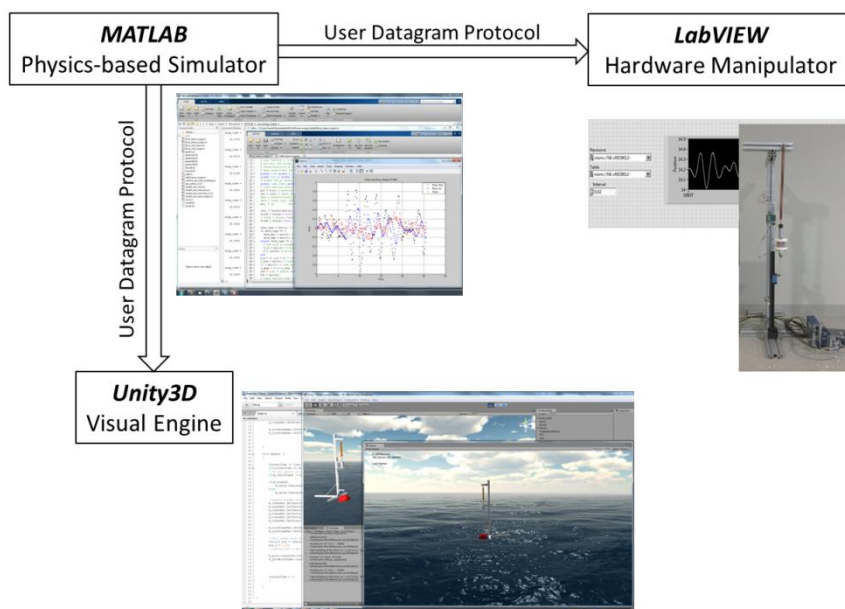


Figure 1.a Data flow block diagram.



Figure 1.b The Wave Energy Converter

In order to capture the motion of the buoy from the physics-based simulator, the data in MATLAB[®] is streamed in a lock step synchronously to both Unity 3D and LabVIEW[®]. Once the time step and other simulation parameters have been selected, the simulation code in MATLAB[®] generates the motion profile of the buoy at a single time interval. The User Datagram Protocol (UDP) is then employed to transfer the buoy motion profile at every time interval to the other two blocks: The hardware controller to actuate the WEC mechanism motor and the game engine to visualize the simulation. UDP is the networking protocol that grants the applications direct access to the data transport service. The real time synchronization is achieved by imposing the MATLAB[®] simulator to send buoy's position and velocity simultaneously to Unity 3D and the hardware controller at the interval of 0.1 second clock time. The buoy's motion profile is obtained by solving the buoy equation, eq. (26) numerically.

The simulation time used in the ODE solver is in general shorter than the real clock time. Once the simulator finds the buoy's profile at 0.1 seconds, it will pause temporally until the clock time also reaches 0.1 second interval and then send out the data wirelessly. The Unity 3D spends its simulation time to generate random wave patterns and render their image. The duration of the simulation time for wave generation depends on the size of the random numbers associated with wavenumber k_n , and the angle ϕ_m for wave generation and while the rendering time depends on the grid size. The component number is set to be 256 for both wavenumber and angle and the grid size is 300x300. The Unity 3D has a built-in counter for clock time. The wave patterns generated by its simulator will be updated at every 0.1 second interval of clock time. Unity 3D will start rendering its image as soon as it receives the buoy profile data. The process will generate a synchronized and smooth motion of waves and the buoy at 10 frames per second in the virtual environment.

LabVIEW[®] is the software responsible for controlling the hardware of the WEC mechanism via a C-Rio 9012 controller. It was programmed to accept the data from the MATLAB[®] simulation code and then use this data to actuate the hardware in real time. The controller was programmed to listen to a pre-identified port in the network at all times. In addition to the controller, a WEC mechanism was built, as shown in Fig. 2, in order to convert the mechanical energy into electricity and, thus, produce a hybrid WEC VR system with enhanced simulation capabilities. When the data sent by MATLAB[®] through UDP has arrived at the port, the C-Rio immediately seizes it. The buoy position data is stored in the C-Rio memory first, and then is utilized to calculate and transmit the right signal to the motor controller to replicate the heaving buoy motion provided by the simulation in MATLAB[®]. Since LabVIEW[®] requires at least 20 data points of the buoy motion profile initially in order to calculate the contour that the stepper motor will follow, there is a slight time lag between the instant data is received and the instant the WEC mechanism starts to move.

The WEC mechanism consists of a crane, a magnetic rod, a coil, an LED board, and a spring at the top. The crane, which is about 40 inches in height, was built to provide the mounting places and hold all the other components in place, as shown in Fig. 3. While the 6-inch-long magnetic rod travels up and down in sync with the buoy motion, the coil remains stationary. The 18-gauge diameter coil collects the change in flux created by the moving magnetic rod and converts it to current in order to light the LED on the circuit board. The spring at the top of the crane helps to hold the rod in place and allows it to move only in the desired direction. The motion of the magnetic rod is adjusted proportionally in the WEC mechanism so as to satisfy the limits of the power of the motor and the distance of the rail so that the heaving motion of the buoy is faithfully replicated in the hardware. For the selected wind speed and wave patterns selected in this study, no such adjustment is needed as the rail length can cover the vertical traveling distance of the buoy.

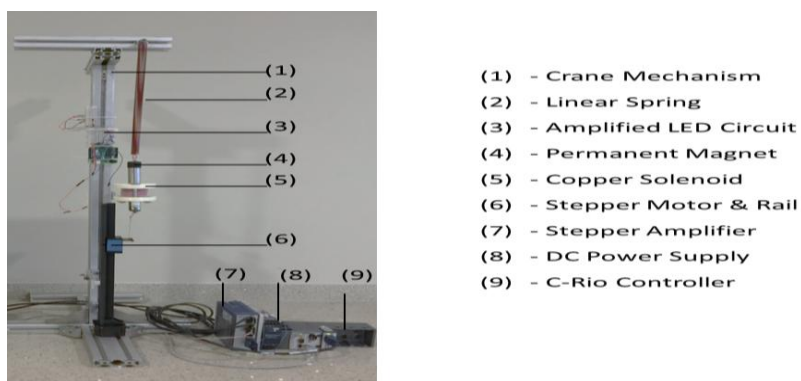


Figure 2. Overview of hardware set-up for the WEC mechanism.

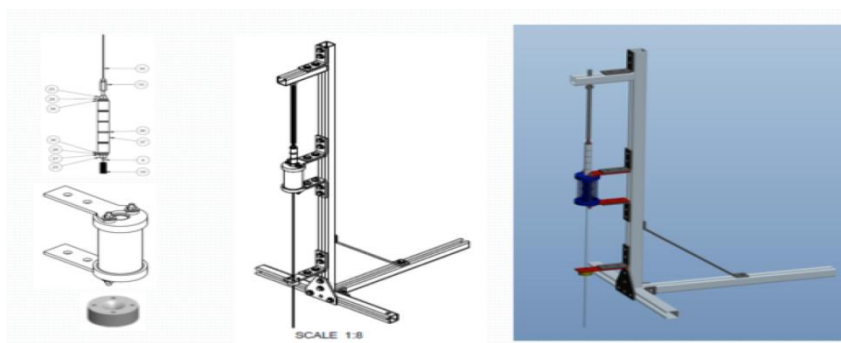


Figure 3. Details of the crane used in the WEC mechanism.

V. DEMONSTRATION OF THE WAVE ENERGY CONVERSION PROCESS

In this section, four cases with different wind speeds, 2, 4, 6 and 8 m/s, respectively, are simulated in order to demonstrate the working principle of the WEC process under various sea conditions. The wave profile is generated in the physics-based simulator using the unified directional spectrum from eq. (18) and assuming that the aforementioned wind speeds occur at 10 m above the sea surface and are sustained over a fetch of 100 km; these conditions are typical of fully-developed seas. A half-submerged spherical buoy with radius of 1 m is utilized in the simulations. As the wind speed increases, the average wave amplitude increases as shown in Fig. 4 (a) – (d). The corresponding motion of the buoy is also shown in these figures. The amplification of the motion of a WEC device is achieved when it operates at near-resonance conditions. A necessary condition for that is the buoy velocity be in phase with the wave excitation [25]. In regular waves, this can be achieved when the damping of the power-take-off (PTO) mechanism is equal to the radiation damping of the wave frequency [26]. When the WEC device is operating in irregular waves, the control of the buoy motion is typically performed by adjusting the damping of the power-take-off (PTO) mechanism either in a pseudo-continuous manner or via discrete control, e.g., latching [27]. In the current simulations, a simpler passive control approach is employed: the damping of the PTO mechanism is preset to match the radiation damping at the peak spectral frequency. Even though in this way the energy absorption in irregular waves is suboptimal, it still suffices to demonstrate the WEC process, without the requirement for prediction of the wave excitation [26].

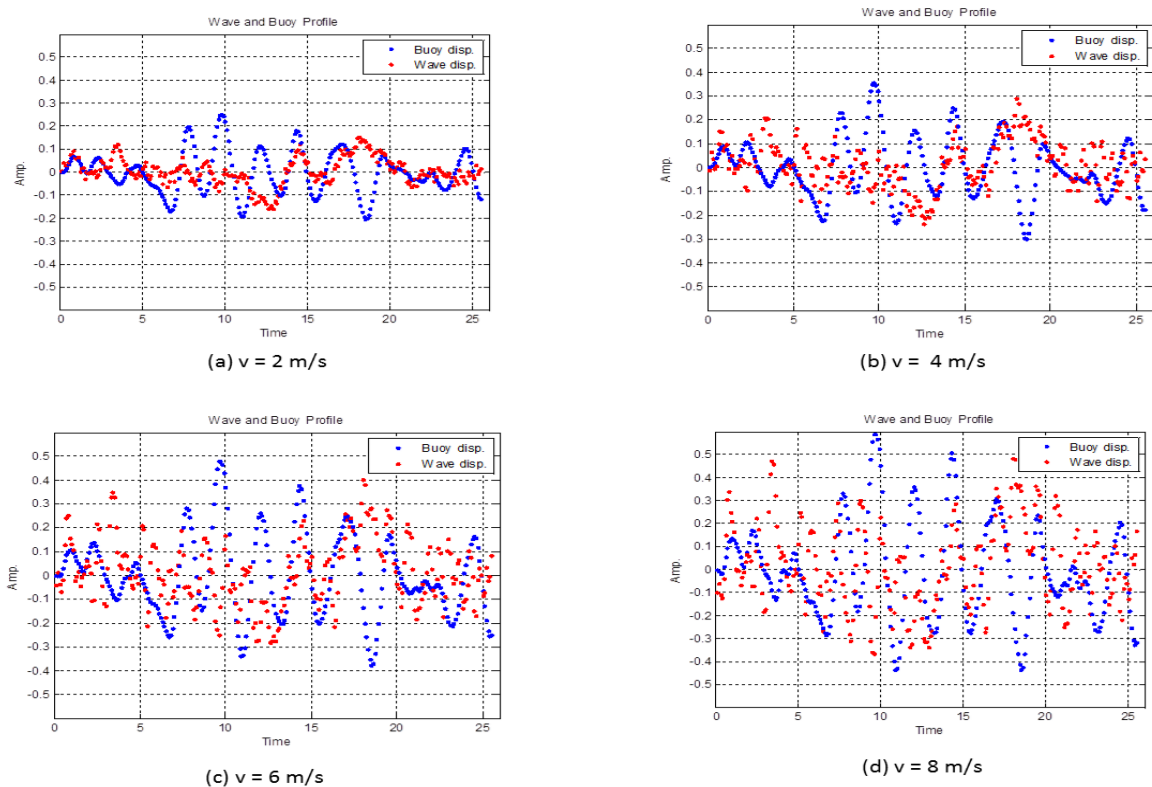
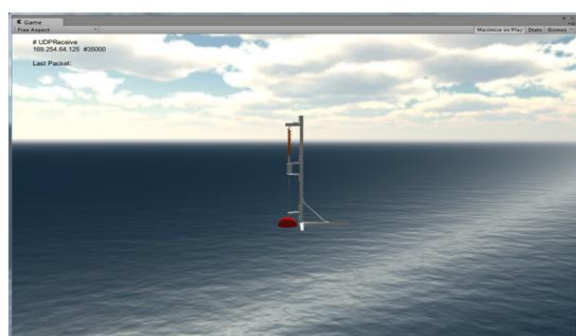


Figure 4. Buoy motion and wave profile (in meters) at different wind speeds.

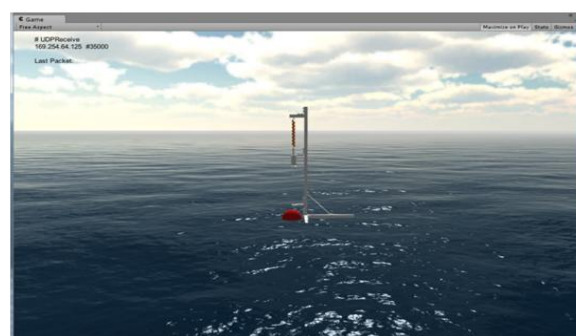
Next, the ocean waves are captured in the Unity 3D game scene, to show the working process of the wave energy conversion. The wind speeds in this virtual environment feature different ocean conditions from calm and glassy to rough seas as shown in Fig. 5 (a) – (d). As already mentioned, the WEC converts the heaving motion of the buoy to electric current. The time series of the electric current is collected using the WEC mechanism shown in Fig. 2 for each of the four cases. The corresponding power spectrum profiles collected from the WEC mechanism are plotted in Fig. 6 (a) – (d). It can be easily observed that there is no dominant frequency at which the electric current is generated. The root mean squared electrical power can be calculated as:

$$P_{e,rms} = \sqrt{\frac{1}{N} \sum_{n=0}^{N-1} p^2(t_n)} \quad (29)$$

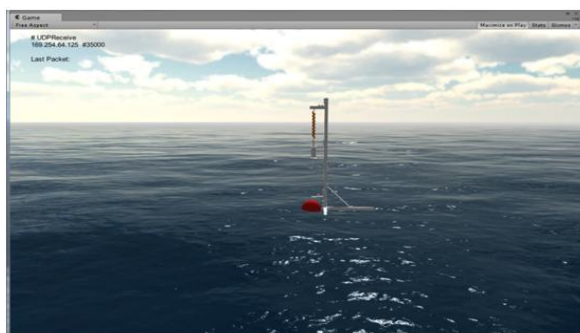
Apparently, while the difference in power between the 2 and 4 m/s wind speed cases is not significant, the two latter cases show an increase of 22.3% and 46.2%, respectively, compared to the 2 m/s wind speed case. The theoretical value of the root mean squared absorbed mechanical power of the buoy, i.e., neglecting friction and power take-off mechanism losses, obtained from eq. (28) and the corresponding electrical power for each of the four cases are presented in Fig. 7. This ratio is indicative of the WEC absorption efficiency. Even though the amount of absorbed power is greater at higher wind speeds, the efficiency drops mainly as a result of available hardware limitations, i.e., the limited useful range of change in magnetic flux of the utilized coil shown in Fig. 2.



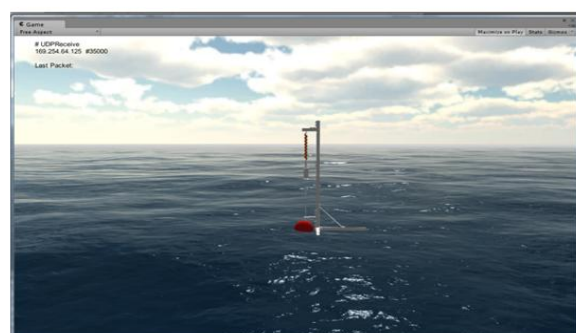
(a) $v = 2$ m/s



(b) $v = 4$ m/s



(c) $v = 6$ m/s



(d) $v = 8$ m/s

Figure 5. Ocean surface in Unity3D at different wind speeds.

VI. CONCLUSIONS AND DIRECTIONS FOR FUTURE RESEARCH

The development of a hybrid virtual reality (VR) software that simulates the wave energy conversion (WEC) process of a heaving buoy is described in this article. This VR system comprises three main function blocks: a physics-based simulator in MATLAB[®], a game studio in Unity 3D, and a hardware manipulator in LabVIEW[®]. The VR software is also combined with a WEC mechanism in order to demonstrate the conversion of mechanical energy into electricity. The software was tested and validated in irregular seas. The absorbed wave energy was calculated and the efficiency of the conversion process was quantified. The experiments demonstrated that the developed VR system can be utilized as both a research and an educational tool. Furthermore, the versatility of the employed wave spectrum regarding the modeling of irregular waves and the modularity of the VR system tools allow for easy implementation of a wide range of WEC simulation scenarios.

A number of improvements that would enhance the effectiveness of the hybrid VR WEC simulation system are currently considered. First, as already mentioned, the utilization of a passive control strategy for the heaving buoy motion is far from optimal, thus, a more effective control method will be implemented in the near future. In addition to this, the utilization of an electromagnetic coil that would allow for increased conversion efficiency and easier manipulation of the amount of generated electricity is currently under way. Finally, the code developed for the VR system will be optimized in order to minimize the time lag in the communication between its three function blocks.

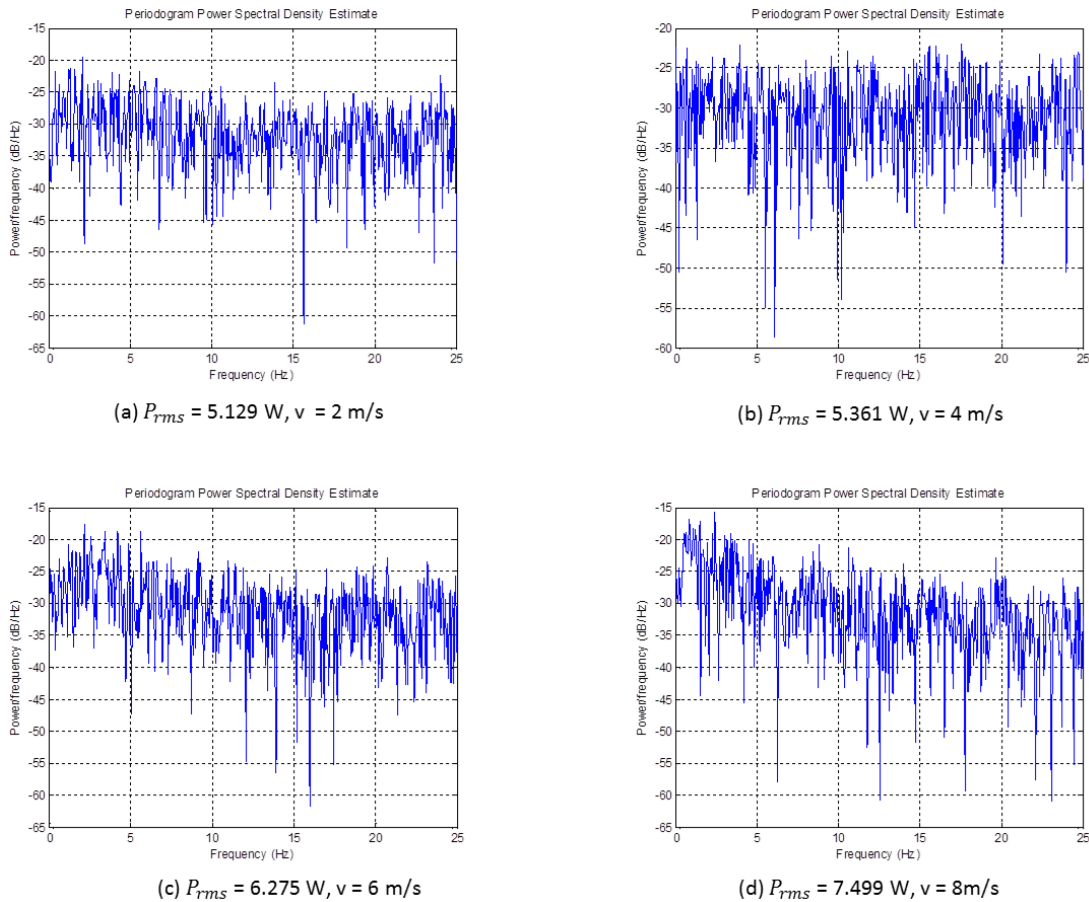


Figure 6. Electrical power at different wind speeds.

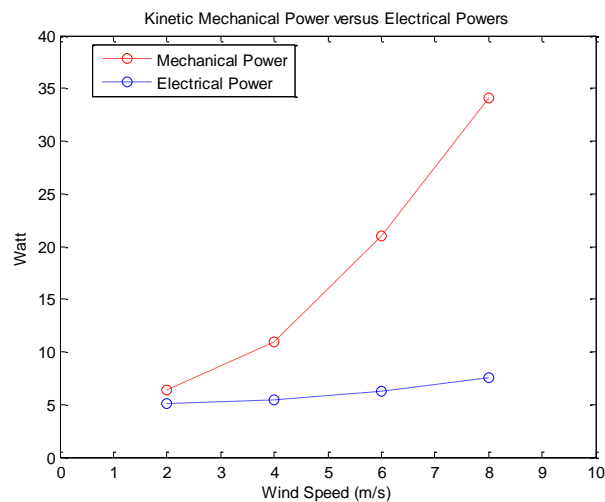


Figure 7. Mechanical vs. electrical power at different wind speeds.

ACKNOWLEDGMENTS

The authors would like to acknowledge the financial support provided by the U.S. National Science Foundation (NSF) through grant # 1245769. Additionally, JW acknowledges partial support from NSF grant # 1319078.

REFERENCES

- [1] T.A. Mikropoulos and A. Natsis. Educational Virtual Environments: A Ten-Year Review of Empirical Research (1999-2009). *Computers and Education*, 56:769-780, 2011.
- [2] A. Gadre, E. Cudney, and S. Corns. Model Development of a Virtual Learning Environment to Enhance Lean Education. *Procedia - Computer Science*, 6:100-105, 2011.
- [3] S.K. Ong, and M.A.Mannan. Virtual Reality Simulations and Animations in a Web-based Interactive Manufacturing Engineering Module. *Computers & Education*, 43:361-82, 2004.
- [4] B. Dalgarno, A.G. Bishop, W. Adlong, and D.R. Bedgood Jr. Effectiveness of a Virtual Laboratory as a Preparatory Resource for Distance Education Chemistry Students. *Computers & Education*, 53:853-865, 2009.
- [5] K.F. Saleh, A.M. Mohamed, and H. Madkour. Developing Virtual Laboratories Environments for Engineering Education. *International Journal of Arts and Sciences*, 3(1):9-17, 2009.
- [6] P.T. Goeser, W.M. Johnson, F.G. Hamza-Lup, and D. Schaefer. VIEW – A Virtual Interactive Web-based Learning Environment for Engineering. *IEEE Advances in Engineering Education*, 2(3):24, 2011.
- [7] X. Hu and B.P. Zeigler. Model Continuity in the Design of Dynamic Distributed Real-Time Systems. *IEEE Transactions on Systems, Man and Cybernetics – Part A: Systems and Humans*, 35(6):867-878, 2005.
- [8] J. Richardson, N. Adamo-Villani, E. Carpenter, and G. Moore. Designing and Implementing a Virtual 3D Microcontroller Laboratory Environment. In: *Proceedings of the 36th ASEE/IEEE Frontiers in Education Conference*, October 28-31, San Diego, CA, 2006.
- [9] D. Morris, C. Sewell, N. Blevins, F. Barbagli, and K. Salisbury. A Collaborative Virtual Environment for the Simulation of Temporal Bone Surgery. *Medical Image Computing and Computer-Assisted Intervention, Lecture Notes in Computer Science*, 3217:319-327, 2004.
- [10] Y. Fu, C. Chen, and J. Cai. Research on Virtual Reality Simulation System of Safe Navigation Environment in Three Gorges Reservoir Area. *Procedia - Environmental Science*, 10:331-336, 2011.
- [11] J.K. Crosier, S. Cobb, and J.R. Wilson. Key Lessons for the Design and Integration of Virtual Environments in Secondary Science. *Computers & Education*, 38:77-94, 2002.
- [12] M. Mircea. SOA Adoption in Higher Education: A Practical Guide to Service- Oriented Virtual Learning Environment. *Procedia – Social and Behavior Sciences*, 31:218-223, 2012.
- [13] C. Bouras, E. Giannaka, and T. Tsiatsos. A Simulation Modelling Tool for Distributed Virtual Environments. *Simulation Modeling Practice and Theory*, 25:1-16, 2012.
- [14] A.G. Abulrub, A. Attridge, and M.A Williams. Virtual Reality in Engineering Education: The Future of Creative Learning.
- [15] R. Lindgren. Generating a Learning Stance through Perspective-taking in a Virtual Environment. *Computers in Human Behavior*, 28:1130-1139, 2012.
- [16] D.E. Hasselmann, M. Dunkel, and J.A. Ewing. Directional Wave Spectra observed during JONSWAP 1973. *Journal of Physical Oceanography*, 10(8):1264-1280, 1980.
- [17] T. Elfouhaily, B. Chapron, K. Katsaros, and D. Vandemark. A Unified Directional Spectrum for Long and Short Wind-Driven Waves. *Journal of Geophysical Research*, 102(C7):15,781-15,796, 1997.
- [18] M.A Donelan, J. Hamilton, and W.H. Hui. Directional Spectra of Wind-Generated Waves. *Philosophical Transactions of the Royal Society of London A*. 315:509-562, 1985.
- [19] W.J. Pierson and L. Moskowitz. A Proposed Spectral Form for Fully Developed Wind Sea based on the Similarity Theory of S.A. Kitaigorodskii. *Journal of Geophysical Research*, 69(24):5181-5190, 1964.
- [20] Y. Toba. Local Balance in the Air-Sea Boundary Processes, III, On the Spectrum of Wind Waves. *Journal of the Oceanographical Society of Japan*. 29:209-220, 1973.
- [21] M.A. Donelan, F.W. Dobson, S.D. Smith, and R.J. Anderson. On the Dependence of Sea Surface Roughness on Wave Development. *Journal of Physical Oceanography*, 23(9):2143-2149, 1993.
- [22] O.M. Faltinsen. *Sea Loads on Ships and Offshore Structures*. 1st edition. Cambridge University Press, 1990.
- [23] H. Hulme. The Wave Forces Acting on a Floating Hemisphere Undergoing Forced Periodic Oscillations. *Journal of Fluid Mechanics*, 121:443-463, 1982.
- [24] E.R. Jefferys. Device characterization. In: B.M. Count (Ed.), *Power from Sea Waves*. Academic Press, pp. 413-438, 1980.
- [25] J. Falnes. *Ocean Waves and Oscillating Systems*. 1st edition, Cambridge University Press, 2002.
- [26] H. Yavuz, T.A. Stallard, A.P. McCabe, and G.A. Aggidis. Time Series Analysis-based Adaptive Tuning Techniques for a Heaving Wave Energy Converter in Irregular Seas. *Proceedings of the Institution of Mechanical Engineers, Part A: Journal of Power and Energy*. 221:77-90, 2007.
- [27] A.F. de O. Falcao, Phase Control through Load Control of Oscillating-Body Wave Energy Converters with Hydraulic PTO System. *Ocean Engineering*, 35:358-366, 2008.

Using Computational Fluid Dynamics as a tool for improved prediction of pressure characteristics of a pilot chamber of PRSOV

Binod Kumar Saha¹, Dipankar Sanyal²

¹ Product Design and Simulation Division,

CSIR-Central Mechanical Engineering Research Institute, Durgapur – 713209, India,

² Department of Mechanical Engineering, Jadavpur University, Kolkata – 700032

ABSTRACT:

In this paper, flow of air through a pressure regulating and shut-Off Valve (PRSOV) has been solved numerically with an objective to determine the pressure of the PRSOV pilot chamber. Flow through the valve is transient, compressible and turbulent in nature. Flow has been solved using ANSYS FLUENT coupled with a special user defined function (UDF). UDF is used for dynamic meshing, automatic data acquisition from ANSYS FLUENT solver and to schedule the numerical test procedure. Within the UDF, valve inlet pressure is varied in a stepwise manner. For every value of inlet pressure, transient analysis leads to a quasi-static flow through the valve. Spool forces are calculated based on different pressures at inlet. From this information of spool forces, pressure characteristic of the pilot chamber of passive control circuit has been derived. The same characteristics have also been obtained after modelling the flow analytically. Both the results have been compared. It is observed, CFD analysis of the flow has led to improved results.

KEYWORDS: Pressure regulating and Shut-Off Valve, pilot flow, dynamic meshing, flow force, pressure regulation, Force Balance, CFD

I. INTRODUCTION

Pressure regulating and Shut-off valve is a critical component used in many fluid power systems, especially in aircraft. The valve is used in Environmental Control System of the aircraft. The valve is installed in a pipe line in an air flow path where available inlet pressure to the valve may vary within a wide range. The main function of the valve is to regulate the air flow and maintain almost constant pressure at its outlet. Schematic diagram of the valve is shown in Fig. 1.

A passive control circuit (Pilot chamber pressure control circuit in Fig. 1) is required to achieve the above objective. Depending upon the valve inlet pressure, this passive control circuit sets the criterion for position of spool inside the valve. Determination of characteristics of the control circuit is a crucial part in designing the control circuit and hence the pressure regulated valve. This requires complete information of flow forces acting on the valve spool. Calculations based on theoretical model can provide some initial approximate information. With the advent of numerical power, advanced, sophisticated and reliable CFD tool is very useful in determining the various flow forces acting on the spool.

Leutwyler and Dalton [1] showed the potential of CFD tool in analyzing compressible, turbulent flow through butterfly valves. ANSYS FLUENT was used for the analysis. Amirante et al. [2-3] evaluated flow forces on an open centre direction control valve. Amirante et al. [4] again modelled direct proportional valve using CFD. Compensation techniques based on spool profiling were used to balance the flow force at different level of valve openings. Chen et al. [5] reported flow visualization using CFD in a ball valve. Chattopadhyay et al. [6] have investigated turbulent flow structure inside a Pressure Regulating and Shut-Off Valve using ANSYS FLUENT. In this work, both 2-D and 3-D simulations were performed with a conclusion that 2-D model could predict the flow coefficients satisfactorily. Song et al. [7] have reported 2D dynamic simulation of a pressure relief valve using CFD.

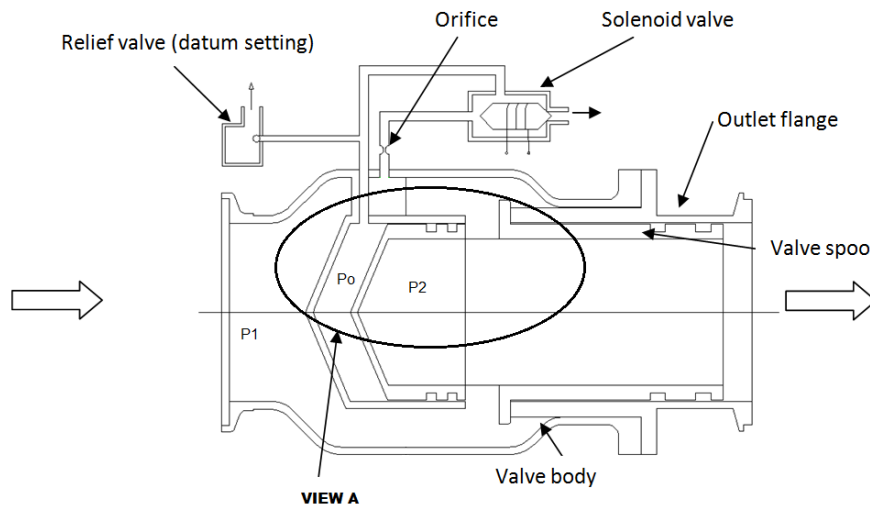
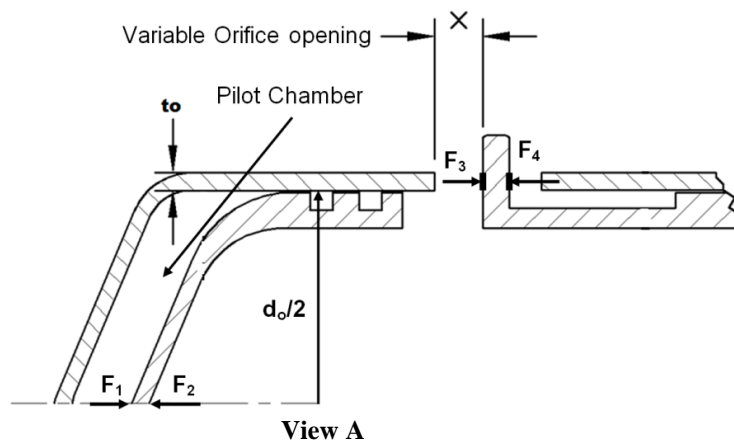


Fig. 1. Schematic diagram of pressure regulated valve



In this study, transient, compressible and turbulent flow through a pressure regulated valve has been solved using commercial software ANSYS FLUENT [10]. As the valve inlet pressure changes, spool inside the valve as shown in Fig. 1 must move in appropriate direction to keep outlet pressure constant. Starting from the instant of inlet pressure change, a transient analysis is performed to reach the state of quasi-static flow through the valve.

II. ANALYTICAL METHOD

Pressure Regulating and Shut-Off Valve (PRSOV) consists of valve body, spool and pilot chamber. Inlet pressure (P_1) of the valve may vary from 207 kPa to 758 kPa. Main function of the valve is to keep the outlet pressure (P_2) at almost constant value. Spool inside the valve body is subjected to a number of forces. When there is a change in inlet pressure, spool moves in appropriate direction and outlet pressure should remain almost constant value.

2.1 Force balance on the spool

spool moves under the action of four forces, F_1 , F_2 , F_3 and F_4 as shown in Figure1. Force F_1 arises due to the pilot chamber air pressure (P_0). Pilot chamber air pressure is controlled by datum setting of relief valve as shown in Fig. 1. The effective area on which this pilot pressure acts is $\pi d_o^2/4$. Therefore, $F_1 = P_0 \times \frac{\pi d_o^2}{4}$ and acts from left to right direction as shown in Figure1.

As the high pressure air flows through the variable orifice, air pressure reduces from inlet pressure (P_1) to outlet pressure (P_2). This outlet pressure acts on the other side of the spool head. Thus a force (F_2) acts on the spool from right to left direction as shown in Fig. 1. Here, $F_2 = P_2 \times \frac{\pi d_o^2}{4}$.

Air pressure changes from P_1 to P_2 as it flows through the orifice. Orifice is formed by spool flange and the valve body thickness (t_o). Since t_o is small enough, so pressure variation is assumed linear. Therefore, average pressure $(P_1 + P_2)/2$ acts on spool flange over an annular area with diameter $(d_o + t_o)$ and thickness t_o .

Here the force, $F_3 = \frac{(P_1 + P_2)}{2} \times \pi(d_o + t_o) \times t_o$. Since t_o is small value, so higher order term of t_o can be neglected. Then, $F_3 = \frac{(P_1 + P_2)}{2} \times \pi d_o \times t_o$ and the force (F_4), which acts on similar area on the other side of the spool flange, is given as $F_4 = P_1 \times \pi d_o \times t_o$.

Spool remains at equilibrium state under the action of these four forces. Therefore, $F_1 + F_3 = F_2 + F_4$
 or, $P_o \times \frac{\pi d_o^2}{4} + \frac{P_1 + P_2}{2} \times \pi d_o \times t_o = P_1 \times \pi d_o \times t_o + P_2 \times \frac{\pi d_o^2}{4}$
 or, $P_o = \frac{t_o}{2d_o} \times P_1 + \left(1 - \frac{t_o}{2d_o}\right) \times P_2$.

III. CFD METHOD

3.1 Mathematical modelling

The ANSYS FLUENT package has been used to solve the axisymmetric flow in the domain shown in Fig. 2. The partial differential equations for the conservation of mass, momentum, energy, turbulence kinetic energy k and turbulence dissipation rate ε along with the algebraic equation for the perfect gas laws have been solved. As given below, these involve time t as the independent variable, the dependent variables of density ρ , velocity \bar{v} , pressure p , temperature T and the flow parameters of kinematic viscosity ν_l , turbulent viscosity ν_t , molecular diffusivity α_l and turbulent diffusivity α_t .

Mass conservation equation: $\partial \rho / \partial t + \nabla \cdot (\rho \bar{v}) = 0$,

Momentum conservation equation:

$$\partial (\rho \bar{v}) / \partial t + \nabla \cdot (\rho \bar{v} \bar{v}) = -\nabla p + \rho (\nu_l + \nu_t) \nabla \cdot \{ \nabla \bar{v} + (\nabla \bar{v})^T - (2\bar{I}/3) \nabla \cdot \bar{v} \},$$

Energy conservation equation:

$$\partial T / \partial t + \bar{v} \cdot \nabla T = -(\alpha_l + \alpha_t) \nabla^2 T + (\nabla \bar{v}) : [\rho (\nu_l + \nu_t) \{ \nabla \bar{v} + (\nabla \bar{v})^T - (2\bar{I}/3) \nabla \cdot \bar{v} \}],$$

Turbulence Kinetic Energy Equation:

$$\partial (\rho k) / \partial t + \nabla \cdot (\rho \bar{v} k) = \nabla \cdot [\rho (\nu_l + \nu_t / \sigma_k) \nabla k] + G_k - \rho \varepsilon - 2 \rho \varepsilon k / (\gamma R T),$$

Turbulence Dissipation Equation:

$$\partial (\rho \varepsilon) / \partial t + \nabla \cdot (\rho \bar{v} \varepsilon) = \nabla \cdot [\rho (\nu_l + \nu_t / \sigma_\varepsilon) \nabla \varepsilon] + \rho C_1 S \varepsilon - \rho C_2 \varepsilon^2 / (k + \sqrt{\nu \varepsilon}),$$

where $S = [\{ \nabla \bar{v} + (\nabla \bar{v})^T \} : \{ \nabla \bar{v} + (\nabla \bar{v})^T \} / 2]^{1/2}$,

$$G_k = \mu_t S^2,$$

C_1 and C_2 are constants and σ_k and σ_ε are turbulent Prandtl number respectively, R is the gas constant and γ is the specific heat ratio. Consistent with the realizable k- ε model due to Shih et al. [13], the equations and the values of the different parameters are chosen as

$$\nu_t = C_\mu k^2 / \varepsilon,$$

$$\alpha_t = \nu_l \cdot \nu_t / (\alpha_l \text{Pr}_t),$$

$$\text{and } \mu = \mu_o (T/T_o)^{3/2} \{ (T_o + s)/(T + s) \},$$

where μ_o and T_o are reference viscosity and temperature, s is Sutherland constant and Pr_t is the turbulent Prandtl number, which have been taken respectively as equal to 1.716×10^{-5} Pa-s, 273.11 K, 110.56 K and 0.85.

3.2 Boundary Conditions

Following boundary conditions were used for this analysis.

1. Inlet boundary where a fixed pressure condition is used. The inlet temperature is fixed at 633 K.
2. As discussed above, outlet boundary of the flow domain is open to ambient. So, pressure and temperature have been set to 101325 Pa and 298.15 K, respectively.
3. No-slip boundary condition is assigned for all the walls. The valve wall was assumed to be at adiabatic condition.
4. For prescribing turbulent quantities at the boundaries, several options are available. We have used a condition prescribing the level of turbulent intensity (TI) at around 5-10% in the incoming fluid stream which is a reasonable level of value used by researchers. Hydraulic diameter of 47.5mm in the incoming fluid stream has been considered.

The initial conditions are the steady state result corresponding to the pressure p_1 at the inlet of the valve body equal to 207 kPa and all other boundary conditions as stated above.

Flow geometry has been approximated with a 2D axisymmetric domain as shown in Fig. 2. Unstructured quadrilateral mesh has been generated using commercial software package ANSYS ICEM CFD. Dynamic mesh motion along with the movement of spool boundaries has been considered during mesh generation. Entire fluid flow domain has been divided into two parts as shown in Fig. 3. Mesh for zone 1 does not possess any motion, whereas mesh for zone 2 undergoes dynamic motion. Wall boundaries comprising spool surfaces move depending upon the conditions as mentioned in FLOWCHART in Fig. 5. Some of the internal edges also move with spool surfaces. One special internal edge has been selected to move with spool surfaces but at exactly half the speed of spool movement. This special movement serves a very important purpose; finer boundary layer of the variable orifice remains intact though the spool opening reduces. Initial mesh contains 0.2 million quadrilateral cells approximately.

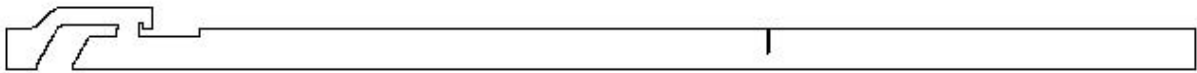


Fig. 2. 2D axi-symmetric flow domain

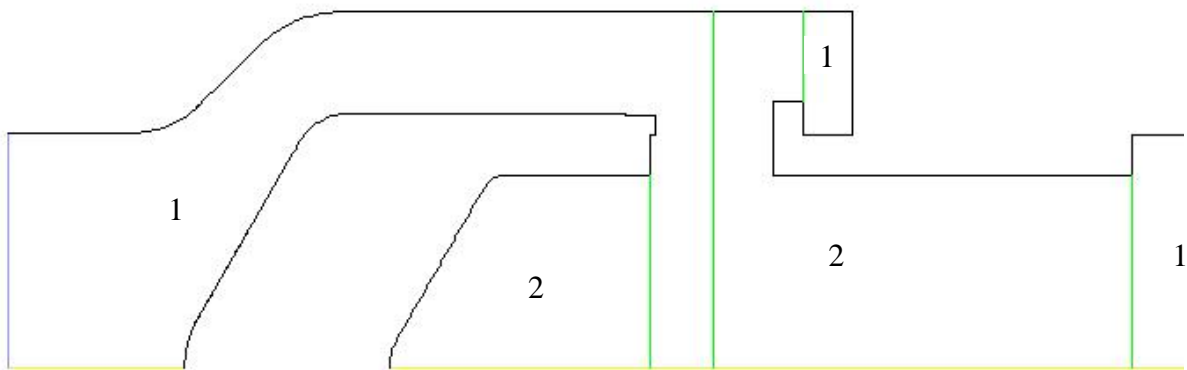


Fig. 3. Flow domain showing two different zones of fluid

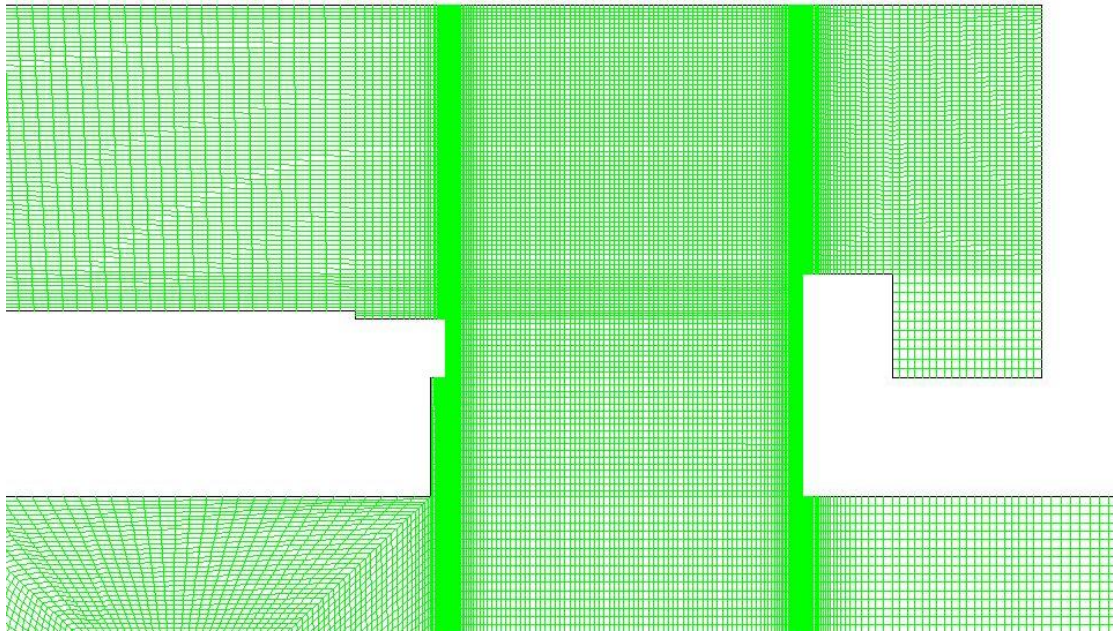


Fig. 4. Structured quadrilateral mesh around orifice opening

3.4 Methodology of calculation

Valve inlet pressure may vary from 207 kPa to 758 kPa, whereas valve outlet pressure remains within 200 kPa to 241 kPa. Air flow further downstream of valve outlet is approximated with the help of an orifice flow finally open to ground level condition. Calculation domain, therefore, includes the valve geometry along with the appropriate pipe length before and after the orifice. 2D axisymmetric flow geometry is shown in Fig. 2.

Transient flow through this flow domain is solved in ANSYS FLUENT to determine various spool openings depending on various inlet pressures. Now, when the inlet pressure is at the minimum value, i.e., 207 kPa, spool opening should be 100%. Therefore, solution of this flow sets the initial condition for transient calculation. In transient calculation, inlet pressure is varied in a step wise manner. This is done via a User Define Function (UDF). In reality, when inlet pressure is changed by a small amount, flow through the valve will take some time to die down the transient phenomena. In CFD, this quasi-static state is achieved after solving the transient flow for a number of time steps. For each time step, the flow convergence is checked using UDF that allows the calculation to move to next time step only after meeting the required criteria for convergence. Also, a check, whether quasi-static condition has been achieved, is carried out with the help of same UDF before proceeding to next time step. This UDF is described with the help of a FLOWCHART given in Fig. 5.

When the transient dies down pressure at valve outlet is checked for the desired outlet pressure. If desired pressure is not obtained, then spool opening is reduced by a delta amount and further transient calculation is carried on. This whole process is automated using the UDF. When the desired pressure is obtained, UDF directs ANSYS FLUENT to write the Case and Data file for further post processing. Spool opening and valve outlet pressure for each time step are written in a DAT file with the instruction written in UDF. This file is required for further reference. After achieving the desired pressure at valve outlet, UDF directs ANSYS FLUENT to increase the valve inlet pressure by a small amount and again the whole loop of operations repeated.

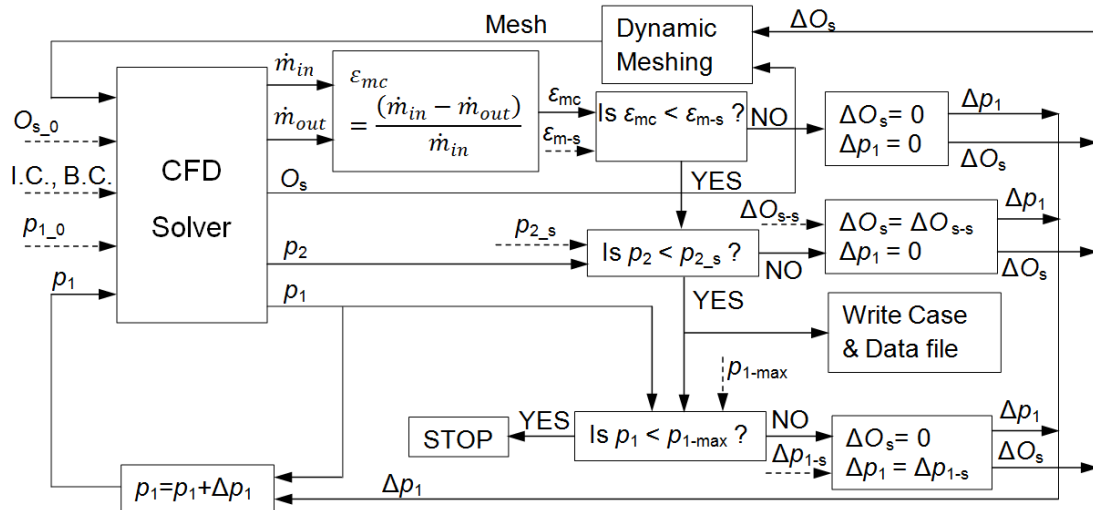


Fig. 5. FLOWCHART for special UDF

IV. RESULTS AND DISCUSSION

Flow through the pressure regulated valve is governed by variable orifice flow. Fig. 6 shows the spool opening in mm against the gauge pressure at valve inlet. It is observed here that spool opening reduces by 86% as valve inlet pressure increases from 240kPa to 360kPa. Thereafter, the gradient of change in spool opening with inlet pressure is very slow. This happens because pressure is almost fixed at valve outlet.

Fig. 7 shows the variation of mass flow rate with the change in inlet pressure. There is no significant change in mass flow rate. This is justified as two things happen simultaneously.

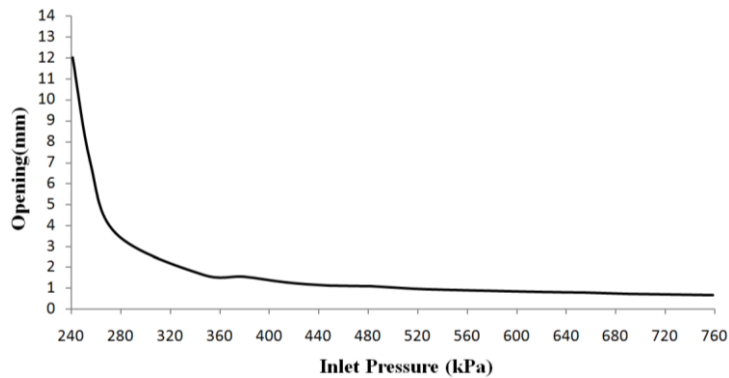


Fig. 6. Spool opening plotted against valve inlet pressure.

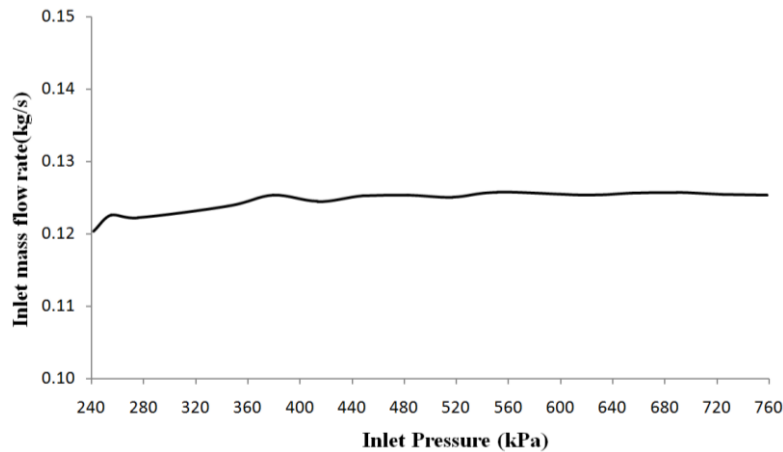


Fig. 7. Variation of mass flow rate through valve with change in inlet pressure.

Resistance in flow path increases as spool opening reduces, which would try to decrease mass flow rate. However, the increase in inlet pressure almost nullifies the above effect.

In Fig. 8 flow forces acting on spool surfaces are plotted against the inlet pressure. The force is acting axially from right to left direction with respect to Fig. 1. Both analytical and CFD results are plotted here. In both the cases, it is observed that the net force increases with increase in the inlet pressure. This owes to the fact that the spool opening creates an orifice and the air pressure acting on the orifice side of spool flange is less than the pressure that acting on the outer side of the spool flange. The derivation in Section 2.1 makes this aspect clearer. Higher absolute force is predicted by the CFD analysis. This pressure distribution and the consequent prediction of spool force is of course more realistic in view of the more detailed nature of the CFD analysis in comparison to a lumped calculation.

As the spool is subjected to a flow force from right to left, a counter force is required to keep the spool at the desired location. This force comes from pilot chamber air pressure. Air pressure in the pilot chamber is maintained by a Pilot Chamber Pressure Control circuit. There is a spring loaded Pressure Relief Valve in that circuit. The required pilot pressure to balance the spool is calculated and plotted in Fig. 9. Both Fig. 8 and Fig. 9 show that CFD analysis has led to sufficient improvement of the pilot chamber pressure characteristic with respect to the analytical results.

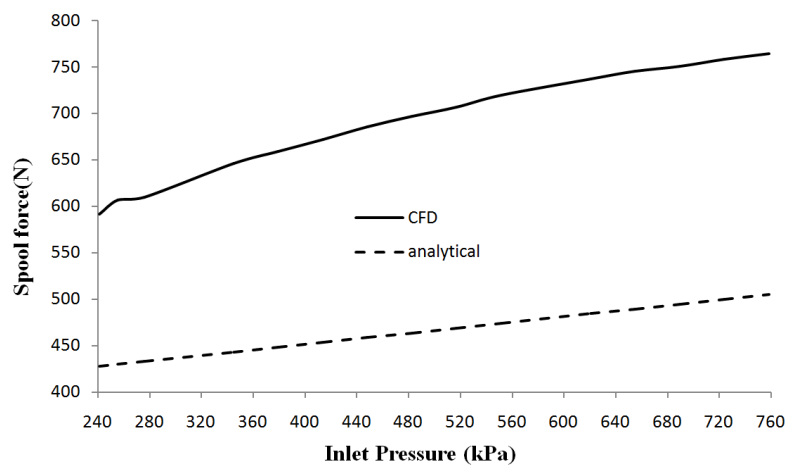


Fig. 8. Variable flow forces on spool surfaces with inlet pressure variation.

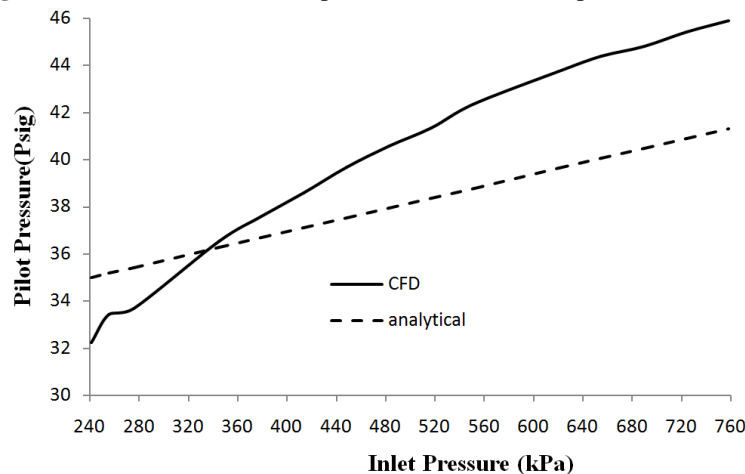


Fig. 9. Pressure characteristic of passive control circuit.

Fig. 10 shows the contour plots of static pressure at 100%, 60%, 30% and 10% spool opening. Corresponding inlet pressures are 241 kPa, 255 kPa, 276 kPa and 414 kPa respectively. A low pressure zone is created at immediate downstream of variable orifice. After that pressure recovery takes place. The size of low pressure zone increases with the increase in valve inlet pressure. This becomes clear from the stream function plots in Fig. 11. The plots clearly reveal the recirculation bubble and the associated downstream flow divergence in each case. Due to the increase in the size of the recirculation bubble with increase in the inlet pressure, the pressure recovery zone is pushed further right.

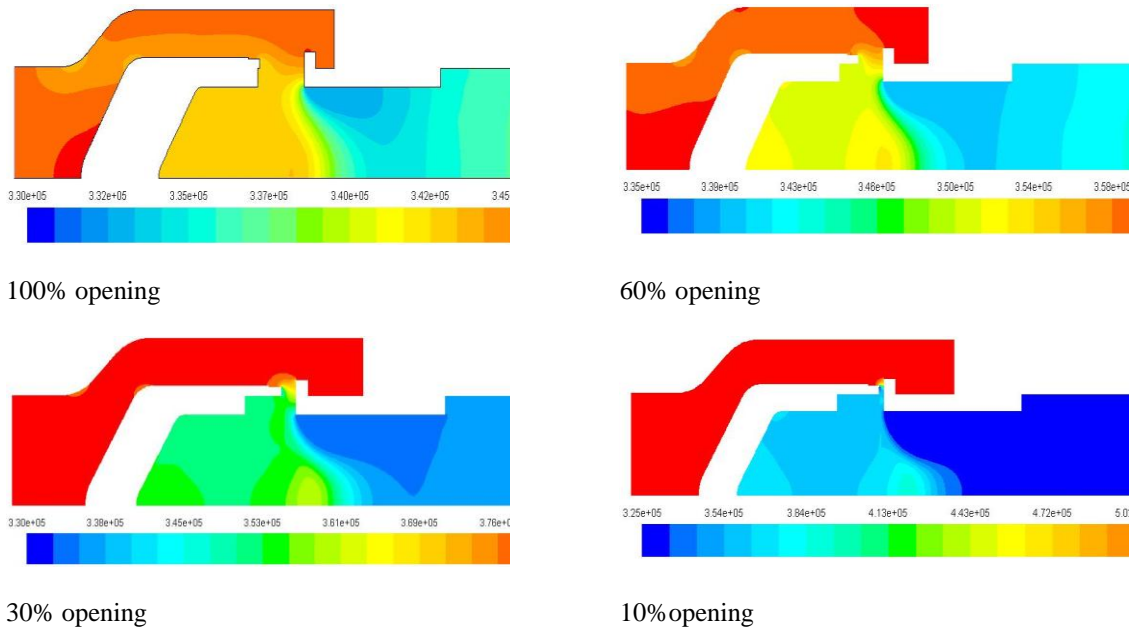


Fig. 10. Pressure contour in Pascal in the main flow path of the valve.

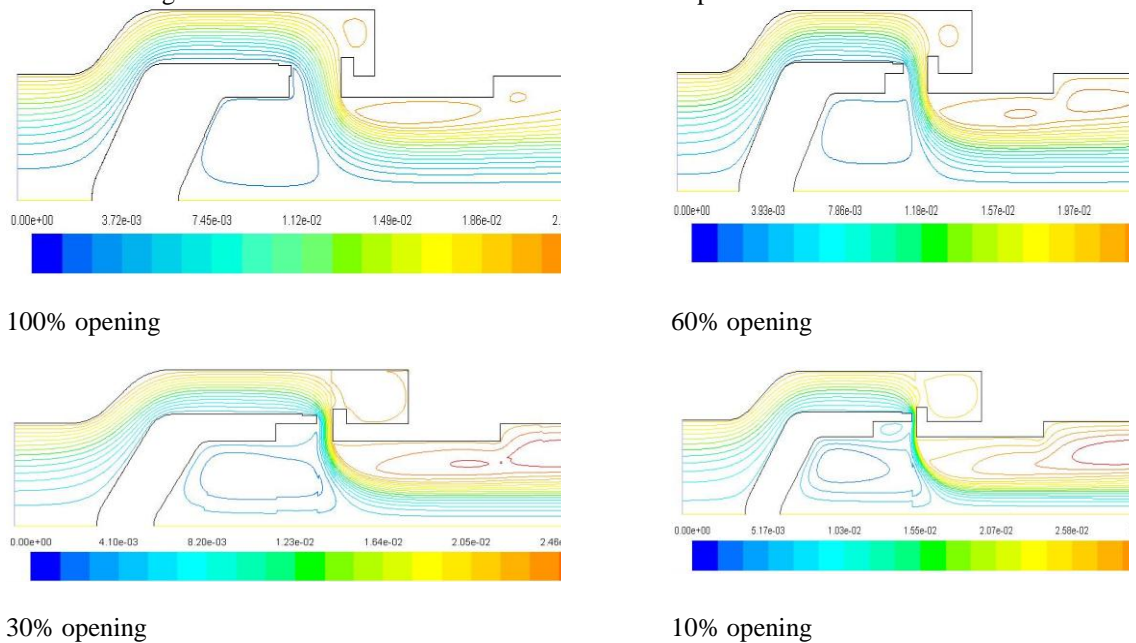
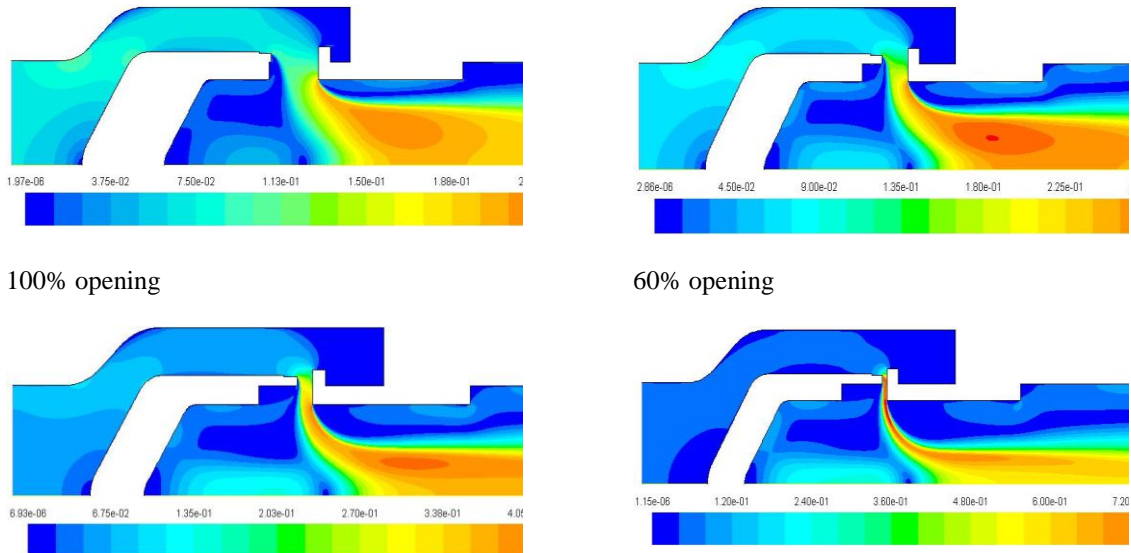
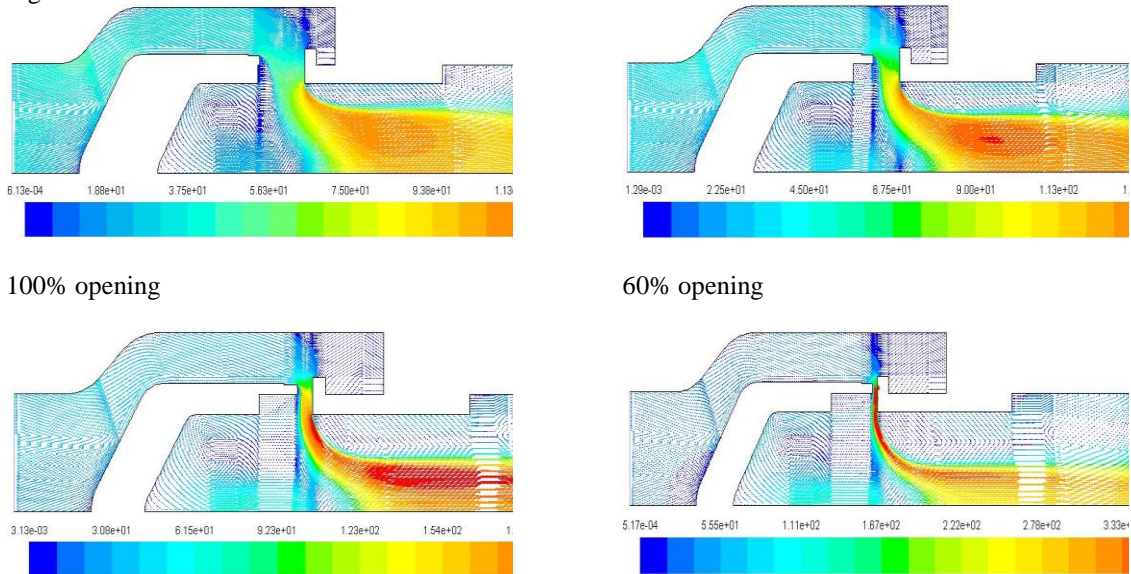


Fig. 11. Contour of stream function (kg/s) inside the main valve.

Figs. 12 and 13 depict the variation of the Mach number and the velocity vector through the valve body and the initial part of the spool valve. The low values of these two variables in the valve body can be attributed to the higher mean radius of the valve body in comparison to the bore diameter of the spool valve. As expected these values also remain low in the regions of the three recirculation bubbles discussed above with reference to Fig. 11. Between the two recirculation bubbles inside the spool valve, the flow enters the spool valve almost in an inward radial manner. Consistent with the decrease in the flow area due to the decrease in the mean radius, both the Mach number and the velocity keep on increasing. These increases signifying flow acceleration continue even during the flow turning to almost axial direction. Near to the axis, the acceleration persists due to the small inward radial component. Away from the axis up to the bubble, the flow decelerates due its diverging nature owing to the small outward radial component. The location of the peak velocity region away from the axis can be attributed to the sharper turning of the flow and the corresponding acceleration prior to reaching this region. Because of the complex flow structure inside the valve discussed above, CFD prediction of spool flow forces is more reliable.



100% opening
60% opening
30% opening
Fig. 12. Contour of Mach number inside the main valve.



100% opening
60% opening
30% opening
10% opening
Fig. 13. Velocity vector (m/s) inside the main valve.

V. CONCLUSION

Control circuit pressure characteristic has been calculated both analytically and by CFD method by solving compressible, turbulent flow through pressure regulated valve. In CFD analysis a special UDF has been developed to couple with ANSYS FLEUNT primarily to modify structured mesh of the flow domain dynamically with change in valve inlet pressure. CFD results has predicted better characteristic. Also, the simulation provides valuable insight into the control circuit behaviour, which is crucial for designers. Attempt to simulate using fully three-dimensional geometry is underway.

ACKNOWLEDGEMENT

We are thankful to Dr. Amitava Dasgupta for providing valuable advice on the functional aspect of the valve. Access to the high performance computing facility of CSIR-CMERI is gratefully acknowledged.

REFERENCES

- [1]. Z. Leutwyler and C. Dalton. A computational study of torque and force due to compressible flow on a butterfly valve disk in mid-stroke position. *J Fluid engineering*, 128:1074-84, 2006.
- [2]. R. Amirante, G. Del Vescove and A. Lippolis. Flow forces analysis of open center hydraulic directional control valve sliding spool. *Energy Conversion and Management*, 47:114-31, 2006.
- [3]. R. Amirante, G. Del Vescove and A. Lippolis. Evaluation of the flow forces on an open centre directional control valve by means of a computational fluid dynamic analysis. *Energy Conversion and Management*, 47:1748-60, 2006.
- [4]. R. Amirante, P.G. Moscatelli and L.A. Catalano. Evaluation of the flow forces on a direct (single stage) proportional valve by means of a computational fluid dynamic analysis. *Energy Conversion and Management*, 48:942-53, 2007.
- [5]. M.J. Chern, C.C. Wang and C.H. Ma. Performance test and flow visualization of a ball valve. *Experimental thermal and fluid sciences*, 31:505-12, 2007.
- [6]. H. Chattopadhyay, A. Kundu, B.K. Saha and T. Gangopadhyay. Analysis of Flow Structure inside a Spool Type Pressure Regulating Valve. *Energy Conversion and Management*, 53:196-204, 2012.
- [7]. X.G. Song, J.H. Jung, H.S. Lee, D.K. Kim and Y.C. Park. 2-D dynamic simulation of a pressure relief valve by CFD. Proc. 9th WSEAS Int. Conf. on Applied Computer and Applied Computational Science, Hangzhou, China. April 11-13, 2010.
- [8]. M. Borghi, M. Milani and R. Paoluzzi. Stationary axial flow force analysis on compensated spool valve. *Int J fluid power*, 1:17-25, 2000.
- [9]. J. Deng, X.M. Shao, X. Fu and Y. Zheng. Evaluation of the viscous heating induced jam fault of valve spool by fluid-structure coupled simulations. *Energy Conversion and Management*, 50:947-54, 2009.
- [10]. www.ansys.com
- [11]. P.L. Skousen. *Valve Handbook*. New York: McGraw-Hill, 2004.
- [12]. ASM International. *ASM Handbook, Volume 18. Friction, Lubrication and Wear Technology*, 1992.
- [13]. T.H. Shih, W.W. Liou, A. Shabbir, Z. Yang and J. Zhu. A new k- ϵ eddy-viscosity model for high Reynolds number turbulent flows—model development and validation. *Computers Fluids*, 24:227-38, 1995.

Hydraulic Transient: Lift Irrigation Scheme

Mohite Sudhir Ganpat¹, Morankar D.V.²

¹ Student M.Tech. Civil (Hydraulic Engineering), Bharati Vidyapeeth Deemed University, College of Engineering, Pune-411043

² Faculty of Civil Engineering, College of Military Engineering, Pune-411031

ABSTRACT:

Water hammer or hydraulic transient occur in pumping mains of Lift Irrigation Scheme (LIS) due to rapid changes in flow. These changes may be due to valve operations (sudden opening or closing of valves) or due to sudden failure of pumps following power failure. The resulting maximum and minimum water hammer pressures govern the design of a pumping main. The present study focuses on analysis of hydraulic transient phenomenon that may occur in pumping main of LIS. Sensitivity of water hammer pressure may be investigated with variation of various input parameters like pipe type, diameter, thickness and water temperature, pump inertia etc. Here sensitivity of maximum and minimum water hammer pressure is investigated with variation of key input parameters like pipe diameter and thickness.

In this study, Shirala Lift Irrigation Scheme was modeled for transient analysis by using SAP2 software. The scheme is characterised by total discharge of 1.18 m³/s, dynamic pump head of 58.86 m and 3.75 kilometers of mild steel pumping main. The sensitivity in hydraulic transient is investigated for variation of above mentioned key input parameters. It is observed that parameters to which water hammer is most sensitive are pipe diameter and thickness.

KEYWORDS: Hydraulic transient, Pumping main, Pressure wave, SAP2, Sensitivity, Shirala LIS, Transient analysis, Water hammer

I. INTRODUCTION

Pumping mains in lift irrigation scheme are required for safe, reliable and economic conveyance. Variation in fluid velocity causes pressure variations. Sudden failure of a pump or closing a valve cause propagation of transient pressure wave throughout the hydraulic system. This may cause significant pressure variations with reference to operating pressure, column separations, extensive cavitation, structural shakes and mass vibrations. Transient analysis is important aspect to be considered while designing pumping stations and pumping mains. Various codes and applications are developed to calculate or simulate water hammer, including but not limited to: Hammer, Surge, KYPipe, Hytran, PIPENET, Hypress, Flowmaster, LIQT, AFT Impulse, Transam, Relap5 and SAP2.

This study aims at hydraulic transient analysis of Shirala LIS for main governing conditions of upsurge & downsurge and also to investigate sensitivity of maximum & minimum transient pressures to change in parameters like pipe diameter and thickness. SAP2 software is used for transient analysis. Analyses are carried out with variations in input parameters.

The paper is divided into sub sections; section 2 presents recent literature on sensitivity analysis of water hammer problems in pipelines. Section 3 presents case study of Shirala LIS and input data. Section 4 deals with the methodology of the study. Section 5 presents analysis of results. The paper is concluded in section 6.

II. LITERATURE SURVEY

Kaliatka et al. (2009) studied water hammer model's sensitivity using a new approach called FAST (Fourier amplitude sensitivity test) and offered the results of their study. A water hammer induced by a fast valve closing was investigated using the RELAP5 / Mod3.3 code model.

Jalil Emadi and Abbas Solemani (2011) focused on determining significance of each input parameter of the application relative to the maximum water hammer estimated by the Hammer software. They found that moment of inertia of pump and electromotor, diameter, type and thickness of pipe and water temperature are the most effective parameters in reducing maximum water hammer.

Behnam Mansuri, Farzin Salmasi and Behrooz Oghati (2014) studied the sensitivity analysis for water hammer problem in pipelines by simulating the transient equations in MATLAB. They investigated sensitivity in negative and positive transient pressures by changing some variables such as pipe diameter, pipe length and wave velocity in pipe.

Sensitivity in transient analysis is less attended area in hydraulic transients. Limited literature is available.

III. CASE STUDY

This study examines hydraulic transients for main governing conditions of upsurge & downsurge and the sensitivity of transient pressures in the context of Shirala Lift Irrigation Scheme. It is on the left bank of Sina River, on upstream of Mahisgaon K.T. Weir near village Shirala in Paranda tahsil of Osmanabad district of Maharashtra state. The source of water is Sina river feed through Bhima-Sina link canal from Ujani reservoir. The scheme consists of lifting of water from Sina river on in single stage, providing irrigation benefits to 2850 Ha. of draught prone command area using 0.63 T.M.C. (17.84 Mm³) of water. The scheme is being implemented by the Water Resources Department, Maharashtra State. Figure 1 shows the geographical location of the scheme. It has two delivery mains, single pumping main and two pumps. Diameter, type and thickness of pipeline as well as discharge rate follow a uniform pattern throughout the pipeline system. Figure 2 shows layout of the scheme.



Figure 1. Index map of Maharashtra showing location of Shirala LIS

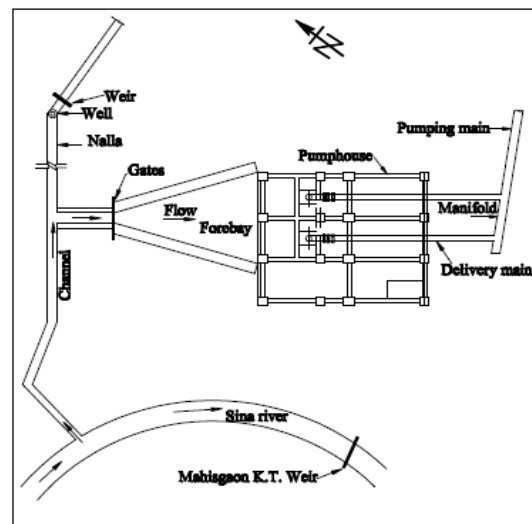


Figure 2. Typical layout of Shirala LIS

Input data

Physical and hydraulic characteristics of the pumping main used for transient and sensitivity analysis includes pumping main alignment data and pump data. The input data was obtained from Lift Irrigation Circle, Central Designs Organisation, Nashik. Figure 3 shows the longitudinal alignment of the pumping main. Figure 4 shows the schematic layout of the water transmission system of the project. It consists of two delivery mains and single pumping main. Delivery mains are 24 m long mild steel pipes of 600 mm internal diameter with 12 mm wall thickness. Centerline elevation of horizontal delivery mains is 482.50 m. Their chainage ranges from 0 to 24 m. Pumping main is 3750 m long mild steel pipe of 850 mm internal diameter with 6 mm wall thickness. Centerline elevation of pumping main at start is 482.50 m and at end at delivery chamber is 515.155 m. Its chainage ranges from 24 to 3774 m.

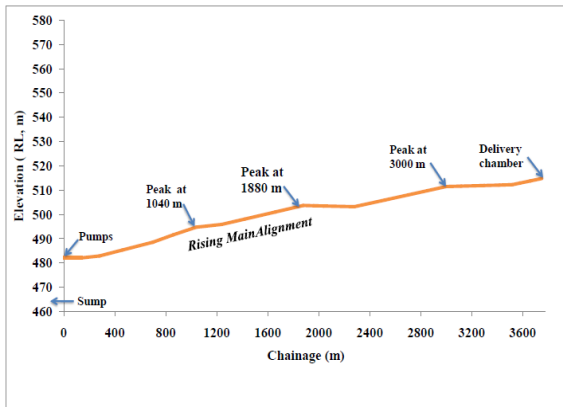


Figure 3. Longitudinal alignment of pumping main

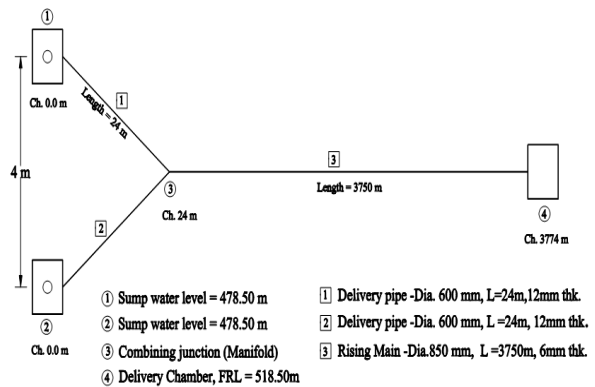


Figure 4. Schematic layout of Shirala LIS

Table 1 shows input data required for transient analysis.

Table 1. Input data for transient analysis

1	Design discharge	1.18 m ³ /s
2	Sump bottom level	466.00 m
3	MDDL in pump sump	471.00 m
4	FRL in sump	475.50 m
5	POL in sump	478.50 m
6	Centerline level of delivery pipe	482.50 m
7	FSL in delivery chamber	518.50 m
8	Pumping main Material Diameter Pipe wall thickness Number Length Discharge	Mild steel (MS) 850 mm 6 mm 1 No 3750 m Discharge 1.18 m ³ /s
9	Delivery main Material Diameter Pipe wall thickness Number Length Discharge	Mild steel (MS) 600 mm 12 mm 2 Nos 24 m Discharge 0.59 m ³ /s
10	Pump details Type H.P. Nos Rated discharge / pump Rated Head for pump Rated speed of pump Pump efficiency GD ² of pump GD ² of motor	Vertical turbine pumps 525 H.P. 2 Nos 0.59 m ³ /s 58.86 m 988 rpm 87.42 % 37 kg-m ² 68 kg-m ²

IV. METHODOLOGY

4.1 Transient Phenomenon

A phenomenon called water hammer / surge /hydraulic transients occurs in the pumping main of LIS when there are rapid changes in discharge. Change in flow rate due to rapid closure of control valves or tripping of pump following power failure causes to and fro transmission of transient pressure waves till steady state of flow is achieved. If the magnitude of resulting maximum and minimum pressure exceeds the limiting values and if the surge protection measures are not in place, a transient can cause pipe burst or pipe collapse. Therefore transient analysis is important during design stage for deciding protection measures and for ensuring proper functioning during operation stage.

4.2 Governing Equations

Transient / Unsteady flow through closed conduits can be described by the continuity and momentum equations given below. These equations are derived using equation of continuity of flow and Newton's second law [4].

Continuity Equation

$$\frac{\partial H}{\partial t} + V \frac{\partial H}{\partial x} + \frac{a^2}{g} \frac{\partial V}{\partial x} = 0 \quad (1)$$

Momentum equation

$$\frac{\partial V}{\partial t} + V \frac{\partial V}{\partial x} + g \frac{\partial H}{\partial x} + \frac{fV|V|}{2D} = 0 \quad (2)$$

In above equations, parameter D is inside diameter of pipe, a is pressure wave velocity, H is the piezometric head at the centerline of conduit above the specified datum, V is the average velocity of flow, f is friction coefficient, x is location dimension, t is time dimension and gravitational acceleration constant. The equations (1) and (2) describing the transient state flow in closed conduits are hyperbolic, partial differential equations. Most widely used Method of Characteristics is used to solve these equations. Transient analysis essentially consists of solving these equations, for every solution point and time step, for a wide variety of boundary conditions and system configurations.

4.3 Analysis Conditions

Various conditions considered in transient analysis are as below:

Steady state analysis: For steady flow there is no water hammer. Therefore, profiles for steady HGL, minimum & maximum pressure head must coincide. This option of analysis with all pumps running is a useful to check the validity of data and to detect possible errors.

Transient analysis: Power failure and single pump failure are the most critical surge condition for a pumping main in LIS. Failure of all the pumps due to power failure is critical with regard to surge pressures in the pumping main. Single pump failure, when multiple pumps are in parallel operation is critical with regard to surge pressures in the pump house. All transient analysis for a pumping main are carried out for critical surge condition of tripping of all pumps following power failure. Following conditions are considered.

i. Analysis without surge protection & without column separation: May or may not show extensive occurrence of negative pressures all along the alignment of pumping main.

ii. Analysis with column separation: If the above analysis shows extensive occurrence of negative pressures, transient analysis is carried out with column separation to find severity of upsurge due to rejoining of separated water columns.

iii. Analysis with / without column separation for upsurge protection: Is carried to find out effect upsurge protection devices on maximum pressure. These devices primarily control the upsurge.

iv. Analysis for downsurge protection: Is carried to find out effect of downsurge protection devices on minimum pressure. These devices primarily control the downsurge.

Limiting values of downsurge and upsurge

Permissible value of negative pressure is one third of atmospheric pressure i.e. -3.33 m plus allowance for overburden, if any, on lower side and value up to vacuum pressure i.e. -10.3 m on higher side. Generally, in conventional design, sub atmospheric pressures are not allowed.

Maximum pressure may be restricted to 1.25 to 1.5 times the pump head or working pressure [7].

V. RESULTS AND DISCUSSIONS

5.1 Results of Transient analysis in the context with Shirala LIS:

Hydraulic transient analysis is carried out for main governing conditions of upsurge & downsurge. These are described below.

i. Governing condition for downsurge or negative pressure: Analysis without surge protection & without column separation gives maximum values of downsurge. Results of analysis are tabulated as below in Table 2.

Table 2. Results of transient analysis for no protection condition

Pipe No	Node Ch. (m)	Max. Pr. (m)	Min. Pr. (m)
1	0	128.125	-54.695
2	0	128.125	-54.695
3	24	128.025	-54.665
3	280	120.53	-48.93
3	460	105.11	-38.55
3	860	81.04	-29.96
3	1240	77.15	-34.89
3	1660	72.385	-40.775
3	2040	70.19	-43.75
3	2520	67.9	-46.45
3	3000	62.03	-51
3	3420	61.19	-48.88
3	3750	37.6	-28.06

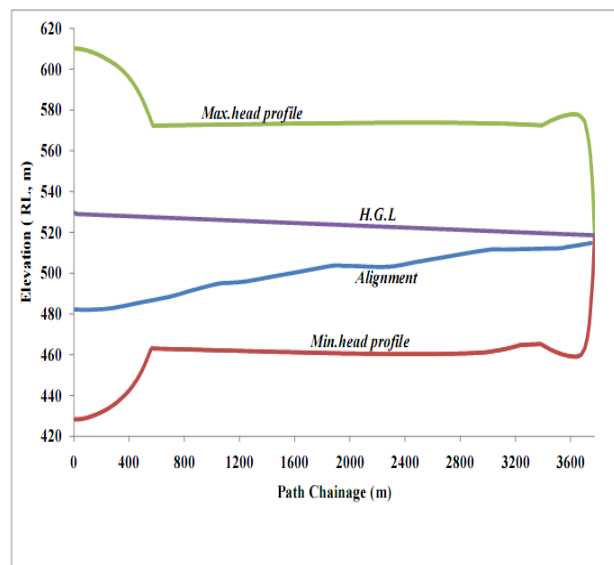


Figure 5. Minimum and maximum pressure for power failure with no protection

Figure 5 shows results of analysis with extensive occurrence of vacuum pressure all along the alignment of pumping main for no surge protection condition. Maximum value of minimum pressure is -55 m which is in excess of acceptable limit of -10m. Maximum value of upsurge is greater than two times the working head (58.86 m). Therefore values of both upsurge and down surge are exceeding limiting values.

ii. Governing condition for upsurge or positive pressure: Analysis without surge protection & with column separation gives maximum values of upsurge. Minimum pressure values in this analysis have no significance, hence skipped. Results of analysis are tabulated as below in Table 3.

Table 3. Results of transient analysis for column separation

Pipe No	Node Ch. (m)	Max. Pr. (m)
1	0	233.905
2	0	233.905
3	24	217.985
3	280	178.64
3	460	174.73
3	860	176.68
3	1240	163.43
3	1660	160.585
3	2040	151.18
3	2520	152.81
3	3000	152.4
3	3420	121.07
3	3750	116.31

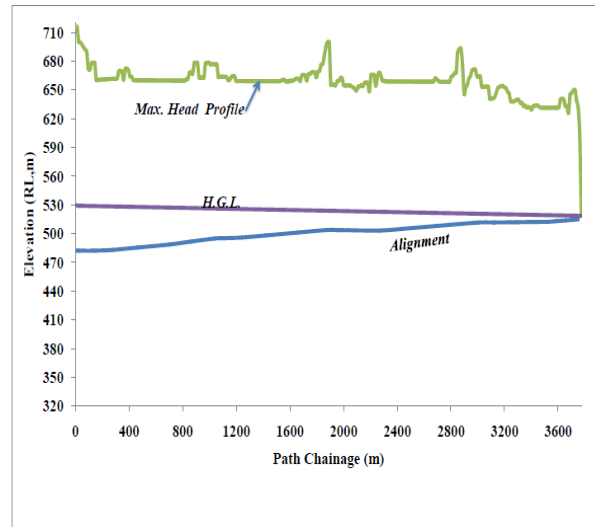


Figure 6. Minimum and maximum pressure for power failure with column separation

Figure 6 shows results of analysis without surge protection and with column separation. The maximum pressure for pumping main is 217.985 m. The hoop stress ($f = pD/2t$) at this pressure is 1544 kg/cm², which is moderately large compared to allowable value of 1200 kg/cm² as per IS 5822 -1994. As the maximum pressure is about four times the working pressure (58.86 m), pressure needs to be controlled with upsurge protection devices. For deciding intermediate locations and sizing of these devices, transient analysis with upsurge protection is carried out.

5.2 Sensitivity in transient analysis

Various input parameters like wave speed, friction factor, surge tank throttling coefficient, Machine inertia, water temperature, pipe type, thickness and diameter, electromotor rpm and power may have significant effects on the results of transient analysis. A thorough transient analysis will investigate the effect of different values for parameters. It is shown that maximum water hammer is most sensitive to pipe diameter and negative pressure is most sensitive to pipe thickness. Sensitivity study helps designers in well understanding of water hammer phenomenon.

The sensitivity in negative and positive pressures is investigated by changing key parameters such as pipe diameter and wall thickness.

i. Effect of pipe diameter

Pipe diameter is one of the parameter affecting velocity and pressure caused by water hammer event. Pipe diameter affects flow velocity. It also affects direct velocity during down surge and reflection pressure wave velocity during upsurge. Pressure wave velocity reduces with increase in diameter causing considerable reduction in maximum water hammer pressure. But downsurge capacity of pipe decreases with increase in diameter.

ii. Effect of Pipe Thickness

Water hammer pressure wave velocity increases with pipe thickness causing considerable improvement in downsurge capacity of pipe. But maximum water hammer pressure increases slightly with increase in pipe thickness.

5.2.1 Sensitivity of maximum water pressures to increase in pipe diameter

Determination of maximum water hammer pressure in pumping main is the most important from technical and economical point of view. To investigate effect of variation of pipe diameter on maximum water hammer, pipe diameter is varied from 850 mm to 1250 mm in the increment of 100 mm, within permissible velocity range (1.0- 2.1 m/s).

Table 4. Sensitivity of maximum water hammer to variation in pipe diameter

Pipe Dia. 'D' (mm)	Pr. Wave vel. 'a' (m/s)	Pr. Rise $\Delta H=av/g$ (m)	Max +WHP (m)	Change in +WHP (m)
850	923.67	195.84	231.46	
950	893.26	151.15	186.77	44.69
1050	865.67	120.01	155.63	31.14
1150	840.49	97.67	133.29	22.34
1250	817.38	79.99	115.61	17.68

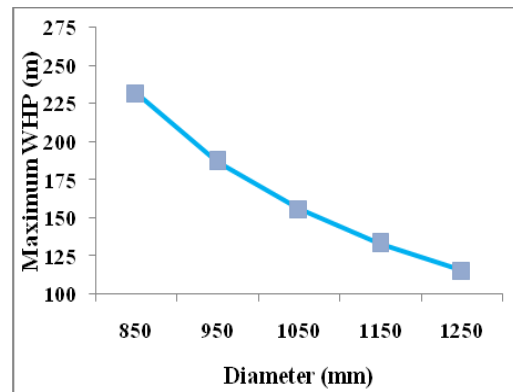


Figure 7. Variation of maximum water hammer with pipe diameter

With all other parameters remaining constant, results are shown in table 4 and figure7. It is observed that the maximum water hammer decreases linearly with increasing diameter. In the context of the Shirala project, 100 mm increase in diameter causes an average decrease of about 29 meters of water column in maximum water hammer for the diameter range considered. Therefore, maximum water hammer can be reduced by increasing pipe diameter (within permissible velocity range). This may increase initial costs of the project (by about 10% per kilometer length of pumping main) but it may eliminate the need for water hammer protection devices and future maintenance risks and costs.

5.2.2 Sensitivity of down surge to variation in pipe thickness

To investigate the effect of pipe thickness on down surge capacity of pipe, thickness range of 6 to 10 mm is considered.

Sensitivity of downsurge to variation in pipe thickness

Dia. (mm)	Pipe Thk. (mm)	Down surge capacity of pipes (m)	Down surge capacity /1 mm thk.	% Change
850	6	17.4		
	7	27	9.6	55%
	8	39.7	12.7	47%
	9	56	16.3	41%
	10	76.4	20.4	36%
		Ave	14.75	45%

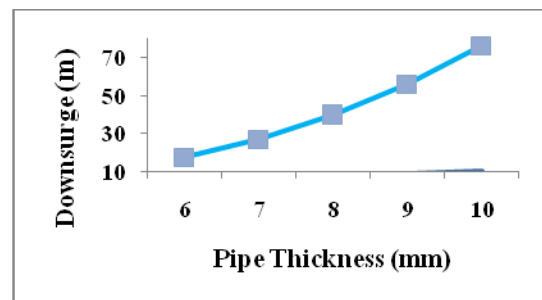


Figure 8. Effect of pipe thickness on downsurge capacity of pipe

With all other parameters remaining constant, results are shown in table 5 and figure 8. It is observed that the down surge improves by about 15 m in average for 1 mm increase in pipe thickness. On an average down surge improves by about 45% for 1 mm increases in pipe thickness with increase 13% in pipe cost per kilometer length.

VI. CONCLUSION

According to present study which was aimed at investigating the effect of key parameters; such as pipe diameter, thickness on hydraulic transient in the context of Shirala Lift Irrigation Scheme, shows that:

- With each 100 mm increase in pipe diameter, maximum water hammer pressure is reduced by 29 meters of water column.
- With each 1 mm increase in pipe thickness, minimum water hammer pressure / down surge carrying capacity is increased by 15 meters of water column

REFERENCES

- [1] Algirdas Kaliatka, Vytis Kopustiniskas and Mindaugas Vaisnoras (2009) Water hammer model sensitivity study by FAST method. *Energetika*, 2009, T. 55. Nr.1, 13–19.
- [2] Behnam Mansuri, Farzin Salmasi and Behrooz Oghati (2014) Sensitivity Analysis for Water Hammer Problem in Pipelines, *Iranica Journal of Energy & Environment* 5 (2): 124-131.
- [3] Bryan W Karney and Duncann McInnis (1990), Transient analysis of water distribution systems, *Journal AWWA*, 62-70.
- [4] Chaudhary, M. H. (1979), *Applied Hydraulic Transients*, New York: Van Nostrand Reinhold Company Limited.
- [5] Don J.Wood (2005), Water-hammer analysis-essential and easy (and efficient), *Journal of Environmental Engineering*, Vol.131, No.8, 1123-1131.
- [6] Jalil Emadi, Abbas Solemani (2011) Maximum Water Hammer Sensitivity, *World Academy of Science, Engineering and Technology*, 49,416-19.
- [7] SAP 2R (2009), *Surge Analysis Program Version 2R*, Transient analysis software from Department of Civil Engineering, Indian Institute of Science, Bangalore.